

2000

An investigation of temperature control issues related to intelligent thermoforming

Khoo Guan Soon
Lehigh University

Follow this and additional works at: <http://preserve.lehigh.edu/etd>

Recommended Citation

Soon, Khoo Guan, "An investigation of temperature control issues related to intelligent thermoforming" (2000). *Theses and Dissertations*. Paper 667.

This Thesis is brought to you for free and open access by Lehigh Preserve. It has been accepted for inclusion in Theses and Dissertations by an authorized administrator of Lehigh Preserve. For more information, please contact preserve@lehigh.edu.

Soon, Khoo Guan
An Investigation of
Temperature
Control Issues
Related to
Intelligent
Thermoforming

January 2001

**AN INVESTIGATION OF TEMPERATURE CONTROL ISSUES
RELATED TO INTELLIGENT THERMOFORMING**

by

Khoo Guan Soon

A Thesis

Presented to the Graduate and Research Committee

of Lehigh University

in Candidacy for the Degree of

Master of Science

In

Mechanical Engineering

Lehigh University

September 2000

This thesis is accepted and approved in complete fulfillment of the requirements
for the degree of Master of Science in Mechanical Engineering.

September 11, 2000

Date

John P. Coulter, Thesis Advisor

Charles R. Smith, Chairperson of the Department

ACKNOWLEDGMENTS

First, I would like to thank the sponsors of this research project. Funding for this project was provided by the Department of Mechanical Engineering & Mechanics of Lehigh University, Pennsylvania. I am also thankful for the joint effort of Dr. Herman F. Nied and the Mechanical Engineering & Mechanics Department in providing the ZMD V-200 Series Thermoforming machine, which this research study was based upon.

Special thanks to Dr. John P. Coulter for his valuable advise, focused disposition, and affable attitude during my graduate research work in the Intelligent Materials and Manufacturing Laboratory.

I would also like to thank my friends and mentors from Susquehanna University, namely Dr. Fred Grosse, Dr. David Bussard, Dr. Kate Hastings, and Jim Sodt for illuminating the path of my potential.

I am indebted to my mother and father for the sacrifices they made for their children to study abroad. Their lessons on responsibility, thoroughness, and modesty have been a constant impetus for my research work.

I am also grateful to Al, Bobby, Kate & Spencer, Bogie & Lauren, Nick & Nora, "The Duke", Aimee Mann, Stan Kubrick, and David Lynch for the privilege of looking through their eyes.

Finally, I am glad to have met Jenni Messimer who has brought me solace and youthfulness.

TABLE OF CONTENTS

ABSTRACT	1
CHAPTER 1: INTRODUCTION TO THERMOFORMING TECHNOLOGY	3
1.1 Introduction to Technology	3
1.2 Related Challenges and Opportunities.....	7
1.3 Motivation behind the Current Research Investigations.....	11
1.4 Scope of Current Research	15
CHAPTER 2: REVIEW OF THERMOFORMING LITERATURE.....	17
2.1 Material Distribution Control in Thermoforming.....	18
2.2 Radiant Heat Transfer Modeling	22
2.3 Sheet Surface Temperature Control through Zone-Heaters.....	25
2.4 Temperature Sensing Capabilities	26
2.5 Sensing & Control Systems in Thermoforming	28
CHAPTER 3: NUMERICAL INVESTIGATION OF POLYMER SHEET TEMPERATURE CONTROL THROUGH ZONE HEATER IMPLEMENTATION.....	29
3.1 Theoretical Development	29
3.1.1 Radiation Exchange between Black Bodies	29
3.1.2 Introduction to the View Factor.....	37
3.1.3 Radiation Exchange between Gray Bodies.....	39
3.2 Heat Transfer Governing Equations Applicable for Radiant Heating during Thermoforming.....	48
3.3 Numerical Solution Approach	50
3.3.1 Discretization of the Governing Equation	50
3.3.2 Software Package Utilized.....	52
CHAPTER 4: EXPERIMENTAL TEMPERATURE SENSING APPROACH	55
4.1 Introduction to IR Imaging Technology	55
4.2 Thermal Imaging System and Temperature Calibration.....	57
4.3 IR Experimental Set-up	60
4.4 Radiant Heater Settings	64
CHAPTER 5: THEORETICAL AND EXPERIMENTAL RESULTS	67
5.1 Individually Controlled Radiant Zone-Heating Patterns	67
5.2 Qualitative Comparisons between Numerical and Experimental Results.....	70
CHAPTER 6: DISCUSSION, CONCLUSIONS AND RECOMMENDATIONS	96
6.1 Feasibility of Sensor-Controller Scheme.....	97
6.2 Numerical Program Usage.....	99
6.3 Possibilities for Temperature Patterns	101
6.4 Recommendations for Future Investigations	102
6.4.1 Further Improvements in IR Thermal Imaging System.....	103
6.4.2 Revision of Radiant Heat Transfer Exchange Simulation	105
6.4.3 Proposals for More Effective Zone-heating Thermoforming	105
REFERENCES	107
VITA	111

LIST OF FIGURES

Figure 1. 1 : An example of large-part thermoformed parts for automotive applications, from the Innovation Center at GE Plastics Automotive in Southfield, Mich.	3
Figure 1. 2 : The vacuum-forming process of a heated polymer sheet into a female mold.	4
Figure 1. 3 : A Variety of Widemouth PET Food Containers that are Challenging the Existing Glass Jars...5	5
Figure 1. 4 : A thermoformed bus bumper from Metrotrans Corp, that's stronger, lighter and more cost effective than the previous fiberglass bumper system	6
Figure 1. 5 : The plug-assisted thermoforming from A through D. The plug device acts like a male mold as the polymer sheet is vacuum-formed into a female mold.	8
Figure 1. 6 : The Conventional Trial & Error-Oriented Thermoforming in Industry. This technique, which starts from the bottom left image, requires excessive reiterations.	9
Figure 1. 7 : Zone-Heaters Incorporated in a Thermoforming Machine.....	10
Figure 1. 8 : A Diagram of the Proposed Sensing & Controls System for Zone-Heating Thermoforming. The loop starts from the bottom left and finishes on the bottom right, without excessive reiterations nor product quality inspections.....	13
Figure 1. 9 : A Summary of the Organization of the Thesis.....	16
Figure 2. 1 : The Areas of Active Thermoforming Research.	17
Figure 2. 2 : Some Contributing Authors for Material Thickness Control.....	18
Figure 2. 3 : Some Contributing Authors for Radiant Heat Transfer Modeling.....	22
Figure 2. 4 : Some Contributing Authors for Sheet Surface Temperature Control	25
Figure 2. 5 : Some Contributing Authors for Temperature Sensing Capabilities.....	26
Figure 2. 6 : Some Contributing Authors for Sensing & Controls System.....	28
Figure 3. 1: Zone Heating Differential Elements in 3-Dimensional Cartesian Coordinates.....	30
Figure 3. 2: Projected Area of Differential Heater Element, dA_h ,	31
Figure 3. 3: Radiation Emitted by dA that passes through a small area dA_n	32
Figure 3. 4: Definition of the Solid Angle.....	33
Figure 3. 5: Diagram of the Projected Sheet Area View from the Heater Element	34
Figure 3. 6 : 2-D Representation of Heater and Sheet Element Geometry.....	39
Figure 3. 7: Relationship between radiative flux, radiosity, and irradiation.....	41
Figure 3. 8: Electrical Analog of Heat Transfer from a Surface i	42

Figure 3. 9: Electrical Analog between Heater and Sheet Elements (Gray bodies).....	43
Figure 3. 10: Discretization of One-Dimensional Heat Conduction through Finite Difference Approximation.....	50
Figure 4. 1: As shown in the diagram above, infrared energy from objects in the scene (A) is focused by optics (B) onto an infrared detector (C). The information from the infrared detector is passed to sensor electronics (D) for image processing. The signal processing circuitry translates the infrared detector data into an image that can be viewed on a standard video monitor (E).	56
Figure 4. 2: Example of visible light versus infrared imaging. The left image is what you may see in ordinary light on a dark night. The image at right is the same scene but as seen with an Infrared camera	57
Figure 4. 3: Linear relationship between incoming thermal energy and gray scale value.	57
Figure 4. 4: The influence of emissivity(ϵ), reflectivity(ρ) and transmissivity(τ) on the detected energy... ..	59
Figure 4. 5: During heating (a), the top and bottom zone heaters are positioned a distance $Z = 8''$ or $Z = 12''$ ($\pm 1''$) from the polymer sheet. With a 25mm lens, the IR imager is placed 61.5'' above the target polymer sheet, in the forming area (b) to obtain a view that encompasses the sheet and reference black bodies.	61
Figure 4. 6: An IR image of the forming area, including the clamps and two black body reference "points" for temperature calibration.	62
Figure 4. 7: Individually Controlled Heaters for Top (a) and Bottom (b), numbered from 1 to 24.....	65
Figure 4. 8: The heat patterns, (i) to (viii), chosen for the present investigation.	66
Figure 5. 1: Individually Controlled Heaters for Top (a) and Bottom (b), Numbered from 1 to 24.....	68
Figure 5. 2: The heat patterns, (i) to (viii), chosen for the experimental investigation.....	69
Figure 5. 3: Plot of Temperature ($^{\circ}\text{F}$) versus Heater Setting (%) for Heater "24".	70
Figure 5. 4: Comparison of Theoretical and Experimental Temperature Distribution Corresponding to Heater Pattern 1 at $Z = 12$ inches: (a) Experimental IR Image at $t=60\text{s}$; (b) Numerical Image at $t=60\text{s}$; (c) Experimental IR Image at $t=120\text{s}$; (d) Numerical Image at $t=120\text{s}$	72
Figure 5. 5: Comparison of Theoretical and Experimental Temperature Distribution Corresponding to Heater Pattern 1 at $Z = 8$ inches: (a) Experimental IR Image at $t=60\text{s}$; (b) Numerical Image at $t=60\text{s}$; (c) Experimental IR Image at $t=120\text{s}$; (d) Numerical Image at $t=120\text{s}$	73
Figure 5. 6: Comparison of Theoretical and Experimental Temperature Distribution Corresponding to Heater Pattern 2 at $Z = 12$ inches: (a) Experimental IR Image at $t=60\text{s}$; (b) Numerical Image at $t=60\text{s}$; (c) Experimental IR Image at $t=120\text{s}$; (d) Numerical Image at $t=120\text{s}$	75
Figure 5. 7: Comparison of Theoretical and Experimental Temperature Distribution Corresponding to Heater Pattern 2 at $Z = 8$ inches: (a) Experimental IR Image at $t=60\text{s}$; (b) Numerical Image at $t=60\text{s}$; (c) Experimental IR Image at $t=120\text{s}$; (d) Numerical Image at $t=120\text{s}$	76

Figure 5. 8: Comparison of Theoretical and Experimental Temperature Distribution Corresponding to Heater Pattern 3 at Z = 12 inches: (a) Experimental IR Image at t=60s ; (b) Numerical Image at t=60s ; (c) Experimental IR Image at t=120s ; (d) Numerical Image at t=120s.	78
Figure 5. 9: Comparison of Theoretical and Experimental Temperature Distribution Corresponding to Heater Pattern 3 at Z = 8 inches: (a) Experimental IR Image at t=60s ; (b) Numerical Image at t=60s ; (c) Experimental IR Image at t=120s ; (d) Numerical Image at t=120s.	79
Figure 5. 10: Comparison of Theoretical and Experimental Temperature Distribution Corresponding to Heater Pattern 4 at Z = 12 inches: (a) Experimental IR Image at t=60s ; (b) Numerical Image at t=60s ; (c) Experimental IR Image at t=120s ; (d) Numerical Image at t=120s.	81
Figure 5. 11: Comparison of Theoretical and Experimental Temperature Distribution Corresponding to Heater Pattern 4 at Z = 8 inches: (a) Experimental IR Image at t=60s ; (b) Numerical Image at t=60s ; (c) Experimental IR Image at t=120s ; (d) Numerical Image at t=120s.	82
Figure 5. 12: Comparison of Theoretical and Experimental Temperature Distribution Corresponding to Heater Pattern 5 at Z = 12 inches: (a) Experimental IR Image at t=60s ; (b) Numerical Image at t=60s ; (c) Experimental IR Image at t=120s ; (d) Numerical Image at t=120s.	84
Figure 5. 13: Comparison of Theoretical and Experimental Temperature Distribution Corresponding to Heater Pattern 5 at Z = 8 inches: (a) Experimental IR Image at t=60s ; (b) Numerical Image at t=60s ; (c) Experimental IR Image at t=120s ; (d) Numerical Image at t=120s.	85
Figure 5. 14: Comparison of Theoretical and Experimental Temperature Distribution Corresponding to Heater Pattern 6 at Z = 12 inches: (a) Experimental IR Image at t=60s ; (b) Numerical Image at t=60s ; (c) Experimental IR Image at t=120s ; (d) Numerical Image at t=120s.	87
Figure 5. 15: Comparison of Theoretical and Experimental Temperature Distribution Corresponding to Heater Pattern 6 at Z = 8 inches: (a) Experimental IR Image at t=60s ; (b) Numerical Image at t=60s ; (c) Experimental IR Image at t=120s ; (d) Numerical Image at t=120s.	88
Figure 5. 16: Comparison of Theoretical and Experimental Temperature Distribution Corresponding to Heater Pattern 7 at Z = 12 inches: (a) Experimental IR Image at t=60s ; (b) Numerical Image at t=60s ; (c) Experimental IR Image at t=120s ; (d) Numerical Image at t=120s.	90
Figure 5. 17: Comparison of Theoretical and Experimental Temperature Distribution Corresponding to Heater Pattern 7 at Z = 8 inches: (a) Experimental IR Image at t=60s ; (b) Numerical Image at t=60s ; (c) Experimental IR Image at t=120s ; (d) Numerical Image at t=120s.	91
Figure 5. 18: Comparison of Theoretical and Experimental Temperature Distribution Corresponding to Heater Pattern 8 at Z = 12 inches: (a) Experimental IR Image at t=60s ; (b) Numerical Image at t=60s ; (c) Experimental IR Image at t=120s ; (d) Numerical Image at t=120s.	93
Figure 5. 19: Comparison of Theoretical and Experimental Temperature Distribution Corresponding to Heater Pattern 8 at Z = 8 inches: (a) Experimental IR Image at t=60s ; (b) Numerical Image at t=60s ; (c) Experimental IR Image at t=120s ; (d) Numerical Image at t=120s.	94
Figure 6. 1: A proposed thermal imaging procedure for real-time IR detection in the heating stage.....	99
Figure 6. 2: A Model System for Improved Sheet Temperature Control by Combining Zone-heating with Moveable Heat Shields.....	103

ABSTRACT

The current investigation focused on the advancement of thermoforming processes with the future goal of fully intelligent manufacturing in mind. Thermoforming has been a traditionally under-utilized manufacturing process, and appropriate science-based advancements could render the process applicable to a much wider range of products. During the study, temperature control issues related to zone-heater based thermoforming were addressed. The specific goals of the work included: 1) the development of an experimental capability to monitor polymer sheet temperature distributions during thermoforming, and 2) the experimental and numerical analysis of the range of temperature distributions that can be obtained with typical zone heater based thermoforming equipment.

During the study, a numerical analysis of polymer sheet heating during thermoforming was completed. The theoretical basis for the phenomenon was developed, and it was then concluded that an existing software package was suitable for utilization during the present effort. In addition, a coupled experimental effort was completed during which an infrared(IR) energy based two-dimensional temperature imaging system was developed and tested.

Once the developmental phases of the work were completed, numerically predicted and experimentally measured temperature

distributions were generated for 32 different processing condition combinations. The conditions studied covered the range of typical thermoforming equipment capabilities, and incorporated eight different zone heater setting configurations, two heating times, and two heater to sheet spacing distances.

The results from both the numerical and experimental portions of the study showed that zone heating can yield a wide range of temperature distributions (and corresponding stiffness distributions) in polymer sheets during thermoforming. Furthermore, when corresponding numerical and experimental temperature distributions were compared, reasonable qualitative agreement resulted in all cases. It was concluded, however, that improved quantitative agreement could be obtained if additional suggested advancements in this area were realized. The work that was accomplished as part of the current study has laid the necessary groundwork for such subsequent advancements.

CHAPTER 1

INTRODUCTION TO THERMOFORMING TECHNOLOGY

1.1 Introduction to Technology

Also known as pressure or vacuum-forming, thermoforming is a manufacturing process highly utilized by the plastics packaging industry. This is true despite economic and environmental obstacles in the early 90s. In addition to thermoformed packaging containers of lesser complexity and size, this somewhat under-utilized plastics forming process is currently being used for large and complex products as well. Figure 1.1 below displays the DaimlerChrysler MCC (Micro Compact Car) "Smart Car" from 1999 with its molded-in-color body panels with clearcoat.



Figure 1.1 : An example of large-part thermoformed parts for automotive applications, from the Innovation Center at GE Plastics Automotive in Southfield, Michigan (GE Plastics Photo Library Library-Automotive at http://www.geplastics.com/resins/news/press/photo_library/automotive/)

CHAPTER 1

INTRODUCTION TO THERMOFORMING TECHNOLOGY

1.1 Introduction to Technology

Also known as pressure or vacuum-forming, thermoforming is a manufacturing process highly utilized by the plastics packaging industry. This is true despite economic and environmental obstacles in the early 90s. In addition to thermoformed packaging containers of lesser complexity and size, this somewhat under-utilized plastics forming process is currently being used for large and complex products as well. Figure 1.1 below displays the DaimlerChrysler MCC (Micro Compact Car) "Smart Car" from 1999 with its molded-in-color body panels with clearcoat.



Figure 1.1 : An example of large-part thermoformed parts for automotive applications, from the Innovation Center at GE Plastics Automotive in Southfield, Michigan (GE Plastics Photo Library Library-Automotive at http://www.geplastics.com/resins/news/press/photo_library/automotive/)

The light weight yet sufficiently impact resistant plastic panels, from GE, weigh 50% less than their traditional equivalents[1]. The versatility and potential of this plastics sheet-forming technique, from thermoformed plastic containers and shower stalls to aircraft and medical applications, rival those of injection molding and other forming processes. In particular, the demand for high mechanical strength yet light weight body panels is moving the automotive industry towards capitalizing on thermoforming advantages[2-4]. Nevertheless, few science-based findings related to this method are documented in academic journals. Industrial practices, though copious in regard to the various methods of thermoforming, rely heavily on operator experiences and non-scientific trials.

Thermoforming is a plastics manufacturing process where a securely clamped polymer sheet material is formed by heat and pressure, as shown in Figure 1.2 below.

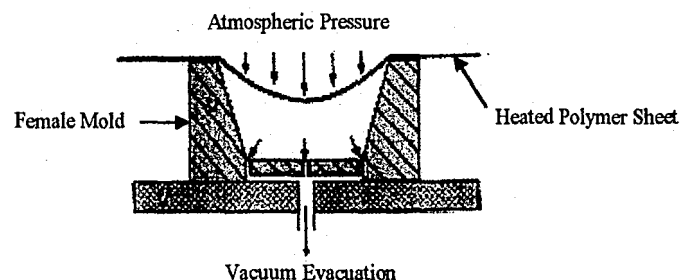


Figure 1. 2 : The vacuum-forming process of a heated polymer sheet into a female mold.

Infrared radiant heat is the common mode of heating the plastic sheet to above its glass transition temperature prior to deformation over a male or into a female mold. Generally, female

molds produce thinner side and bottom walls, whereas male molds create substantial stretching, which results in thinning, on the flange area near the clamps. A combination of both male and female molds produces the plug-assisted forming method, which is the most prevailing technique used throughout the thermoforming industry today. Plug-assisted thermoforming produces a more uniform material distribution in the final deformed product, thus combining the advantages of both the male and female mold based techniques.

The interest in thermoforming is directly linked to the overall level of enthusiasm towards plastics as a processing material. The domination of plastics over the use of glass or other materials can be illustrated by observing the shelves of grocery stores.



Figure 1. 3 : A Variety of Widemouth PET Food Containers that are Challenging the Existing Glass Jars (Modern Plastics DEC 1999, Pg. 50, from GrafcO).

molds produce thinner side and bottom walls, whereas male molds create substantial stretching, which results in thinning, on the flange area near the clamps. A combination of both male and female molds produces the plug-assisted forming method, which is the most prevailing technique used throughout the thermoforming industry today. Plug-assisted thermoforming produces a more uniform material distribution in the final deformed product, thus combining the advantages of both the male and female mold based techniques.

The interest in thermoforming is directly linked to the overall level of enthusiasm towards plastics as a processing material. The domination of plastics over the use of glass or other materials can be illustrated by observing the shelves of grocery stores.



Figure 1.3 : A Variety of Widemouth PET Food Containers that are Challenging the Existing Glass Jars (Modern Plastics DEC 1999, Pg. 50, from Grafco).

Glass jars of the wide-mouth variety, an enduring choice in food packaging, are confronting plastics competitors in the form of blow-molded PET (Polyethylene Terephthalate) containers, as illustrated in Figure 1.3 above. Thermoformed PS (Polystyrene) has an estimated 1.8 million tons share in the global packaging market[5]. Outside the food packaging industry, plastics have been steadily replacing sheet metal vehicle exteriors. Large-part thermoforming has enabled the option of plastic body panels, like bus bumpers as seen in Figure 1.4, and roofs of recreational vehicles. ABS (acrylonitrile-butadiene-styrene), a tough engineering thermoplastic with a large temperature window for thermoforming, and polycarbonates are the most common polymeric materials utilized for such automotive applications. Over 1.3 billion tons of ABS are used annually in the US[2].

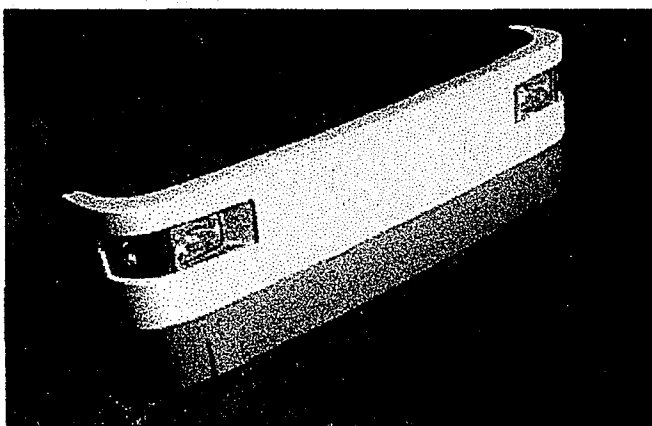


Figure 1.4 : A thermoformed bus bumper from Metrotrans Corp, that's stronger, lighter and more cost effective than the previous fiberglass bumper system. (GE Plastics Photo Library Library-Automotive at http://www.geplastics.com/resins/news/press/photo_library/automotive/)

Besides the related weight reducing and impact resistant attributes, thermoformed plastics permit lower investment

Glass jars of the wide-mouth variety, an enduring choice in food packaging, are confronting plastics competitors in the form of blow-molded PET (Polyethylene Terephthalate) containers, as illustrated in Figure 1.3 above. Thermoformed PS (Polystyrene) has an estimated 1.9 million tons share in the global packaging market[5]. Outside the food packaging industry, plastics have been steadily replacing sheet metal vehicle exteriors. Large-part thermoforming has enabled the option of plastic body panels, like bus bumpers as seen in Figure 1.4, and roofs of recreational vehicles. ABS (acrylonitrile-butadiene-styrene), a tough engineering thermoplastic with a large temperature window for thermoforming, and polycarbonates are the most common polymeric materials utilized for such automotive applications. Over 1.3 billion tons of ABS are used annually in the US[2].

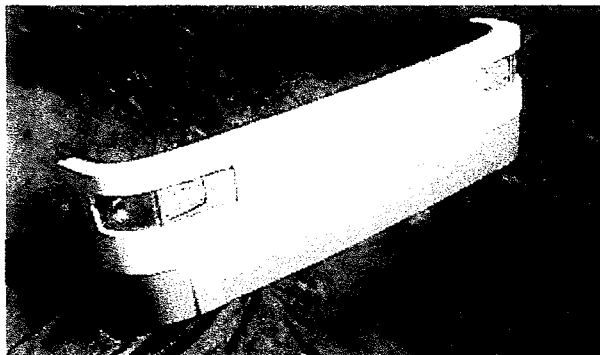


Figure 1. 4 : A thermoformed bus bumper from Metrotrans Corp, that's stronger, lighter and more cost effective than the previous fiberglass bumper system. (GE Plastics Photo Library Library-Automotive at http://www.geplastics.com/resins/news/press/photo_library/automotive/)

Besides the related weight reducing and impact resistant attributes, thermoformed plastics permit lower investment

expenses and allow for greater product variance due to shorter product life cycles. Therefore, the reduction of mold costs and lead times in thermoforming provide a provident alternative to injection molding, blow molding, or structural foam molding[6]. Traditional thermoforming molds are generally less complex in shape and significantly less expensive than those for injection molding. However, with 3-D solid modeling and sophisticated CNC machining, more detailed precision molds are now feasible[6]. Moreover, relatively new mold materials for thermoforming like Metapor and Espor (microporous aluminum alloy) rival the higher mold complexity and texture obtained through injection molding. Aside from these modest developments, the "low tech" thermoforming industry lacks the understanding of the science behind this seemingly uncomplicated heat-and-form process. Many opportunities are available for science-based studies in heat sensing and control, process modeling, and optimization of forming parameters.

1.2 Related Challenges and Opportunities

The archetypal thermoforming problem lies in the pursuit of material distribution control, be it a uniform or some prescribed thickness[7-9]. A common counterstrike against this blockade is persistent process parameter optimization. Plug-assisted thermoforming, as seen in Figure 1*5, is a popular industrial practice that is applied with the goal of improved material

distribution. Several journal papers have endeavored to empirically optimize this process parameter by varying plug speed, size, shape, and material. Other experimental studies of process parameters include the optimization of forming temperature (or heating time), vacuum drawing speed, and mold temperature.

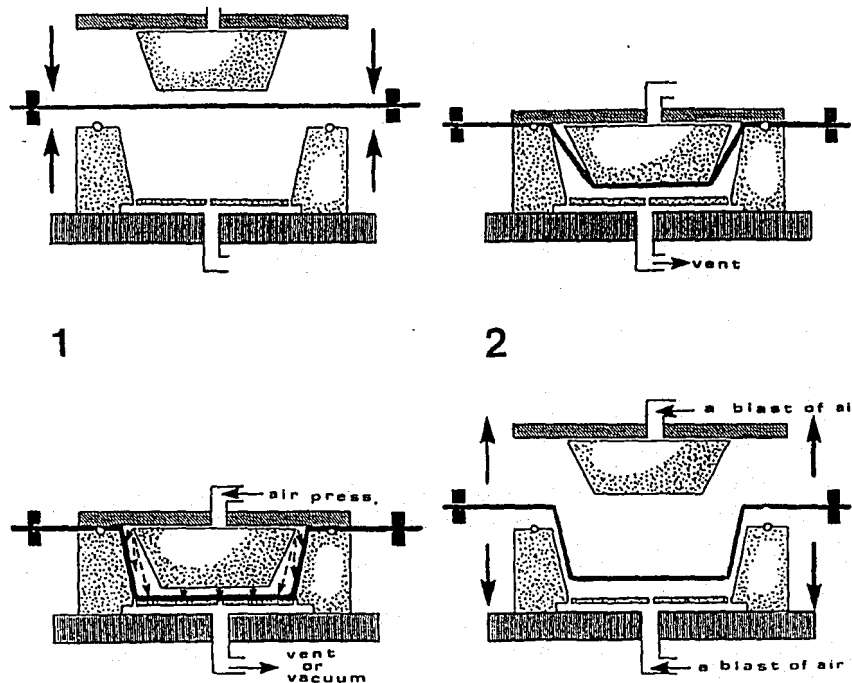


Figure 1. 5 : The plug-assisted thermoforming from A through D. The plug device acts like a male mold as the polymer sheet is vacuum-formed into a female mold.

An attempt to better control the sheet temperature prior to forming gave rise to zone-heating through individually controlled heaters. This promising technique, designed to obtain desired heating patterns, remains an insufficiently studied, trial-dependent routine that will benefit this thermoforming rut. Figure 1.6 provides a summary of the traditional "low tech"

thermoforming practice, while Figure 1.7 shows an example of zone heaters embedded in a thermoforming machine.

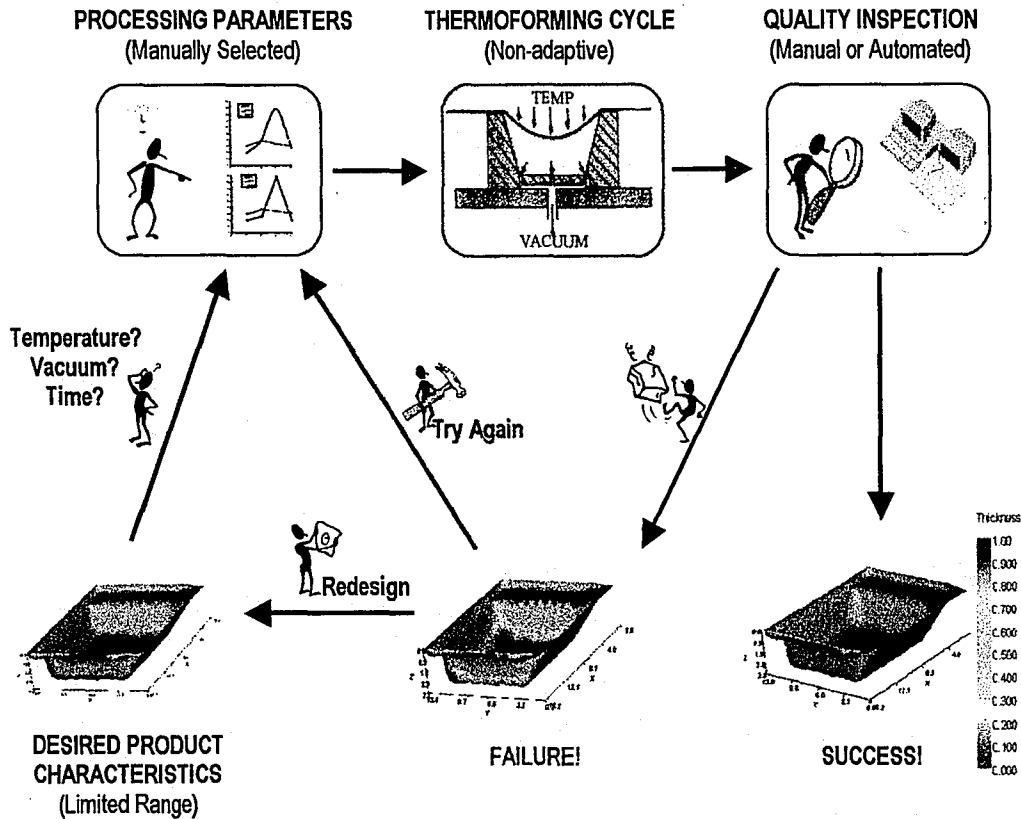


Figure 1.6 : The Conventional Trial & Error-Oriented Thermoforming in Industry. This technique, which starts from the bottom left image, requires excessive reiterations.

The prediction of the final sheet thickness is critically dependent on the accurate measurement of sheet temperature prior to deformation. Therefore, sheet temperature sensing is an integral part of this research thesis. Non-contact IR (infrared) thermal imaging is a potential means for sheet temperature characterization that is currently employed by some in the thermoforming industry. However, the effectiveness of thermal

mapping lies with its incorporation into the heater controls to build a real-time sensing and control sub-system.

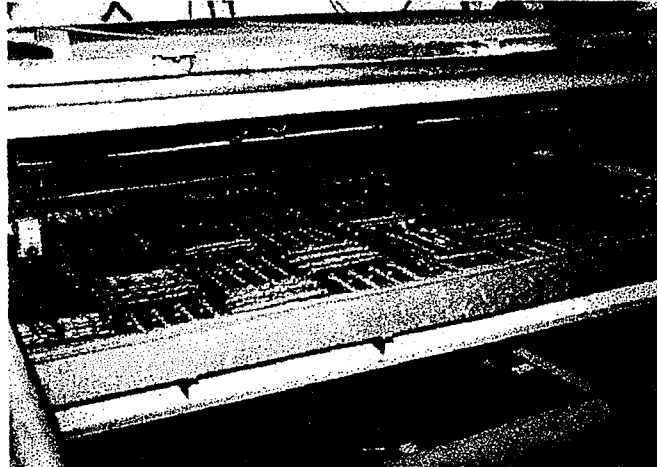


Figure 1.7 : Zone-Heaters Incorporated in a Thermoforming Machine.

Ideally, this design will attain an intended or optimal heat pattern before the polymer sheet forms into the mold.

The accurate characterization of sheet temperature will improve the predictions of material deformation via process modeling.

Process parameter optimization can be obtained through numerical simulations without wasteful "trial & error" experimental tests. Currently, the scope of process simulation, particularly finite element analysis of heating and deformation, has expanded in the thermoforming industry. Several software companies have been refining their modeling codes in order to include multi-layer and reinforced materials, predict heating and cooling times, consider shrinkage and warpage, and simulate twin-sheet forming. Presently, the forerunners of commercial thermoforming software are Polydynamics' *T-formcad*, Compuplast's

mapping lies with its incorporation into the heater controls to build a real-time sensing and control sub-system.

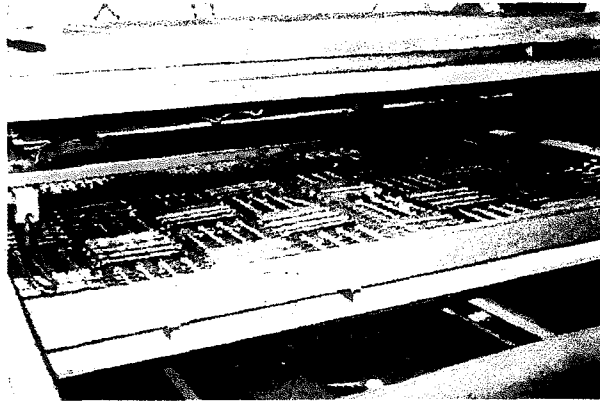


Figure 1. 7 : Zone-Heaters Incorporated in a Thermofforming Machine.

Ideally, this design will attain an intended or optimal heat pattern before the polymer sheet forms into the mold.

The accurate characterization of sheet temperature will improve the predictions of material deformation via process modeling.

Process parameter optimization can be obtained through numerical simulations without wasteful "trial & error" experimental tests. Currently, the scope of process simulation, particularly finite element analysis of heating and deformation, has expanded in the thermofforming industry. Several software companies have been refining their modeling codes in order to include multi-layer and reinforced materials, predict heating and cooling times, consider shrinkage and warpage, and simulate twin-sheet forming. Presently, the forerunners of commercial thermofforming software are Polydynamics' *T-formcad*, Compuplast's

T-SIM 4.0, *Fluent's Polyflow 3.7*, and *C-Mold*. New thermoforming software packages are also being developed at the University of Massachusetts at Amherst, and The Industrial Materials Institute of the Canadian National Research Council (IMI-CNRC) [10].

Sagging, shrinkage, and warpage of heated polymer sheets are properties inadequately studied in thermoforming. A handful of journal articles exist describing experimental and numerical efforts focused on these heating and cooling quandaries that are so important to part quality [4, 11]. Excessive sag may cause overheating and premature stretching prior to forming. Heated sheets in the rubbery and glassy states succumb to shrinkage and warpage as a result of residual stresses. So far, a limited number of shrinkage and warpage modeling through FE analyses (elastic, hyperelastic) has been developed, whereas the research in sheet sag has been entirely empirical.

1.3 Motivation behind the Current Research Investigations

Large-part thermoforming of multi-layer materials has produced a flourish of opportunities related to this manufacturing process. For three consecutive years, the annual 6.5% average increase in the amount of thermoformed parts is primarily the responsibility of heavy-gauge custom thermoforming. Additionally, a 1998 survey reported that custom thermoforming in North America consumes 834 million lbs. of heavy-gauge sheet, mainly ABS and HDPE (High-density polyethylene). The growth in

heavy-gauge sheet forming of large parts has propelled some enhancements in thermoforming for the processing of multi-layered, reinforced, and filled materials.

The capabilities of thermoforming are largely untapped. The successful characterization of the heated sheet will enhance the understanding of this process by linking the temperature parameter to the final thickness distribution. This finding will improve such applications as deep drawing and complex mold geometry, making thermoforming a formidable, economical alternative to injection molding.

The current research is also aimed at eliminating the industrial practice of "trial and error". Figure 1.8 illustrates the proposed concept for improved thermoforming. With the introduction of zone-heating, operator experience has become an unfortunate factor for successful thermoforming. By manually operating and monitoring the forming process, much guesswork is involved in obtaining the optimal processing parameters. Therefore, the use of a sensing and control sub-system can effectively replace the inefficient craft of hand-operated heater settings. With "trial & error" relinquished, further manufacturing costs would be reduced.

The introduction of automation into the heating controls will evidently save energy and curb material waste. A sensing and control sub-system could effectively regulate the heating process without the wasteful tests involved in "trial & error" practices.

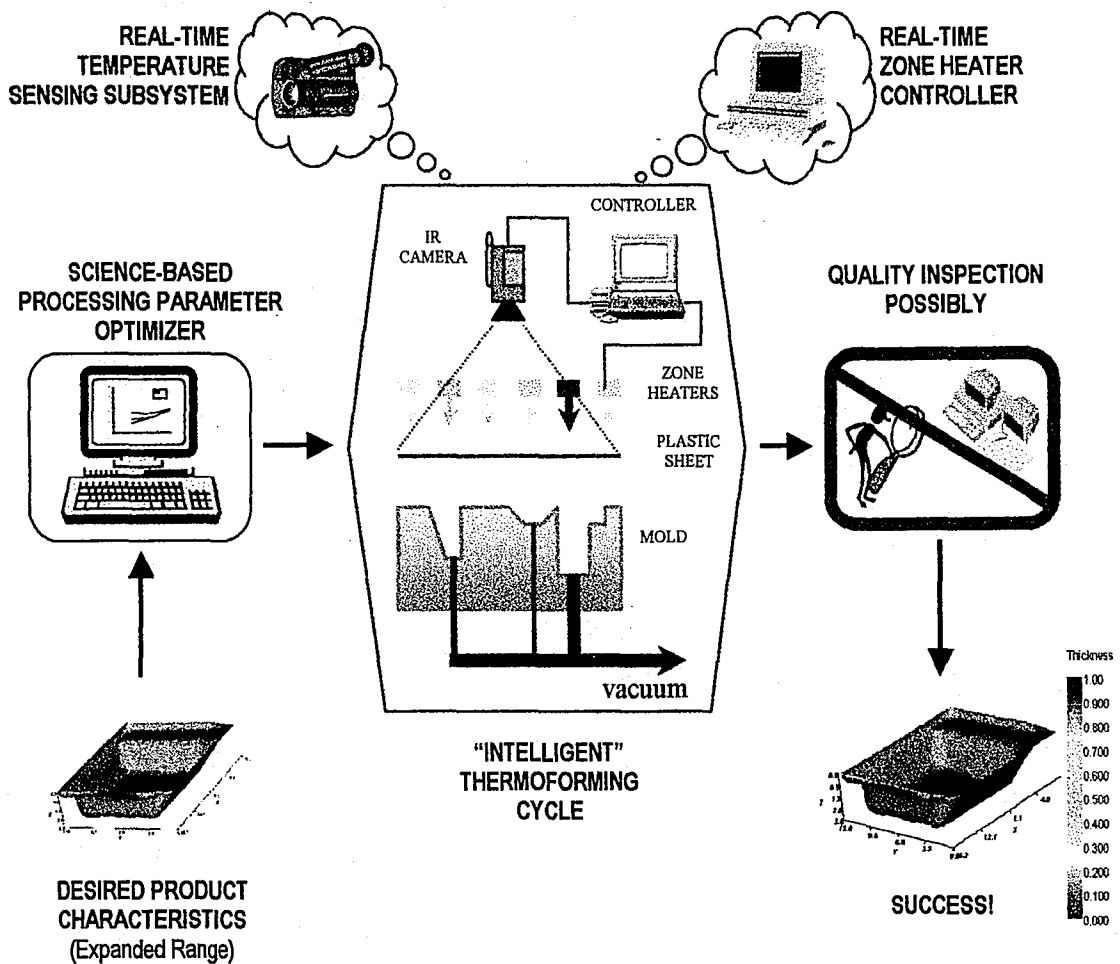


Figure 1. 8 : A Diagram of the Proposed Sensing & Controls System for Zone-Heating Thermoforming. The loop starts from the bottom left and finishes on the bottom right, without excessive reiterations nor product quality inspections.

For instance, when the camera detects an undesired hot or cold zone on the plastic sheet, the corresponding controller will adjust the proper zone heaters in order to attain the prescribed heat pattern. A survey by Plastics Custom Research Services reported a rise in process control and automation in the thermoforming industry[6]. Recently, some cost-redeeming applications of temperature sensing technology can be found in the thermoforming industry. For instance, a customer of Geiss,

German machine-maker, reduced their material scrap rate by 3% with the use of a pyrometer-based, closed-loop temperature sensing system. Eventually, an annual \$65,000 was saved by employing this \$30,000 IR scanner[12]. A real-time heating control system is intended to eliminate scrap material by "Intelligent Thermoforming"; the concept of sensing and control for acquiring the desired heat patterns prior to deformation.

Finally, this research thesis will further enforce the delivery of science into the thermoforming process. The industry is clearly ahead of its science in this nicknamed "old timer" among plastics forming processes, as evident from the dependence on repetitive tests in commercial applications and empirical observations in journal papers. A puissant thermoforming system will emerge through the synthesis of the thermal imaging and control capability with the numerical simulation of the sheet deformation. At GE Plastics, some new progress was noted in the process simulation methods to predict thinning and shrinkage of multi-layer sheets. In short, the introduction of science-based insight into thermoforming, like solving heat transfer equations with appropriate boundary conditions or accounting for the radiant transmissivity of semi-transparent material, will bridge the gap between our academic research and this plastics manufacturing industry.

1.4 Scope of Current Research

The research conducted during the present study was an initial step of an estimated multi-investigator and multi-year project which will conclude with the realization of a robust real-time sensing and control sub-system for zone-heater based thermoforming processes. The first phase involved the establishment of an IR thermal imaging system for opaque (PP) and nontransparent (ABS) polymer sheets. For experimentation and initial system development purposes, the IR imager was mounted above the forming area. In the future, it is planned that the IR camera will eventually be mounted at an angle in order to "see" the plastic sheet during the heating process, which occurs between two sandwiching radiant heaters. During the present study, thermal images were obtained within the intended field-of-view (FOV), and temperature measurements were carefully calibrated. With the established thermal mapping technology, sheet temperature images were then obtained for a variety of permutations of zone heater settings. The goal of doing so was to determine the range of complexity of sheet temperature patterns that can be obtained with a given zone heater configuration.

In an effort to better understand zone heating based capabilities, a numerical heat transfer modeling component was also included as part of the investigation. Numerical results were generated to identify zone heater patterns yielding both uniform and spatially variant sheet temperature distributions.

When possible, the validity of the numerical results obtained was evaluated through a direct comparison with experimental results.

The remaining portions of the thesis are organized as illustrated in Figure 1.9.

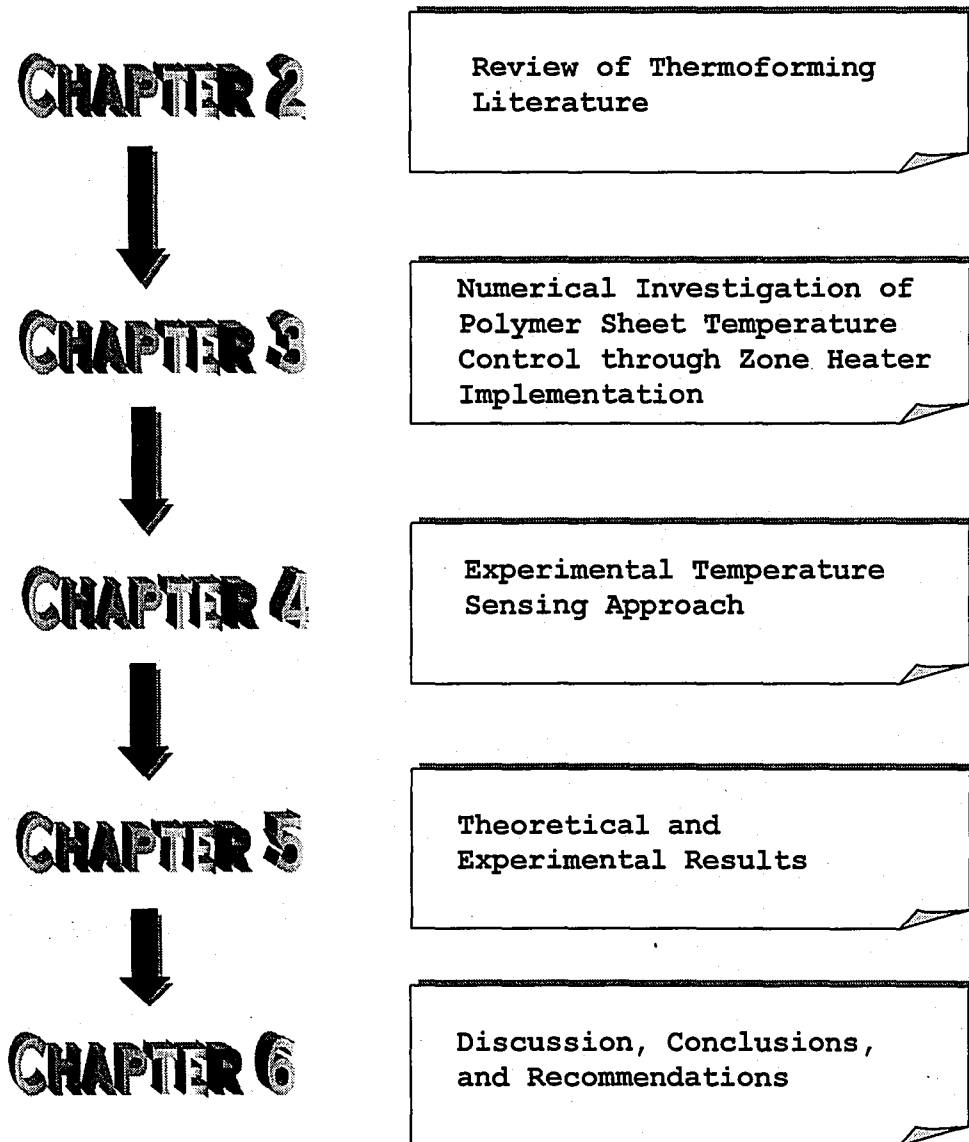


Figure 1.9 : A Summary of the Organization of the Thesis.

CHAPTER 2

REVIEW OF THERMOFORMING LITERATURE

Industrial and scientific developments related to thermoforming have been reviewed through a comprehensive examination of journal articles, conference proceedings, and text books. The present chapter summarizes the important findings related to the current study. Figure 2.1 illustrates some of the critical thermoforming research areas in industry today:

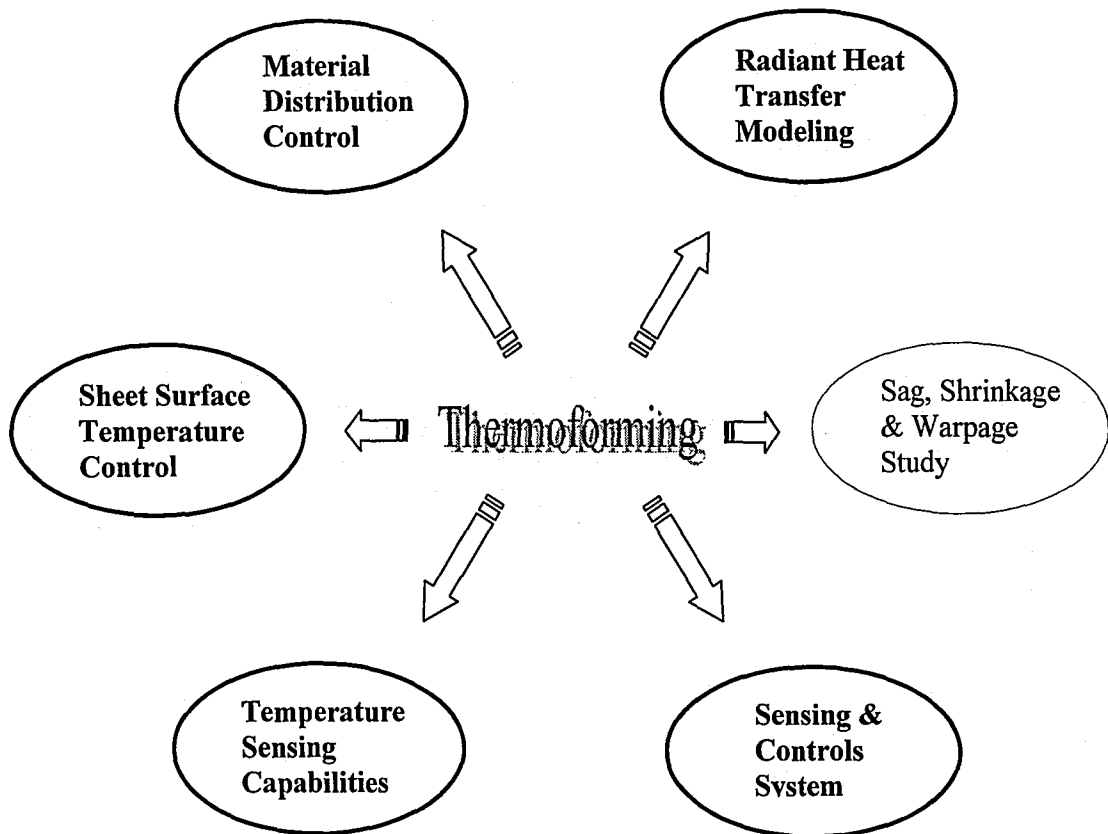


Figure 2. 1 : The Areas of Active Thermoforming Research.

The five areas of interest for this thesis are highlighted in Figure 2.1. The following sections review the progress in each of these areas. In each case, the review is preceded by a list of authors who have contributed to the respective areas.

2.1 Material Distribution Control in Thermoforming

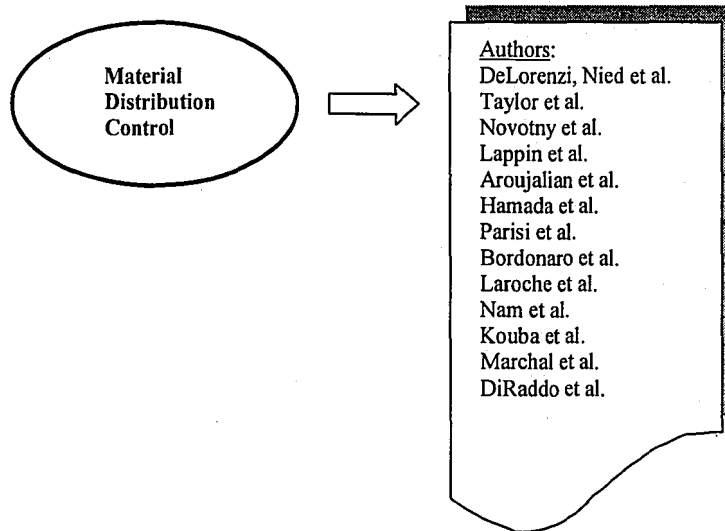


Figure 2. 2 : Some Contributing Authors for Material Thickness Control

The current interest in thermoforming research has led to much process experimentation and theoretical modeling, though the former is dominant. Nevertheless, the control of desired material distribution has been approached in several ways. Industrial experience has led to the popular plug-assisted vacuum-forming technique that offers more uniform material distribution, especially at the corners[13], than straight thermoforming. This experimental approach has been focused on during investigations

that attempted to optimize the plug-device[14-17]. The shape, size, and speed of the plug were found to influence the uniformity of the final sheet thickness. Other attempts at optimizing the thermoforming operation were made on process parameters such as the pre-stretch bubble height, sheet temperature, mold temperature, stretching and heating rate, delay time prior to forming, and evacuation rate[18]. Bordonaro, et al. designed a set of experiments that supported the significance of the first three forming variables towards acceptable parts[7].

Material distribution and energy consumption issues have also been addressed through analogous numerical simulations. Finite element analysis is a popular modeling tool that has been applied to thermoforming[19-23]. deLorenzi, et al. developed a simulation software package capable of predicting final part thicknesses[13]. Their finite element program modeled a nonlinear elastic polymer membrane and produced results that correlated well with experimental data. The Mooney-Rivlin and Ogden material model formulations were applied. This was also done by the group led by Taylor[8]. This group attributed existing, though small, discrepancies to the lack of time-dependent temperature information throughout the deforming membrane, and the need for better comprehension of actual temperature-dependent material behavior. They concluded that the elusive temperature distribution information represents the key to a more precise numerical simulation of thermoforming. Furthermore, their

investigation on a rectangular box formed with different thermoplastics suggested that mold geometry, as opposed to material properties, most greatly influences the final thickness distribution.

Marchal, et al. investigated some optimal thermoforming conditions using the computational code POLYFLOW[24]. Since numerical simulation permits the exploration of numerous forming parameters and their influence on final part, the worst that could come of it is a satisfying set of conditions to begin an experimental or production run. They suggested more complex sheet temperature patterns to further improve the part thickness distribution.

Other researchers have structured combined experimental and numerical investigations in an effort to predict final thickness distribution. Recognizing the inadequate characterization of the heating stage, in other words the lack of sheet temperature information, Taylor, et al. and DiRaddo, et al. combined numerical computation and temperature sensing tools to achieve desired quality parts[8, 25]. In Taylor's group, infrared thermography and finite element modeling were employed to investigate the influence of process variables such as evacuation rate (vacuum), sheet surface temperature, mold temperature, and material slip over the mold surface. An infrared imager, which is a non-contact thermal mapping device, provided temperature information for the major areas of the sheet as it was positioned

above the mold. The finite element model assumed a flat (neglecting sag) sheet with uniform initial temperature accomplished through zone-heating. The sheet boundary conditions were found to influence the thickness distribution since additional unrestrained material could potentially slide into the mold cavity. They also suggested a deeper understanding of biaxial material properties (like polymer stretching at high temperatures and strain rates) since their approximate model is based on uniaxial material data.

DiRaddo, et al. simulated the process with a combination of heating, sagging, and forming numerical models. The K-BKZ viscoelastic model, generally accepted for representing molten state polymer deformations, was used to predict the sheet forming as well as sheet sag. In brief, finite element models, supported by validating experimental measurements, were made for the radiant sheet heating and the deformation stage, individually. The calculated heating results were experimentally verified before being utilized for a subsequent simulation of the forming stage. Additionally, a sensitivity analysis, capable of establishing a relation between input parameters and part quality, was performed in an attempt to move towards overall process optimization.

2.2 Radiant Heat Transfer Modeling

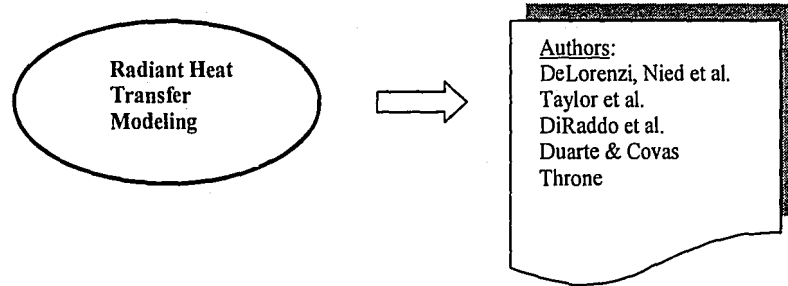


Figure 2.3 : Some Contributing Authors for Radiant Heat Transfer Modeling

As suggested in section 2.1, the temperature distribution throughout the polymer has a major effect on the deformation process. Since the deformation of the polymer sheet determines its final thickness distribution, deLorenzi, et al.[13] confirmed that the single most important variable in improving material distribution analysis is the polymer temperature gradient. They also suggested that "[a] more complete approach would be to perform a transient thermal analysis simultaneously with the inflation [or deformation] analysis," which was attempted by Diraddo, et al.[25]. Today, two apparent sources of radiant heat transfer models for thermoforming exist.

Duarte and Covas[26] solved the one-dimensional non-steady (transient) heat conduction problem through the sheet thickness while accounting for radiative and convective boundary conditions. The free convection cooling on the heater-exposed surface was neglected. As part of their work, a method for computing shape factor fields for any two parallel surfaces was

developed. Their thermoforming set-up consisted of one radiant heater in parallel, and directly opposed to the target sheet. The differential or zone-heating ability was included in their numerical analysis. The fully implicit finite difference method, with central difference approximations, was employed to solve for the transient temperature as a function of heating time. As observed by other findings[27], the sheet temperature decreases from the center to the edges when a uniform heater setting is imposed. Furthermore, as the heater-to-sheet distance increases, the polymer surface temperature gradient decreases in a non-linear fashion.

In addition to solving the direct problem, as described above, Duarte and Covas also took on the task of proposing the solution to a more complex inverse heating problem in thermoforming. Briefly, this particular inverse problem is defined as solving for the heater temperatures (individually controllable) from a prescribed, desired uniform sheet temperature. Their results were contour plots of heater temperature settings that would heat a polymer sheet to a uniform temperature after a specified time. Finally, they suggested an amalgamation of their inverse heating algorithm with a sheet deformation counterpart that will conceptually provide a robust numerical model for the entire thermoforming process.

The other current source of transient heat transfer calculation comes from a thermoforming consulting company called

Sherwood Technologies Inc. in Ohio, U.S.A. Dr. James Throne produced an explicit finite difference program in the QBasic computer language, TF505[28], that outputs the heating time for creating a more uniform sheet temperature distribution. Similar to Duarte and Covas, the one-dimensional transient heat conduction model was used. However, top and bottom heaters (individually controllable) that "sandwich" the sheet can be specified. The radiative and convective boundary conditions can be applied to both the upper and lower sheet surfaces[29].

One of the capabilities intrinsic to Throne's computer code is the user specification of numerous forming parameters, including material properties. Chapter 3 contains a list of these forming variables. The program conveniently incorporates a database of 34 polymers that could be selected for the heating calculations. A potential shortcoming of the program, however, is that it assumes a biaxial heater symmetry that limits the temperature specification to only one quadrant of each heater pattern. Furthermore, some simplification is made on the view factor for finite planar gray bodies. The TF505 program is designed towards the generation of a uniform sheet temperature distribution, as the program terminates when the average sheet temperature exceeds the normal forming temperature.

2.3 Sheet Surface Temperature Control through Zone-Heaters

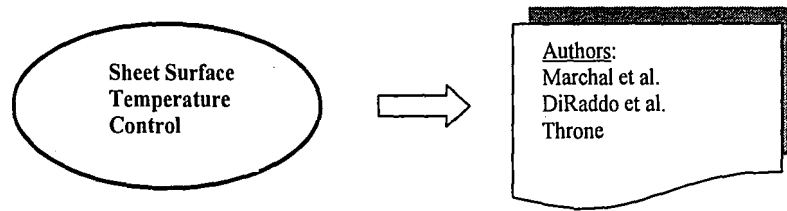


Figure 2. 4 : Some Contributing Authors for Sheet Surface Temperature Control

Zone-heating in thermoforming was originally conceived of to obtain a more uniform sheet surface temperature distribution. In their simulation of thermoforming, Marchal, et al. Sought to yield lower temperatures at thinner portions of the sheet to induce a higher local viscosity. This, accordingly, would locally increase the region's resistance to deformation and further thinning[24]. This phenomenon was confirmed numerically and experimentally by Diraddo, et al.[25] and Throne[29].

In a thermoforming investigation of 7x7 zone heating elements, Throne made several observations regarding the effects of local energy interchange and sheet-to-heater distance on sheet temperature. After several heater adjustments, a uniform heat flux to the whole sheet, within $\pm 1.5\%$, was achieved[29]. Moreover, it was recorded that "a 28% increase in heat flux no a given element resulted in a 7% increase in heat flux to the elements immediately surrounding it, and a 3% increase to elements surrounding those elements[27]." Throne also concluded

that excessive spacing between heater and sheet is inefficient to energy consumption. Heater-to-sheet spacing should only be restrained by maximum sheet sag and the prevention of local overheating.

2.4 Temperature Sensing Capabilities

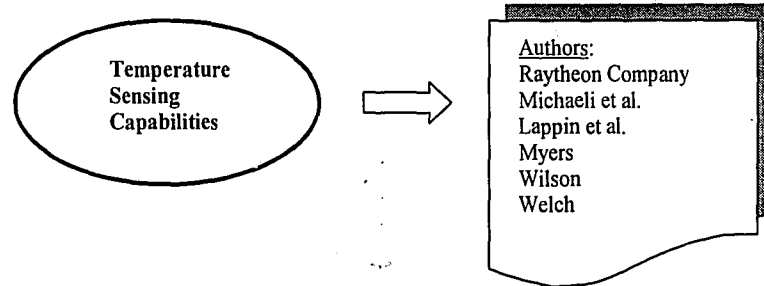


Figure 2. 5 : Some Contributing Authors for Temperature Sensing Capabilities

Upon realizing the significance of sheet temperature characterization prior to thermoforming, industrial and academic engineers have explored numerous non-contacting temperature sensing systems[30,31]. Geiss[12] integrated an infrared scanning pyrometer system in their commercial thermoformers that scans "lines" of temperature as the sheet exits the heaters into the forming area. The so called IR linescanners can detect an array of 4096 (64 x 64) thermal points on the pre-heated polymer. A complementary software package, linked directly to the IR linescanner, displays the temperature profile as a color thermogram. The temperature line-scanning technology has been

implemented elsewhere[9, 31]. Single and multi-point pyrometer systems have been deployed and tested[12, 32, 33].

The infrared thermal imager is an accurate temperature sensing tool that affords very high resolution (320 X 240 pixels). It is comparably a "video camera" that detects IR emission instead of visible light. Raytheon, currently as the major producer of IR thermal imagers, offers imaging devices that cover different ranges of radiation wavelengths for a variety of applications, from process monitoring and construction to security[34]. Taylor's group situated an IR imager at a perpendicular view of the forming area to create a time-dependent sheet thermograph[8]. They recognized the limitations of infrared imaging of the complete sheet during the heating stage. Although successful thermal maps were taken after the heating process and during vacuum deformation, substantial error is admitted in the corners where a distorted view factor prevailed.

DiRaddo, et al. mentioned the use of an infrared camera for temperature measurements after the heating stage[25]. The temperature profile error noted along the sides of the sheet is attributed to the heat-sinking clamping frame. The reader is reminded that these temperature sensing systems measure only the surface information. The utilization of these measurements as the bulk temperature for "thick" material requires some detailed heat conduction analysis to maintain the integrity of the results.

2.5 Sensing & Control Systems in Thermoforming

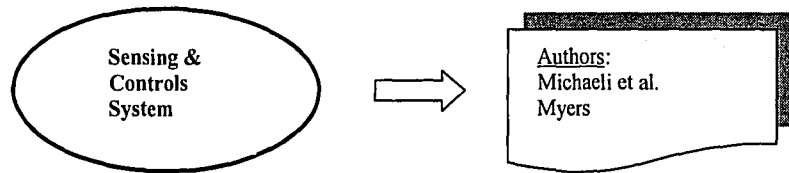


Figure 2. 6 : Some Contributing Authors for Sensing & Controls System

Michaeli and Marwick designed a closed-loop control system that automated the thermoforming process to achieve the required temperature profile for quality parts[9]. The measured sheet temperatures were used jointly with the desired profile to calculate a new set of heater values for the next cycle. Naturally, some waste was created between the adjacent cycles when a new set of "improved" heater settings attempted to achieve the prescribed temperature profile. Other closed-loop scanning systems[12] have also attempted to improve the quality of thermoformed parts.

Despite these few industrial attempts, the deployment of temperature sensing and control systems for thermoforming in industry remains a relatively uncharted territory. The current research investigation was performed in an attempt to contribute to the advancement of thermoforming science and the future realization of fully intelligent thermoforming processes. The presentation of the investigation begins with a description of the related heat transfer theory in the following chapter.

CHAPTER 3

NUMERICAL INVESTIGATION OF POLYMER SHEET TEMPERATURE CONTROL THROUGH ZONE HEATER IMPLEMENTATION

3.1 Theoretical Development

Prior to the delving into an analysis of radiative heat transfer between two surfaces, namely the heater and the sheet during thermoforming processes, an introduction to a parameter called the view factor (or shape factor) is in order. The view factor, denoted as F_{ij} , is defined as "the fraction of the radiation leaving surface i that is intercepted by surface j " [35]. The following theoretical development focuses on proper view factor determination and is tailored specifically for the respective heater and sheet surfaces, A_h and A_s , that are common in zone-heating thermoforming machines. Prior to describing the view factor, the radiative energy exchange between black bodies is discussed.

3.1.1 Radiation Exchange between Black Bodies

First, two "black surfaces" are considered. This idealization implies perfect emissivity ($\epsilon=1$) for both surfaces. Then, two differential areas, dA_h and dA_s , linked by an imaginary line, r , are defined in Cartesian coordinates as shown in Figure 3.1.

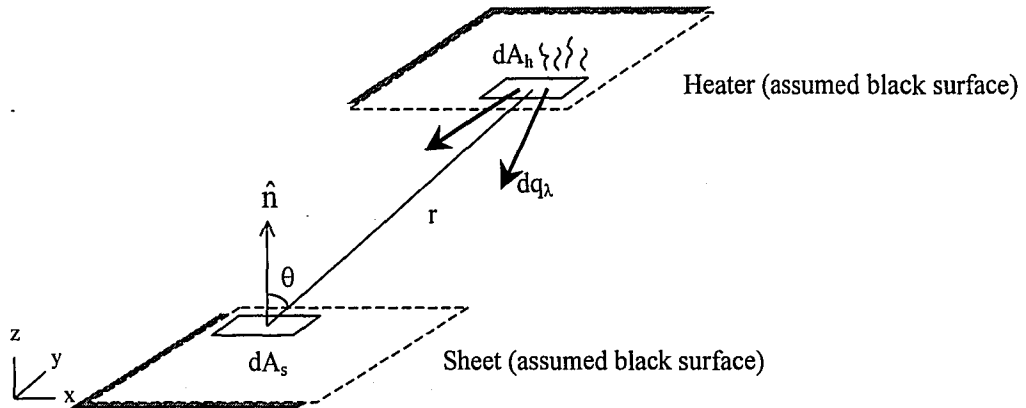


Figure 3. 1: Zone Heating Differential Elements in 3-Dimensional Cartesian Coordinates.

Note that the normals for both differential areas (only drawn for dA_s) create an identical angle θ with the line r . Now, let's introduce the quantity of emitted radiation from black body dA_h as a spectral intensity, $I_{b\lambda}$. $I_{b\lambda}$ is defined as "the rate at which radiant energy is emitted at the wavelength λ in the (θ, ϕ) direction, per unit area of the emitting surface normal to this direction, per unit solid angle about this direction, and per unit wavelength interval $d\lambda$ about λ " [35]:

$$I_{b\lambda} = \frac{dq_\lambda}{(dA_h \cos \theta) d\omega} \quad (3.1)$$

with units $\left(\frac{W}{m^2 \cdot sr \cdot \mu m} \right)$. The numerator, dq_λ , is the rate at which the radiation of wavelength λ leaves dA_h and passes through the area " $(dA_h \cos \theta)$ ". This area, utilized in the spectral intensity

definition, is the projection of dA_h normal to the radiation direction, as illustrated in Figure 3.2.

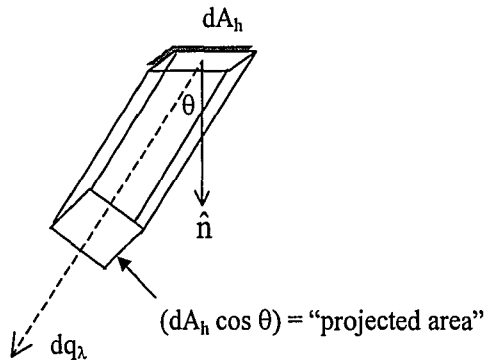


Figure 3. 2: Projected Area of Differential Heater Element, dA_h .

The total radiation from dA_h to dA_s is obtained by integrating equation (3.1) over all wavelengths, from zero to infinity:

$$\int_0^{\infty} I_{b\lambda} d\lambda = \int_0^{\infty} \frac{dq_\lambda}{(dA_h \cos \theta) d\omega} d\lambda \quad (3.2)$$

$$\Rightarrow \int_0^{\infty} I_{b\lambda} d\lambda = \frac{1}{(dA_h \cos \theta) d\omega} \int_0^{\infty} dq_\lambda d\lambda \quad (3.3)$$

Since $I_b = \int_0^{\infty} I_{b\lambda} d\lambda$, and $dq = \int_0^{\infty} dq_\lambda d\lambda$, the total intensity of emitted radiation becomes:

$$I_b = \frac{dq}{(dA_h \cos \theta) d\omega} \quad (3.4)$$

Rearranging equation (3.4),

$$dq = I_b (dA_h \cos \theta) d\omega \quad (3.5)$$

where dq is the rate of radiation from dA_h and received by dA_s .

Let's clarify the $d\omega$ term. The solid angle, $d\omega$, is illustrated in Figures 3.3 and 3.4:

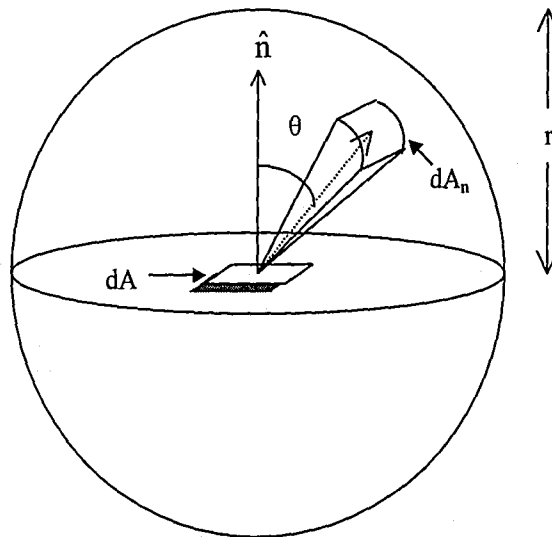


Figure 3. 3: Radiation Emitted by dA that passes through a small area dA_n .

Considering only the top hemisphere of Figure 3.3, all the radiation emitted from the area dA must reach this imaginary hemispherical surface. Every small area on the hemispherical surface, like dA_n , subtends a solid angle at dA . An isolated view of this is shown in Figure 3.4. Mathematically, the solid angle is determined from the relationship

$$d\omega = \frac{dA_n}{r^2} \quad (3.6)$$

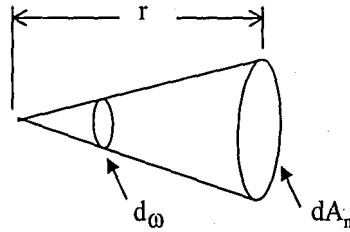


Figure 3. 4: Definition of the Solid Angle.

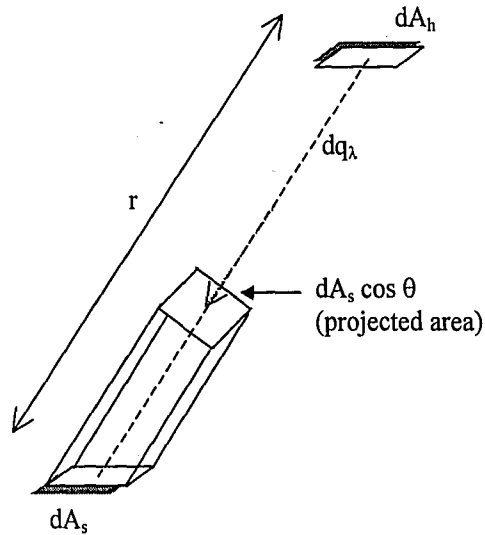
with a corresponding unit of steradian (sr). In other words, the solid angle for dA_n is the area of dA_n divided by r^2 . For instance, the solid angle for the top hemisphere is 2π steradians (from $2\pi r^2$ divided by r^2). In our special case, $d\omega$ is the solid angle that dA_s subtends as "seen" from dA_h .

For thermoforming processes, the view of dA_s from dA_h is a projected area of the sheet element, as illustrated in Figure 3.5. Therefore, since $dA_n = dA_s \cos \theta$, equation (3.6) provides our thermoforming specific definition of the solid angle as

$$d\omega = \frac{dA_s \cos \theta}{r^2} \quad (3.7)$$

Substituting this into equation (3.5) yields

$$dq = I_b (dA_h \cos \theta) \frac{dA_s \cos \theta}{r^2} \quad (3.8)$$



where dq_λ = rate of radiation at wavelength λ leaving dA_h
 θ = zenith angle
 $d\omega$ = solid angle subtended by the dA_s when viewed from dA_h

Figure 3. 5: Diagram of the Projected Sheet Area View from the Heater Element.

Next, in the development of the view factor, equation (3.8) will be used to obtain the net radiation exchange between the heater and sheet differential elements. Of course, these derivations are still made with the black body idealization. The relationship between total emissive power of a black surface, E_b , and total black body spectral intensity, I_b [36] is

$$E_b = \pi \cdot I_b \quad (3.9)$$

Substituting this relation and the equation for $d\omega$ into equation (3.8) yields

$$dq_{dA_h \rightarrow dA_s} = \frac{E_b}{\pi} \frac{(dA_h \cos \theta) dA_s \cos \theta}{r^2} \quad (3.10)$$

Note that the subscripts for dq , " $dA_h \rightarrow dA_s$ ", describe the direction of radiant energy leaving dA_h that is incident on dA_s . Now, by applying the Stefan-Boltzmann law of thermal radiation, $E_b = \sigma \cdot T^4$ [37], equation (3.10) becomes

$$dq_{dA_h \rightarrow dA_s} = \frac{\sigma T_h^4}{\pi} \frac{(dA_h \cos \theta) dA_s \cos \theta}{r^2} \quad (3.11)$$

This expression describes the radiation leaving dA_h (heater surface) and incident on dA_s (sheet surface) with a new T_h variable.

Since any surface at a temperature above 0 Kelvin emits radiant energy, some emission does radiate from the sheet element to the heater element. By referring to equation (3.11), an analogous equation can be derived for the radiation from dA_s that is incident on dA_h :

$$dq_{dA_s \rightarrow dA_h} = \frac{\sigma T_s^4}{\pi} \frac{(dA_s \cos \theta) dA_h \cos \theta}{r^2} \quad (3.12)$$

Finally, the net radiation exchange between dA_h and dA_s is the difference between $dq_{dA_h \rightarrow dA_s}$ and $dq_{dA_s \rightarrow dA_h}$ or equation (3.11) minus equation (3.12)

$$dq_{dA_h \Rightarrow dA_s} = (\sigma T_h^4 - \sigma T_s^4) \cdot \frac{(\cos \theta)^2 dA_h dA_s}{r^2} \quad (3.13)$$

If there exists "n x m" number of heater elements possessing temperatures $T_{h, nm}$ and small areas $dA_{h, nm}$, the energy exchange between all the heater elements and dA_s becomes

$$q_{A_h \Rightarrow dA_s} = \sum_{n,m} dq_{dA_{h, nm} \Rightarrow dA_s} \quad (3.14)$$

or

$$q_{A_h \Rightarrow dA_s} = \frac{\sigma}{\pi} \sum_{n,m} (T_{h, nm}^4 - T_s^4) \cdot \frac{(\cos \theta)^2 dA_{h, nm} dA_s}{r^2} \quad (3.15)$$

The term $dA_{h, nm}$ denotes a single heater element. Supposing that there are "j x k" sheet elements, the terms " $dA_{s, jk}$ " and " $T_{s, jk}$ " can be introduced into equation (3.15) to yield

$$q_{A_h \Rightarrow dA_s} = \frac{\sigma}{\pi} \sum_{n,m} (T_{h, nm}^4 - T_{s, jk}^4) \cdot \frac{(\cos \theta)^2 dA_{h, nm} dA_{s, jk}}{r^2} \quad (3.16)$$

3.1.2 Introduction to the View Factor

With the derivation of equation (3.13) now complete, the view factor can be formally defined. For the differential areas dA_h and dA_s , the view factor, $F_{dA_h \rightarrow dA_s}$, is the fraction of energy leaving dA_h that strikes dA_s :

$$F_{dA_h \rightarrow dA_s} = \frac{dq_{dA_h \rightarrow dA_s}}{E_b \cdot dA_h} \quad (3.17)$$

Substituting equation (3.10) into this expression,

$$F_{dA_h \rightarrow dA_s} = \frac{E_b (dA_h \cos \theta) dA_s \cos \theta}{\pi r^2} \cdot \frac{1}{E_b \cdot dA_h} \quad (3.18)$$

or

$$F_{dA_h \rightarrow dA_s} = \frac{\cos^2 \theta \cdot dA_s}{\pi r^2} \quad (3.19)$$

Analogous equations for the view factor can be written for the radiative fraction from the heater to the sheet, F_{hs} :

$$F_{hs} = \frac{\cos^2 \theta \cdot A_s}{\pi r^2} \quad (3.20)$$

Similarly, the radiative fraction from the sheet that is incident on the heater can be expressed as follows,

$$F_{sh} = \frac{\cos^2 \theta \cdot A_h}{\pi r^2} \quad (3.21)$$

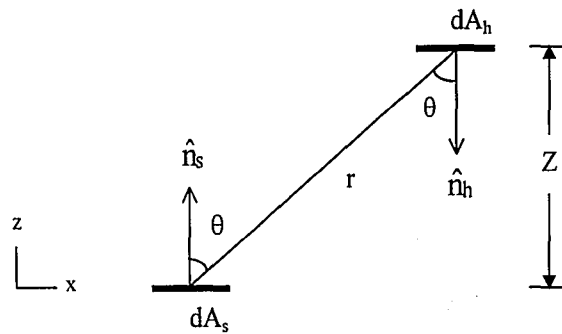
Equations (3.20) and (3.21) lead to an important view factor relation called the reciprocity relation[38],

$$A_h F_{hs} = A_s F_{sh} \quad (3.22)$$

or more generally,

$$A_i F_{ij} = A_j F_{ji} \quad (3.23)$$

From Figure 3.1, $r^2 = X^2 + Y^2 + Z^2$, where X, Y, and Z are unit spaces between the differential areas in the x, y, and z-directions respectively. Figure 3.6 illustrates, two dimensionally, the parameters involved in the derivation of the view factor, F_{hs} , for the heater element as "seen" from the sheet element.



dA_s = sheet differential area θ = angle between sheet area normal and r
 dA_h = heater differential area Z = vertical distance between differential areas
 r = linear distance between differential areas

Figure 3. 6 : 2-D Representation of Heater and Sheet Element Geometry.

3.1.3 Radiation Exchange between Gray Bodies

At this point, the idealization of our theoretical details shall accommodate for some imperfections in reality. The black body assumption for surfaces is an approximation for materials in the physical world where emissivity, ϵ , is less than perfect ($\epsilon < 1$). Thus, the gray body approach will be used in the developments that follow.

Some complications in analyzing radiation exchange arise when gray (non-black) surfaces reflect energy. For an opaque, diffuse, gray surface, $(\rho + \alpha) = 1$ where,

ρ = reflectivity, or portion of reflected radiant energy,

α = absorptivity, or portion of absorbed radiant energy.

This assumes no transmissivity through the surface (opaque). A diffuse surface is one in which the absorptivity (α) is equal to the emissivity (ϵ) [36]:

$$\epsilon(T) = \alpha(T) \quad (3.24)$$

Furthermore, the emissivity and absorptivity of a gray surface do not vary with wavelength.

The previous paragraph described several quantities that will be used for the theoretical details to come. In aiding our description of the gray body radiation exchange, two flux

quantities with units $\left(\frac{\text{Btu}}{\text{hour} \cdot \text{ft}^2}\right)$ are introduced:

Radiosity (J) represents "the total radiant energy per unit time per unit area leaving a surface".

Irradiation (G) is "the rate at which radiant energy reaches a surface per unit time per unit area" [36].

The following developments will unfold with the assumptions that the gray surfaces are isothermal, and the radiosity and irradiation transpire uniformly. The net radiative flux q_i'' , lost by the surface i , is related to radiosity (J_i) and irradiation (G_i) by the subtraction of the former from the latter, or

$$q_i'' = (J_i - G_i) \quad (3.25)$$

Figure 3.7 illustrates the relationship between the three associated parameters. Moreover, the net radiative flux q_i'' may

also be written in terms of surface emissive power (E_i) and absorbed irradiation ($\alpha_i G_i$):

$$q_i'' = (E_i - \alpha_i G_i) \quad (3.26)$$

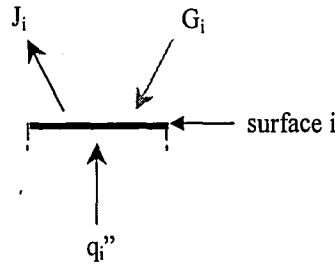


Figure 3. 7: Relationship between radiative flux, radiosity, and irradiation.

Combining equations (3.25) and (3.26) and maintaining the diffuse surface assumption (3.24), the following expression can be obtained:

$$q_i'' = \frac{E_{bi} - J_i}{\frac{1 - \epsilon_i}{\epsilon_i}} \quad (3.27)$$

Equation (3.27) above describes the heat transfer from an arbitrary surface i . The term " E_{bi} " represents the emissive energy for a black body I , where $E_i = \epsilon_i E_{bi}$.

A simpler, more straight-forward approach to present the gray body radiation problem is through the use of an electrical analogy. Figure 3.8 depicts a circuit analog of heat transfer from a surface i . The resistance, R_{surface} , accounts for the imperfect emissivity of the gray body :

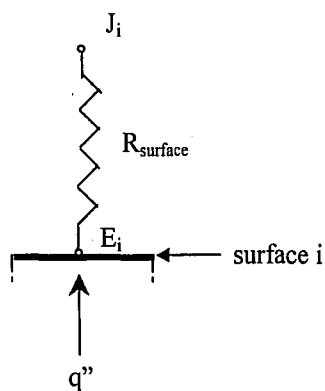


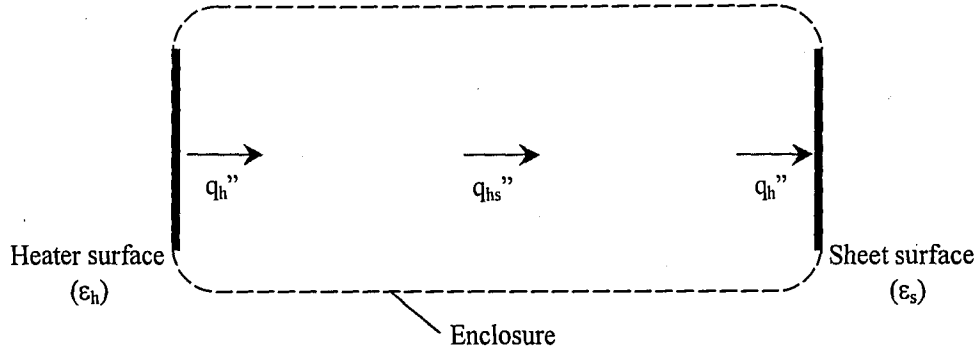
Figure 3. 8: Electrical Analog of Heat Transfer from a Surface i.

The net radiative transfer from surface i is defined as the ratio of the driving potential of heat flux from surface i, $(E_i - J_i)$, to the surface radiative resistance, R [35]:

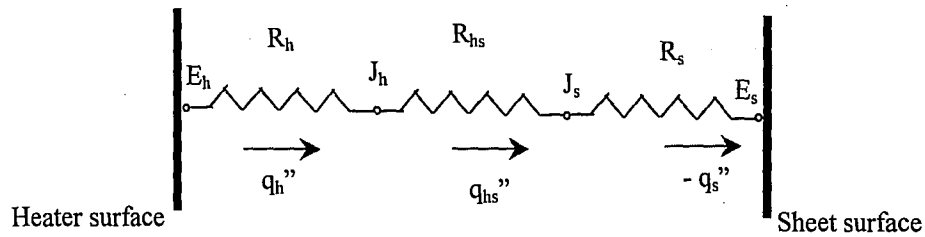
$$q_i'' = \frac{E_{bi} - J_i}{R} \quad (3.28)$$

where $R = \frac{(1 - \epsilon_i)}{\epsilon_i}$. This, of course, matches equation (3.27).

Applying this concept to our intended surfaces yields the thermal/electrical analogy illustrated in Figure 3.9. R_h refers to the " R_{surface} of the heater" whereas R_s applies to that of the sheet. R_{hs} , on the other hand, is the resistance from geometry (view factor), or " R_{geometry} between the surfaces". Now, the two surfaces of interest are first assumed to be in an enclosure, exchanging energy only with each other, as illustrated in Figure 3.9 (a).



(a)



(b)

Figure 3. 9: Electrical Analog between Heater and Sheet Elements (Gray bodies).

Therefore, the net heat transfer flux from the heater surface, q_h'' , must equal the net heat transfer flux to the surface sheet surface, $-q_s''$, and both quantities must also equal the net energy exchange flux, q_{hs}'' :

$$q_h'' = -q_s'' = q_{hs}'' \quad (3.29)$$

Applying equation (3.27), it may be concluded that

$$q_h'' = \frac{E_{bh} - J_h}{(1 - \epsilon_h) / \epsilon_h} \quad \text{and} \quad -q_s'' = \frac{J_s - E_{bs}}{(1 - \epsilon_s) / \epsilon_s} \quad (3.30)$$

Note that ϵ_h and ϵ_s symbolize the emissivity for the heater and sheet surfaces respectively. In order to use the equations from above, q_h'' , q_s'' , J_h and J_s would have to be known. To this end, consider, again, the radiation exchange between the heater and sheet in an enclosure. In this reiteration, allow the sheet to consist of 'K' number of elements, while leaving the heater to remain (the sum of all little heater elements into) one. The trick here is that the irradiation of the heater surface equals the sum of the radiosities from every surface (including the heater's radiosity). Therefore, this notion used jointly with the view factor definition yields the relation:

$$A_h G_h = \sum_{s=1}^K F_{sh} A_s J_s \quad (3.31)$$

From the reciprocity relation, equation (3.23), the above equation can be rewritten as,

$$A_h G_h = \sum_{s=1}^K F_{hs} A_h J_s \quad (3.32)$$

The areas, A_h , cancel each other. Substituting the result for G_h into a form of equation (3.25), $q_h'' = (J_h - G_h)$, yields

$$q_h'' = J_h - \sum_{s=1}^K F_{hs} J_s \quad (3.33)$$

Applying the conservation rule of radiation within an enclosure, or the summation rule, $\sum_{s=1}^K F_{hs} = 1$, the equation above becomes,

$$q_h'' = \sum_{s=1}^K F_{hs} J_h - \sum_{s=1}^K F_{hs} J_s \quad (3.34)$$

$$\Rightarrow q_h'' = \sum_{s=1}^K F_{hs} (J_h - J_s) \quad (3.35)$$

$$\Rightarrow q_h'' = \sum_{s=1}^K \frac{(J_h - J_s)}{1/F_{hs}} = \sum_{s=1}^K q_{hs}'' \quad (3.36)$$

Equation (3.36) expresses q_h'' as the sum of q_{hs}'' components exchanging radiation with the other surfaces in the enclosure. The denominator containing F_{hs} looks suspiciously like a resistance in an electrical analogy. In fact, the equation above may be represented as a ratio of a driving potential, $(J_h - J_s)$, to the geometrical resistance, $1/F_{hs}$. Returning to Figure 3.9(b),

and utilizing the circuit analogy, the radiation flux exchange between the heater surface and sheet surface experiences a potential $(E_{bh} - E_{bs})$ with two R_{surface} and an R_{geometry} :

$$q_{hs}'' = \frac{(E_{bh} - E_{bs})}{R_{h \text{ surface}} + R_{\text{geometry}} + R_{s \text{ surface}}} \quad (3.37)$$

$$\Rightarrow q_{hs}'' = \frac{(E_{bh} - E_{bs})}{\frac{1 - \epsilon_h}{\epsilon_h} + \frac{1}{F_{hs}} + \frac{1 - \epsilon_s}{\epsilon_s}} \quad (3.38)$$

Applying the Stefan-Boltzmann radiation law,

$$q_{hs}'' = \frac{\sigma(T_h^4 - T_s^4)}{\frac{1 - \epsilon_h}{\epsilon_h} + \frac{1}{F_{hs}} + \frac{1 - \epsilon_s}{\epsilon_s}} \quad (3.39)$$

Equation (3.39) can be re-written as,

$$q_{hs}'' = (F_{h-s} F_g) \sigma(T_h^4 - T_s^4) \quad (3.40)$$

where

$$(F_{h-s} F_g) = \frac{1}{\frac{1 - \epsilon_h}{\epsilon_h} + \frac{1}{F_{hs}} + \frac{1 - \epsilon_s}{\epsilon_s}} \quad (3.41)$$

If all the radiation leaving the heater reaches the sheet, i.e. infinitely planar gray bodies, then $F_{hs} = 1$, and equation 3.40 becomes:

$$q_{hs}'' = \frac{\sigma(T_h^4 - T_s^4)}{\frac{1-\epsilon_h}{\epsilon_h} + \frac{1-\epsilon_s}{\epsilon_s}} \quad (3.42)$$

or

$$q_{hs}'' = F_g \sigma(T_h^4 - T_s^4) \quad (3.43)$$

In equation (3.43) above, only the gray body emissivity factor F_g is included, where

$$F_g = \frac{1}{\frac{1-\epsilon_h}{\epsilon_h} + \frac{1-\epsilon_s}{\epsilon_s}} \quad (3.44)$$

Thus far, the theoretical developments of the view factor and net energy exchange between the two differential surfaces are made towards a more comprehensive understanding of surface heat transfer between parallel finite planes. In other words, the equations derived above will account for the energy interaction on the surfaces of the polymer sheet due to the radiation from the flat heaters. The heat transfer occurring within the sheet, however, is developed separately. The diffusion of heat through the polymer sheet will have a less extensive derivation, as it is

simplified into one-dimensional heat conduction through the sheet thickness.

3.2 Heat Transfer Governing Equations Applicable for Radiant Heating during Thermoforming

Radiant heating during thermoforming can be modeled by applying traditional conduction heat transfer governing equation with appropriate radiation and convection boundary conditions. Since the thermoplastic sheets of interest possess an "infinitely larger" width and length compared to their thickness, a one-dimensional heat conduction analysis is sufficient. Through the conservation of energy on a differential control volume, the heat conduction (or diffusion) equation becomes:

$$\rho C_p \frac{\partial T}{\partial t} = \frac{\partial}{\partial z} \left(k \frac{\partial T}{\partial z} \right) \quad (3.45)$$

where ρ = density (kg/m³)
 C_p = specific heat (J/kg.K)
 k = thermal conductivity (W/m.K)

Sometimes the material constants listed above are written as

$\alpha = \frac{k}{\rho \cdot C_p}$, or thermal diffusivity of the plastic. The z-direction

is through the thickness(L) of the sheet from top to bottom where

$0 \leq z \leq L$. The simplified one-dimensional heat equation, above,

is solved with an initial temperature condition and specified boundary conditions. The initial condition is as follows:

$$T(z,0) = T_i \quad \text{for } 0 \leq z \leq L \quad (3.46)$$

Since typical thermoforming machines have two sources of radiant zone-heating, the two surfaces of the polymer, top and bottom, are exposed to radiant energy exchange. Naturally, the view factor and gray body factor are included. Moreover, convective cooling boundary conditions are also imposed on the sheet surfaces. The boundary conditions are thus defined as follows:

$$\text{B.C. @ } z=0 \quad -k \frac{\partial T}{\partial z} = h_0 (T_{\text{air},0} - T_{s,0}) + F_{h-s} F_g \sigma (T_{h,0}^4 - T_{s,0}^4) \quad (3.47)$$

$$\text{@ } z=L \quad -k \frac{\partial T}{\partial z} = h_N (T_{\text{air},N} - T_{s,N}) + F_{h-s} F_g \sigma (T_{h,N}^4 - T_{s,N}^4) \quad (3.48)$$

where,

- k = thermal conductivity
- h_0 = heat transfer coefficient of air above the sheet
- h_N = heat transfer coefficient of air below the sheet
- $T_{h,0}$ = temperature of heater facing top sheet surface
- $T_{h,N}$ = temperature of heater facing bottom sheet surface
- T_s = temperature of sheet
- σ = the Stefan-Boltzmann constant ($5.67 \times 10^{-8} \frac{\text{W}}{\text{m}^2 \cdot \text{K}}$)
- F_{h-s} = the view factor between the heater and the sheet
- F_g = the gray body emissivity factor (unitless)

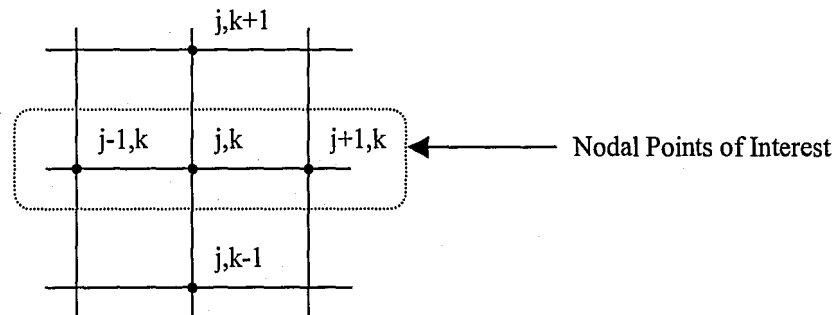
"0" denotes the top while "N" signifies the bottom sheet surface.

The above equation with associated boundary conditions can be solved numerically using a number of different approaches. The solution approach applied during the present investigation was the finite difference approach, which is briefly described in the next section.

3.3 Numerical Solution Approach

3.3.1 Discretization of the Governing Equation

First, the sheet is discretized into nodal points to obtain FD equations for the top sheet surface (node 0) through the material to the bottom surface (node N):



$$\frac{\partial T}{\partial t} = \frac{T_{j,k} - T_{j,k}}{\Delta t} \quad \text{and} \quad \frac{\partial^2 T}{\partial x^2} = \frac{T_{j+1,k} + T_{j-1,k} - 2T_{j,k}}{\Delta x^2}$$

Figure 3. 10: Discretization of One-Dimensional Heat Conduction through Finite Difference Approximation.

The heat conduction equation to be discretized comes from equation (3.45), which with the thermal diffusivity included is

$$\frac{\partial T}{\partial t} = \alpha \left(\frac{\partial^2 T}{\partial z^2} \right) \quad (3.49)$$

Substituting the discretization relations included in Figure 3.10 into the above heat conduction equation,

$$\frac{T'_{j,k} - T_{j,k}}{\Delta t} = \alpha \left[\frac{T_{j+1,k} + T_{j-1,k} - 2T_{j,k}}{\Delta x^2} \right] \quad (3.50)$$

or, solving for $T'_{j,k}$

$$T'_{j,k} = T_{j,k} + \left(\frac{\alpha \cdot \Delta t}{\Delta x^2} \right) \cdot [T_{j+1,k} + T_{j-1,k} - 2T_{j,k}] \quad (3.51)$$

letting $F_0 = \left(\frac{\alpha \cdot \Delta t}{\Delta x^2} \right)$ and, rearranging yields,

$$T'_{j,k} = T_{j,k} + F_0 [T_{j+1,k} + T_{j-1,k}] - 2F_0 T_{j,k} \quad (3.52)$$

or

$$T'_{j,k} = F_0 [T_{j+1,k} + T_{j-1,k}] + (1 - 2F_0) T_{j,k} \quad (3.53)$$

where $T'_{j,k}$ = sheet element temperature at a later time t . The discretized equation above will enable the computation of temperatures for nodes 2 through $(N-1)$ within the sheet. The

nodes at the sheet surfaces (node 1 and node N) are governed by the stated boundary conditions that will be calculated using the following finite difference equations:

$$T'_{0,jk} = T_{0,jk} + 2F_0 [T_{1,jk} - T_{0,jk}] + 2F_0 [T_{a,0} - Bi_0 T_{0,jk}] + 2F_0 Rad_{0,jk} F_g \quad (3.54)$$

with

$$F_0 = \frac{\alpha \cdot \Delta t}{\Delta x^2}, \quad Bi = \frac{h \cdot \Delta x}{k}, \quad \text{and} \quad Rad = \frac{\Delta x}{k} F_{h-s} \sigma (T_H^4 - T_0^4) \quad (3.55)$$

3.3.2 Software Package Utilized

The finite difference previously described form the basis for an existing code, which to some degree was developed for zone-heating thermoforming processes. The code, called "TF505", is a Qbasic program produced by Sherwood Technologies in Ohio, USA. This commercial software package was used to expedite the current research process by circumventing some programming. "TF505" simulates the energy exchange between N x M heater elements and the same number of sheet elements. This program solves the finite difference equations explicitly with some simplifications in the combined view factor and gray body effects. The lumped-capacitance model is used in "TF505". This approximation is valid since the Biot number for the chosen parameters is less than 0.1, as illustrated in the following calculations:

$$Bi = \frac{h \cdot t}{k} = \frac{1 \cdot \left(\frac{0.06}{12}\right)}{0.125} \quad (3.56)$$

$$Bi = 0.04, \quad (\text{which is } < 0.1) \quad (3.57)$$

where h = air heat transfer coefficient	= 1.000	$\frac{\text{Btu}}{\text{ft}^2 \cdot \text{hr} \cdot ^\circ\text{F}}$
t = sheet thickness (Polypropylene)	= 0.060	inches
k = thermal conductivity (Polypropylene)	= 0.125	$\frac{\text{Btu}}{\text{ft} \cdot \text{hr} \cdot ^\circ\text{F}}$

When the average temperature of the entire sheet becomes greater than the normal forming temperature of a selected polymer, like PP, the program terminates and produces a temperature array of sheet elements. For purposes of comparison with experimental images, "TF505" was utilized and programmed to terminate after 60 seconds, and 120 seconds of heating time, respectively. The program output includes a matrix of surface and center sheet temperatures. The output displays the temperatures of a sufficient quadrant of an entire sheet. The following lists some input parameters for "TF505":

1. Sheet dimensions (thickness, width, length)
2. Initial temperatures (sheet, heater, air)
3. Emissivity (sheet and heater)
4. Sheet-to-heater spacing
5. Heat transfer coefficients for warm air
6. Choice of 34 polymers from material properties database.

One of the constraints of this program is the limited number of elemental divisions permitted in the y-direction (length-wise). For the present calculations an 8 x 12 element

array was selected. Basically, the sum of radiation exchange from every heater element is imposed onto one sheet element, and a loop repeated the whole process through the entire sheet of 96 elements. The internal sheet temperature is calculated through 9 thickness-elements specified within "TF505" (excluding the two surface nodes).

In an attempt to theoretically model the range of sheet temperature distributions obtainable with zone heater based thermoforming equipment, a number of simulations were performed and compared with corresponding experimental results. The findings when this was done are presented and discussed in Chapter 5. Prior to focusing on the very important comparisons, however, it is critical that one understands the experimental temperature sensing methods utilized. This is the subject of Chapter 4, which follows.

CHAPTER 4

EXPERIMENTAL TEMPERATURE SENSING APPROACH

The present investigation was configured to include the development of an experimental capability to monitor polymer sheet temperature distributions in real-time during thermoforming processes. Such a capability would serve the dual role of enabling both numerical model evaluation and real-time intelligent process control during manufacturing. While a number of temperature sensing approaches were considered, the one that was chosen for development and implementation was based on infrared imaging technology. Details related to this technology and the thermal imaging system that was developed as part of the current work are provided throughout the remainder of this chapter.

4.1 Introduction to IR Imaging Technology

Infrared thermal imaging technology studies began in the demanding world of military research and development during the 60s. By 1988, the first commercial IR camera was introduced in industry. Raytheon has been the forerunner of IR technology, especially since the consolidation of Texas Instruments and Hughes Aircraft Corporation as a part of Raytheon's Sensors & Electronics division in 1998. The IR camera employed during the current study in this thesis was Raytheon's "PalmIR 250", one of

today's more affordable high-resolution hand-held thermal imagers.

The IR camera consists of a lens, detector, and signal processor. IR imagers detect emitted infrared energy from objects and produce proportional electrical signals that are displayed as a "thermal signature". All matter possessing a temperature emits infrared radiation in the amount defined by the Stefan-Boltzmann radiation law, $E = \sigma T^4$ [38].

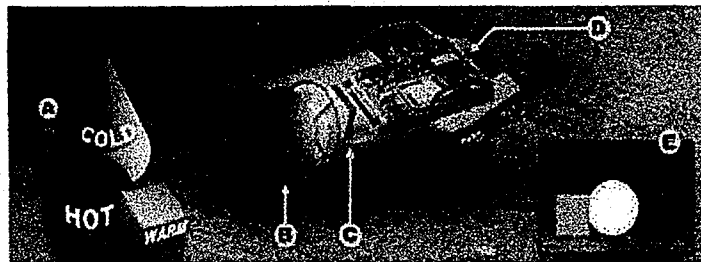


Figure 4. 1: As shown in the diagram above, infrared energy from objects in the scene (A) is focused by optics (B) onto an infrared detector (C). The information from the infrared detector is passed to sensor electronics (D) for image processing. The signal processing circuitry translates the infrared detector data into an image that can be viewed on a standard video monitor (E). (From Raytheon at <http://www.raytheoninfrared.com/technologies/tec2.htm>)

Figure 4.1 simply illustrates the principles of IR thermal imaging from emitted energy detection to video display.

The IR camera can "see" in the dark as visible light is inconsequential to its thermal detection. Figure 4.2 illustrates the advantage of IR imaging in providing the thermal information unseen through visible light. This technology has also been proven as a successful narrative device for heightened-suspense in the film chronicles of "Hannibal Lecter" and "The Predator". The advantage of IR imaging in comparison to IR spot pyrometry

today's more affordable high-resolution hand-held thermal imagers.

The IR camera consists of a lens, detector, and signal processor. IR imagers detect emitted infrared energy from objects and produce proportional electrical signals that are displayed as a "thermal signature". All matter possessing a temperature emits infrared radiation in the amount defined by the Stefan-Boltzmann radiation law, $E = \sigma T^4$ [38].

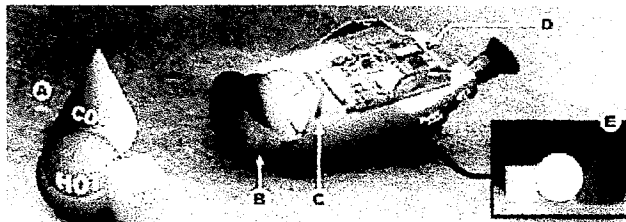


Figure 4. 1: As shown in the diagram above, infrared energy from objects in the scene (A) is focused by optics (B) onto an infrared detector (C). The information from the infrared detector is passed to sensor electronics (D) for image processing. The signal processing circuitry translates the infrared detector data into an image that can be viewed on a standard video monitor (E). (From Raytheon at <http://www.raytheoninfrared.com/technologies/tec2.htm>)

Figure 4.1 simply illustrates the principles of IR thermal imaging from emitted energy detection to video display.

The IR camera can "see" in the dark as visible light is inconsequential to its thermal detection. Figure 4.2 illustrates the advantage of IR imaging in providing the thermal information unseen through visible light. This technology has also been proven as a successful narrative device for heightened-suspense in the film chronicles of "Hannibal Lecter" and "The Predator". The advantage of IR imaging in comparison to IR spot pyrometry

lies in its thermal mapping capability that provides a wealth of temperature information on the surface area of a target object.



Figure 4. 2: Example of visible light versus infrared imaging. The left image is what you may see in ordinary light on a dark night. The image at right is the same scene but as seen with an Infrared camera. (<http://www.raytheoninfrared.com/technologies/tecl.htm>)

4.2 Thermal Imaging System and Temperature Calibration

The IR camera detection is a linear response to the incoming thermal energy (E). Since this energy is not linearly related to temperature, in all but very small ranges, IR detectors do not respond linearly with temperature (T). Therefore, the gray scale (GS) intensity response, encompassing 256 values, of the IR imager is proportional to thermal energy, or " $GS \propto E$ ". The energy versus gray scale relationship in Figure 4.3 is a valid assumption.

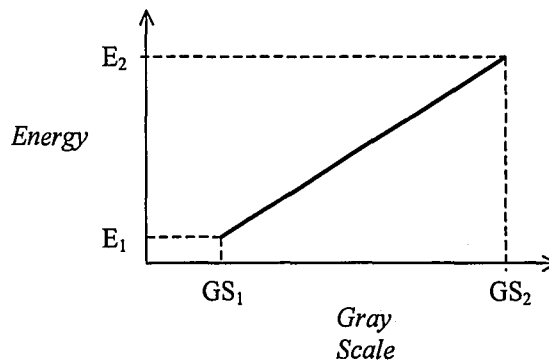


Figure 4. 3: Linear relationship between incoming thermal energy and gray scale value.

lies in its thermal mapping capability that provides a wealth of temperature information on the surface area of a target object.

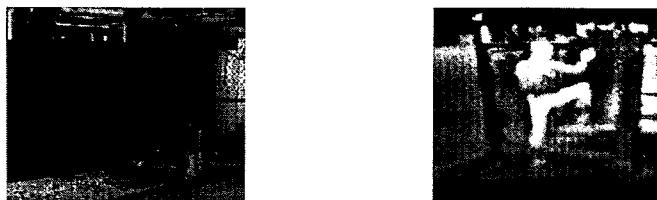


Figure 4. 2: Example of visible light versus infrared imaging. The left image is what you may see in ordinary light on a dark night. The image at right is the same scene but as seen with an Infrared camera. (<http://www.raytheoninfrared.com/technologies/tec1.htm>)

4.2 Thermal Imaging System and Temperature Calibration

The IR camera detection is a linear response to the incoming thermal energy (E). Since this energy is not linearly related to temperature, in all but very small ranges, IR detectors do not respond linearly with temperature (T). Therefore, the gray scale (GS) intensity response, encompassing 256 values, of the IR imager is proportional to thermal energy, or " $GS \propto E$ ". The energy versus gray scale relationship in Figure 4.3 is a valid assumption.

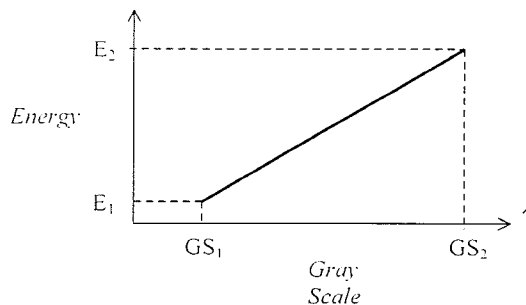


Figure 4. 3: Linear relationship between incoming thermal energy and gray scale value.

The PalmIR 250 imager does not require calibration as far as detected energy to gray scale image is concerned. However, the calibration of its gray scale response into temperature values is accomplished with a digital data processing software developed at Engineered Data Systems in Michigan. To accomplish this calibration, two blackbody objects with known temperatures (via surface thermocouples) and optical properties (ϵ , ρ , and τ) need to be placed within the camera's field-of-view. One point is selected from each object, and these two points represent the range of detection. Again, the linear interpolation between the two known calibration points is one of energy. Upon conversion of these energy values, through the Stefan-Boltzmann relation, a temperature range of detection is successfully calibrated.

The energy and gray scale variables can be written in the familiar form of a linear "y = m·x + b" equation, as illustrated in equation (4.1) below:

$$E = m \cdot (GS) + b \quad (4.1)$$

When two calibration points are chosen, the above Equation will produce two simultaneous relations, as shown in equations (4.2a) and (4.2b), that can be solved for values of "m" and "b".

$$E_1 = \epsilon_1 \sigma (T_1 + 273)^4 = m \cdot (GS)_1 + b \quad (4.2a)$$

and,

$$E_2 = \epsilon_2 \sigma (T_2 + 273)^4 = m \cdot (GS)_2 + b \quad (4.2b)$$

Substituting "m" and "b" into equation (4.1) will produce an equation for E versus GS that can then be used for the forthcoming temperature conversions. For the Polypropylene (PP) target material utilized during the present study, a gray body, the energy detected by the IR camera eye is a result of emission from the polymer, foreground reflection off the polymer, and background transmission through the polymer, as illustrated in Figure 4.4. Using the known material values of emissivity (ϵ), reflectivity (ρ), and transmissivity (τ), along with the ascertained foreground (T_f) and background (T_b) temperature compensations, equation 4.3 will produce the target temperature (T_t).

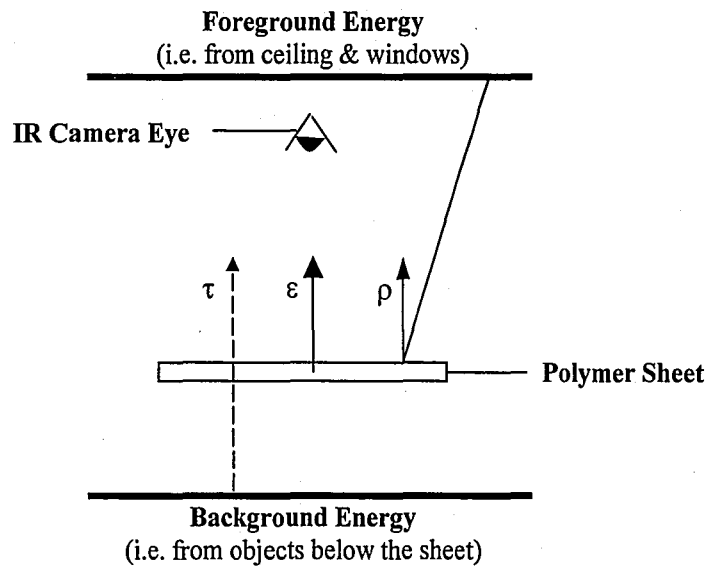


Figure 4. 4: The influence of emissivity(ϵ), reflectivity(ρ) and transmissivity(τ) on the detected energy.

For the present calculations emissivity can be assumed identical to absorptivity. Equation (4.3) can be rearranged to solve for T_t .

$$m \cdot (GS)_t + b = \epsilon_t \sigma (T_t + 273)^4 + \rho_t \sigma (T_f + 273)^4 + \tau_t \sigma (T_b + 273)^4 \quad (4.3)$$

4.3 IR Experimental Set-up

The IR thermal imager was obtained and mounted above the forming area of the thermoforming machine, viewing the clamped polymer sheet. Black foam boards were placed behind the IR camera and below the clamped sheet to maintain the Foreground and Background compensation at room temperature (75 to 85°F). The video output from the camera was fed to a framegrabber in an associated personal computer that ran the commercial "IR-Comp" and "Autocapture" data processing software. The lens focus and aperture (which acts as an optical gain) were adjusted manually. Additionally, the "Gain" and "Level" settings on the camera were adjusted until a proper real-time video display was obtained. Figure 4.5 illustrates the arrangement and dimensions of the experimental set-up.

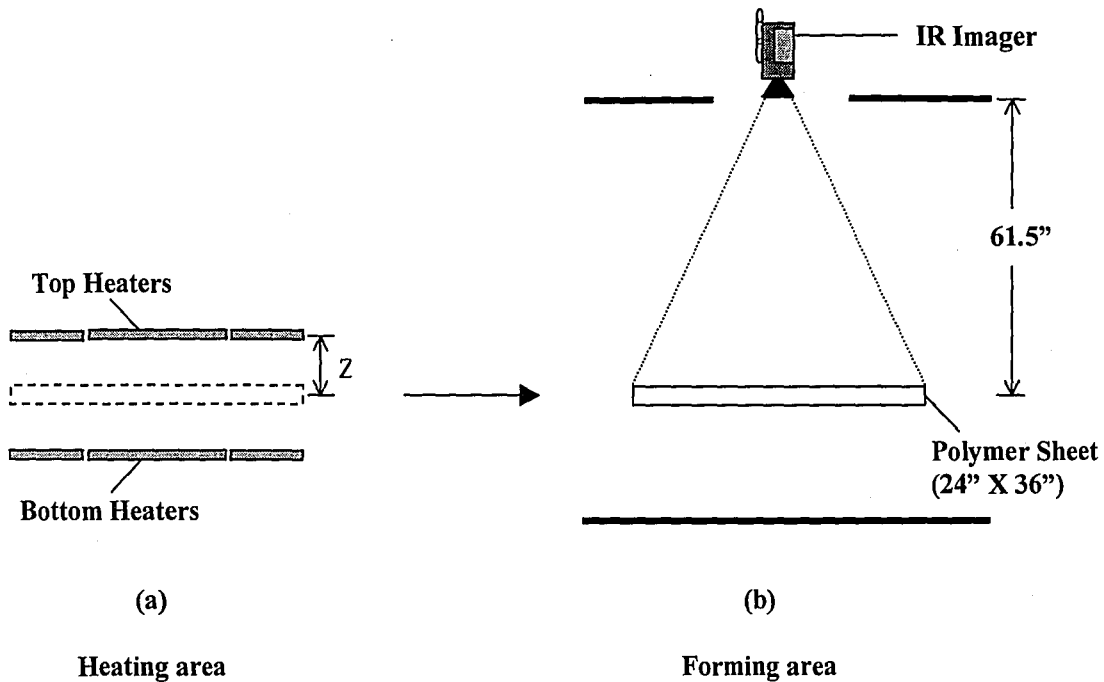


Figure 4. 5: During heating (a), the top and bottom zone heaters are positioned a distance $Z = 8''$ or $Z = 12'' (\pm 1'')$ from the polymer sheet. With a 25mm lens, the IR imager is placed 61.5'' above the target polymer sheet, in the forming area (b) to obtain a view that encompasses the sheet and reference black bodies.

In the experimentation, the distance "Z" between the sheet and top heater was one inch less than the nominal value, whereas the bottom heater is one inch further away. For instance, when "Z=12", the top heater-to-sheet distance was actually 11 inches while the bottom separation was 13 inches. The reasoning behind this is to specifically compensate for sheet sag which brings the top and bottom separation levels closer to each other and the nominal "Z=12" or "Z=8" distance.

Figure 4.6 shows a typical scene of the forming area with two reference black bodies. In this gray scale image, a higher saturation of white represents higher temperatures while black denotes lower temperatures. The bright white spot on the top

right of the image is the thermal signature of a 60 watt bulb used as the high temperature threshold. On the other hand, the less intense spot below is the lower temperature boundary. Note that the forming area at room temperature is cooler than the "Cool reference" in Figure 4.6.

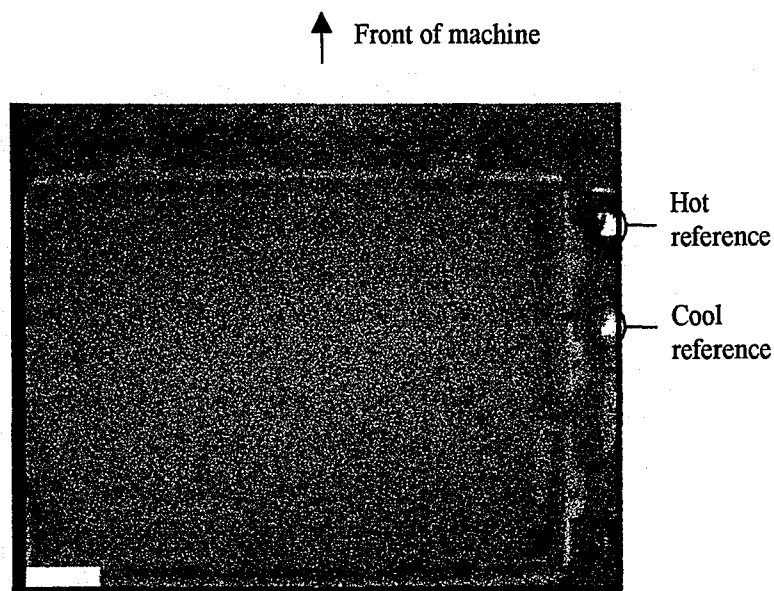


Figure 4. 6: An IR image of the forming area, including the clamps and two black body reference "points" for temperature calibration.

The "Hot" and "Cool" references define the temperature calibration range. During the study, the two references were adjusted to encompass the predicted maximum and minimum sheet surface temperatures. The "Hot reference" was adjusted between 187.5 °F and 335 °F, whereas the "Cool reference" ranged from 89 °F to 121.5 °F. Thus even the "Cool reference" was hotter than room temperature. This explains why the un-heated polymer sheet in Figure 4.6 is darker than both the hot and cool reference

bodies. Contact thermocouples were used to record the actual hot and cool reference temperature values as well as the experimental room temperature.

The temperature conversion from gray scale values (GS) to Fahrenheit ($^{\circ}\text{F}$) was made through the "Autocapture" program. The following parameters are required for the software's calibration worksheet prior to obtaining the digitized data:

- Hot Reference Temperature
- Cool Reference Temperature
- Emissivity of Reference Black Bodies ($\epsilon_B=1$)
- Background & Foreground Temperature
- Emissivity(ϵ), Reflectivity(ρ), and Transmissivity(τ)

For the 60 mil PP homopolymer material, the following values were used:

$$\epsilon = 0.28, \quad \rho = 0.20, \quad \text{and} \quad \tau = 0.52 \quad (4.4)$$

The temperature calibration procedure was made with respect to thermocouple measurements. First, a K-type surface thermocouple was used to obtain the temperature of a specific area near the center of the sheet. These temperatures were taken when the heated polymer sheets reached the forming area, immediately after an IR image was taken. Such measurements were made during the various heater settings and the values of ϵ , ρ , and τ were adjusted until the Autocapture software provided a good comparison with the thermocouple readings of the specific area. After several trials, the above stated values of ϵ , ρ , and τ

enabled the IR imaging system to give reasonable accuracy for the surface sheet temperature of 60 mil polypropylene homopolymer.

As polypropylene is a semi-crystalline polymer, its opacity turns transparent at softening temperatures around 300 °F. Some studies have been made regarding the temperature dependence of the optical properties of polymers[39, 40]. However, this collection of experimental polymer data extends to films of thicknesses below 20 mil. Ideally, our IR imaging system would be independent of a thermocouple temperature reference if accurate optical properties of our target semi-transparent material is readily available. However, a compromise was made, by using a contact thermometer as reference, due to the constraint of time. This predicament will be further discussed in Chapter 6.

4.4 Radiant Heater Settings

The thermoforming machine utilized during the present investigation was a ZMD V-200 series zone-heating thermoformer[41]. This machine is equipped with 24 separately controllable heaters, as shown in Figure 4.7. During the investigation, eight different zone heating patterns were chosen for the experimentation using the 24 individually controlled heaters. Figure 4.8 illustrates the eight patterns selected. In selecting these patterns, an attempt was made to study the full range of possibilities achievable with the target thermoforming machine.

1		2		3	
4	5	6	7	8	9
10		11		12	

(a)

13		14		15	
16	17	18	19	20	21
22		23		24	

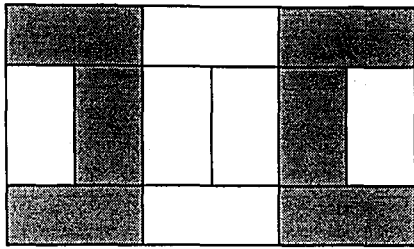
(b)

Figure 4. 7: Individually Controlled Heaters for Top (a) and Bottom (b), numbered from 1 to 24.

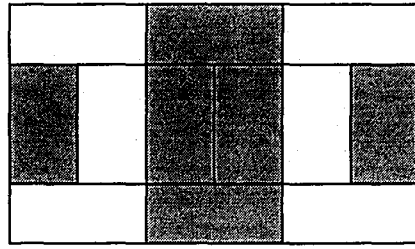
In addition, two heating times (60 and 120 seconds) and two sheet-to-heater distances (8 and 12 inches) were studied. Hence, a total experimental design of 32 different trials with heated polypropylene sheets was performed.

The heaters were set at one of two different power levels: 61%, or 8%. At steady-state (after a 15 minute warm-up period) heater temperatures under these conditions reached 640 °F and 200 °F respectively. The higher temperature was chosen with regard to the default heater settings in "TF505", the computation software. Moreover, 200 °F was selected instead of room temperature (0% power) in order to expedite the intervals between experiments. Radiant heaters possess a low rate of cooling.

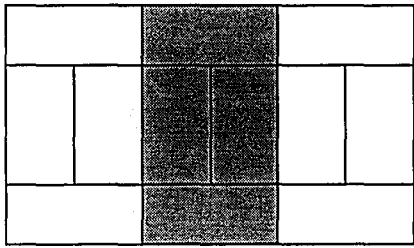
The results obtained during the study and comparisons between theory and experimentation are provided in the next chapter.



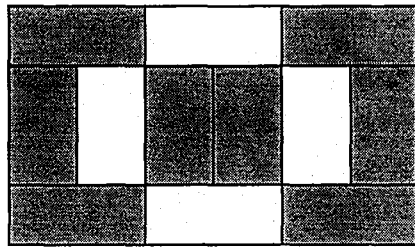
(i)



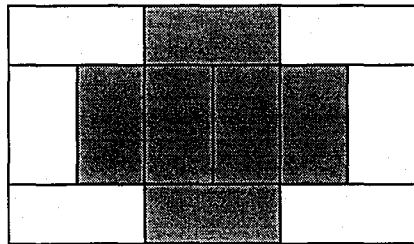
(ii)



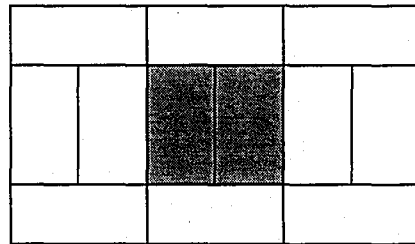
(iii)



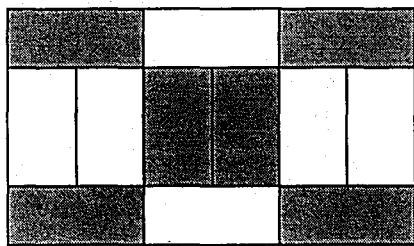
(iv)



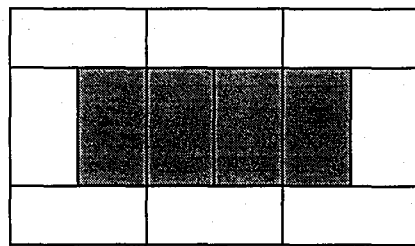
(v)



(vi)



(vii)



(viii)

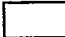

 = 640 °F
 = 200 °F

Figure 4. 8: The Heat Patterns, (i) to (viii), Chosen for the Present Investigation.

CHAPTER 5

THEORETICAL AND EXPERIMENTAL RESULTS

Temperature distributions resulting from numerical simulations and experimental infrared thermal imaging for the prescribed heat pattern settings are presented and compared in this chapter. The objective was to study the advantages and limitations of zone-heating in regard to inducing desired polymer sheet heat patterns prior to thermoforming. Such knowledge would be useful when applied in conjunction with predictions of required polymer sheet temperature patterns that would yield desired amounts of localized deformation during forming and the intended final thickness distributions. Thus, one of the primary objectives of the study was to create a validated set of guidelines for physically possible sheet temperature distributions.

5.1 Individually Controlled Radiant Zone-Heating Patterns

As mentioned previously, during the investigation eight different zone heating patterns were chosen for study using the 24 individually controlled heaters shown in Figure 5.1. Prior to initiating the numerical and experimental endeavours, thirty two different sheet heating situations were selected. These cases consisted of the eight heat patterns, identical for both top and bottom heaters of the thermoformer, at two heating times (t) and two different sheet-to-heater distances (Z).

1		2		3	
4	5	6	7	8	9
10		11		12	

(a)

13		14		15	
16	17	18	19	20	21
22		23		24	

(b)

Figure 5. 1: Individually Controlled Heaters for Top (a) and Bottom (b), Numbered from 1 to 24.

The heaters were set to one of the eight patterns illustrated in Figure 5.2. To generate the heater temperature shown, the heaters were actually set at two different power levels: 61% or 8% (out of 100%). At steady-state, with these settings (after a 15 minute warm-up period) the heater temperatures reached the 640 °F and 200 °F levels respectively. Heater "24" was characterized empirically using a Raytek Raynger ST pyrometer gun. A logarithmic plot of heater temperature vs. % heater power, shown in Figure 5.3, was used as a general guideline for setting the individual heaters to their desired temperatures.

During the study, the higher temperature was chosen to correspond to the default heater settings in "TF505", the numerical software package. On the other hand, the 200 °F lower heater temperature level was selected instead of room temperature (0% power) to expedite the intervals between experiments. As radiant heaters possess a low rate of cooling, a concern was that

it would take over an hour for the heaters to fully cool to room temperature after heating if such were desired.

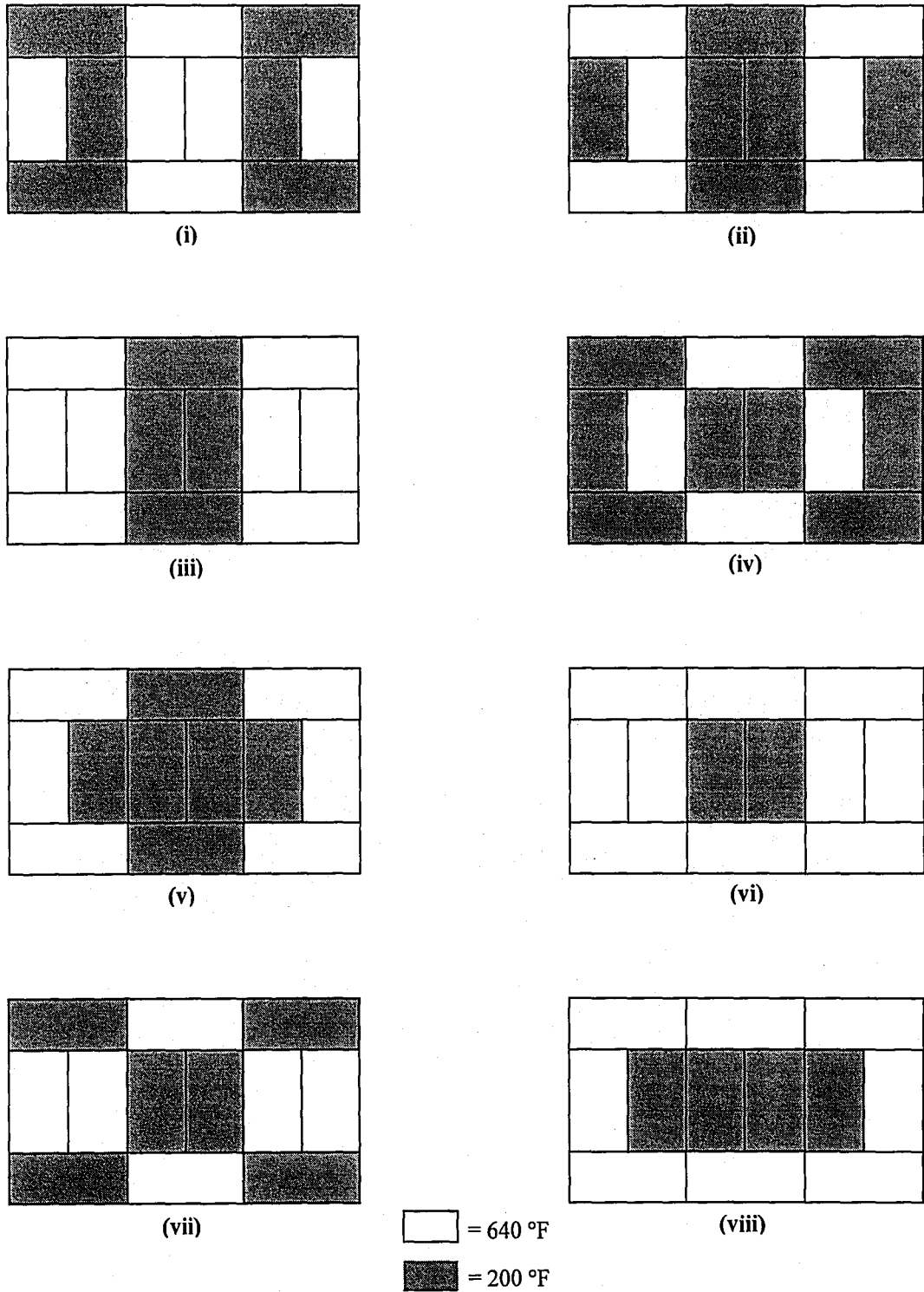


Figure 5. 2: The Heat Patterns, (i) to (viii), Chosen for the Experimental Investigation.

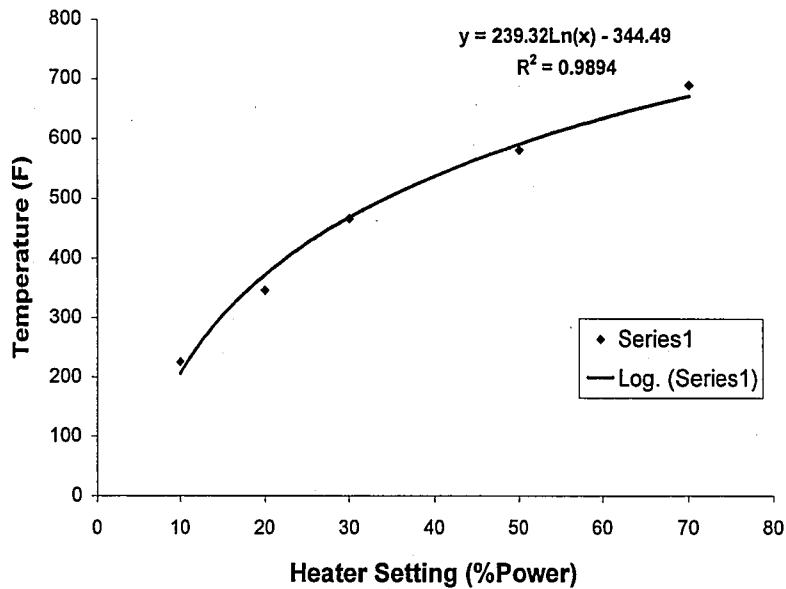


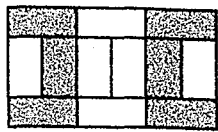
Figure 5. 3: Plot of Temperature (°F) versus Heater Setting (%) for Heater “24”.

5.2 Qualitative Comparisons between Numerical and Experimental Results

Figures 5.4 through 5.19 display resultant numerical and experimental comparisons for Heat Patterns 1 through 8. It should be noted that in the figures, gray colored heaters are at 200 °F whereas white heater blocks represent those at 640 °F. In the following analysis, the two heater temperature settings will be repeatedly referred to as the “cool” or “hot” heater settings. Furthermore, the numerical results displayed as full-sized 24 X 36 inch thermal maps were originally computed on only a quadrant of each sheet. The dimensions of the top and bottom heating areas, as seen in Figures 5.1 (a) and (b), were identical to the polymer sheet size during this study.

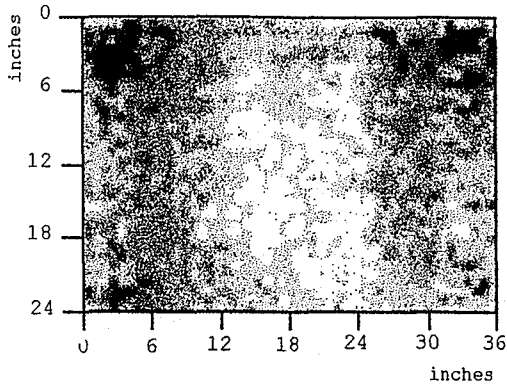
Heat Pattern 1 is mostly "hot" in the center third of the heating area. Figures 5.4 (a) and (c) show experimental results, whereas Figures 5.4 (b) and (d) display numerical results that were obtained in the fashion described in Chapter 3. In all cases, the center of the sheet was found to be noticeably warmer than the perimeter, an obvious occurrence due to "edge losses" of the view factor. This will be seen to be prevalent throughout the remaining comparisons. At 60 seconds, the IR image detected temperatures between 180 and 200 °F in the middle portion of the sheet. At 120 seconds, the IR image possessed high temperature regions commensurate with Heat Pattern 1 as seen in Figure 5.4 (c). Figures 5.4 (c) and (d) are qualitatively comparable in that the middle region of the sheet was hot (between 260-290 °F) whereas the four corners were at temperatures around 170 °F.

When the heater was closer to the sheet at Z=8 inches, as seen in Figure 5.5, the thermal maps appear less diffused. The temperature patterns induced on the polymer sheets were more defined compared to Figure 5.4 with Z=12 inches. Figures 5.5 (a) and (b) bear closer similarities to each other as the Z distance was reduced from 12 to 8 inches. Figure 5.5 (c) has very similar comparisons to Heat Pattern 1 with the distinctive "hot strip" in the center and two hot areas on the sides. On the other hand, the numerical results of Figure 5.5 (d) appeared more diffused compared to the experimental IR image of Figure 5.5 (c).



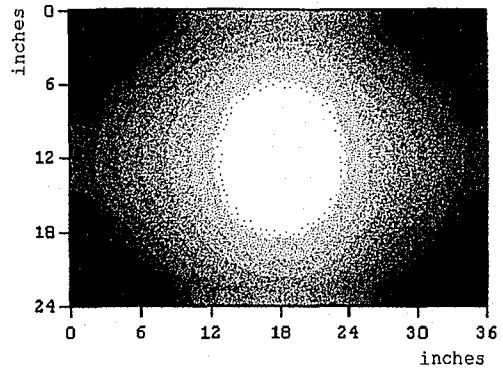
Pattern 1

Z = 12 inches

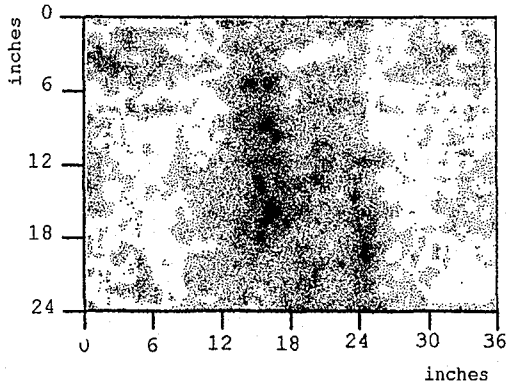


(a)

t = 60s

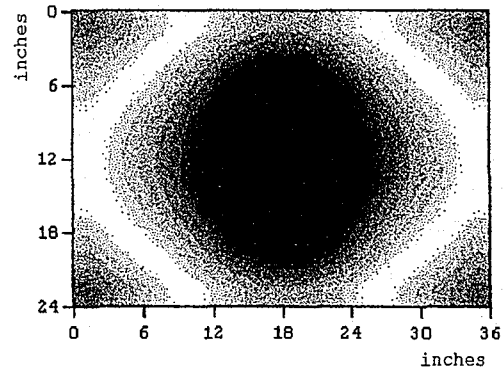


(b)



(c)

t = 120s



(d)

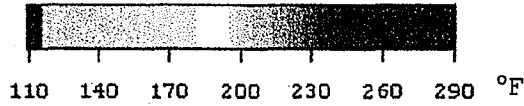
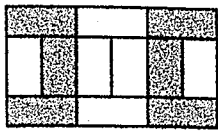
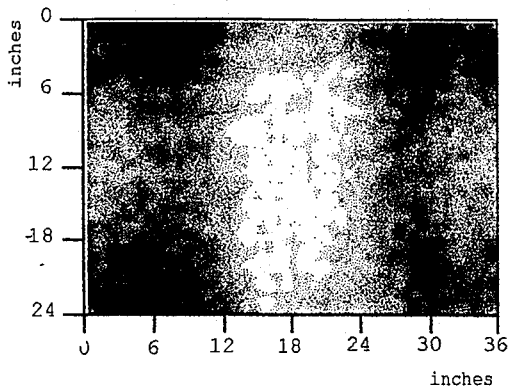


Figure 5. 4: Comparison of Theoretical and Experimental Temperature Distribution Corresponding to Heater Pattern 1 at Z = 12 inches: (a) Experimental IR Image at t=60s ; (b) Numerical Image at t=60s ; (c) Experimental IR Image at t=120s ; (d) Numerical Image at t=120s.



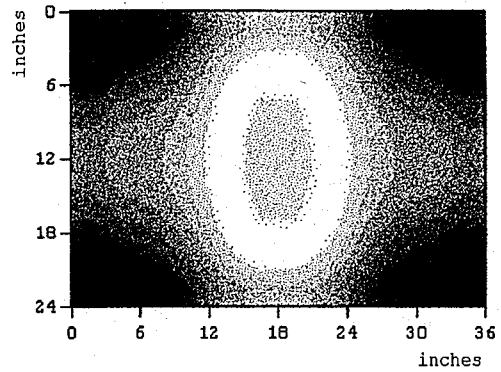
Pattern 1

Z = 8 inches

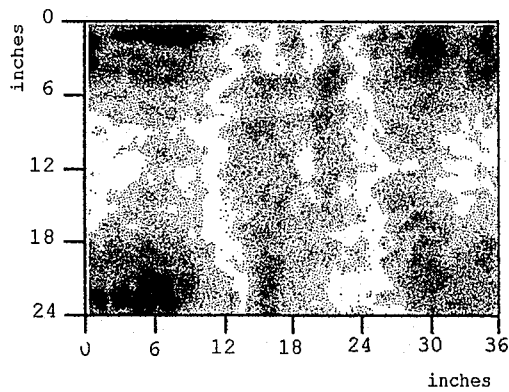


(a)

t = 60s

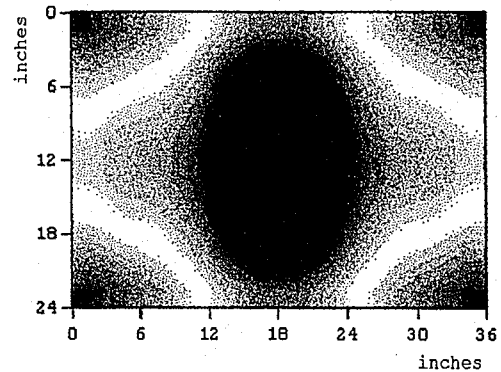


(b)



(c)

t = 120s



(d)

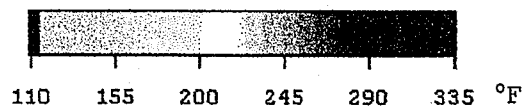
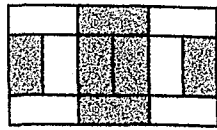


Figure 5. 5: Comparison of Theoretical and Experimental Temperature Distribution Corresponding to Heater Pattern 1 at Z = 8 inches: (a) Experimental IR Image at t=60s ; (b) Numerical Image at t=60s ; (c) Experimental IR Image at t=120s ; (d) Numerical Image at t=120s.

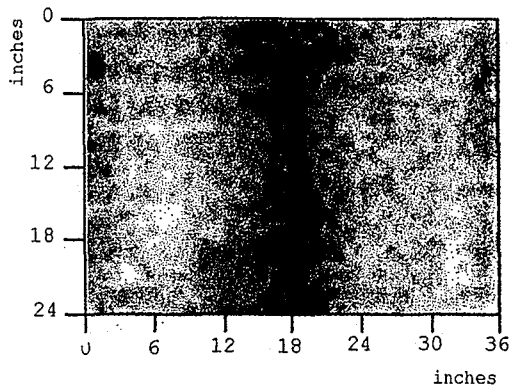
Pattern 2 is a negative image of Pattern 1 in that the "hot" and "cool" heaters from the first pattern are reversed. Figures 5.6 (a) and (b) have warmer regions below 180 °F that corresponds to the "hot" heaters at distances of Z=12 inches away. At t=120 seconds, Figure 5.6 (c) and (d) appeared to be hotter versions of their counterparts at t=60 seconds with their hottest temperatures between 210 and 420 °F.

Compared to Figure 5.6, the thermal maps in Figure 5.7 appear less diffused. Figures 5.7 (a) and (b) contain two higher temperature regions at around 200 °F. The IR image of Figure 5.7 (a) has cool spots below 120 °F which are more prevalent near the edges of the middle region. Figures 5.7 (c) and (d) have comparable temperature patterns in the shape of mirror imaged kidney beans. The hot metal clamps of the thermoformer were most likely influencing the hot edges on the left and right side of Figure 6.7 (c). Moreover, the temperature gradient increased with 180 °F found in the middle (at x=18 inches) and 210 °F (at x=12 inches) found within only 6 inches away on the sheet. Figure 6.7 (d) containing the numerical result predicted an even sharper temperature gradient between x=18 inches and x=12 inches.



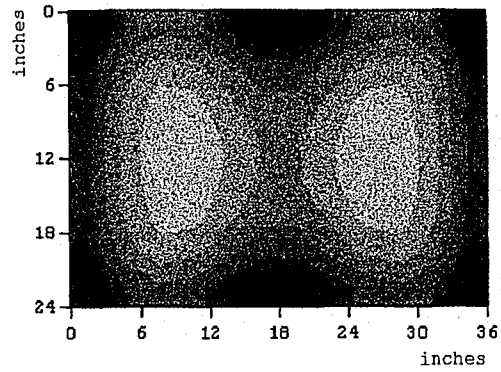
Pattern 2

Z = 12 inches

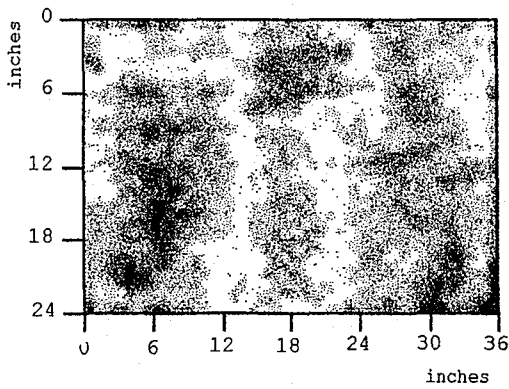


(a)

t = 60s

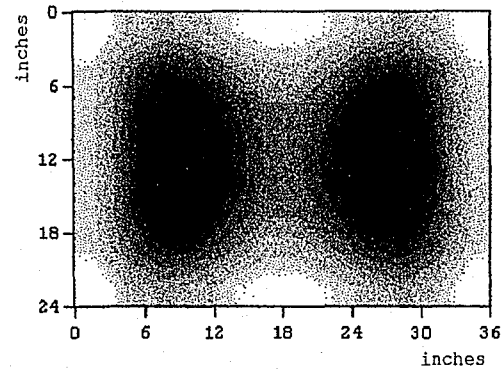


(b)



(c)

t = 120s



(d)

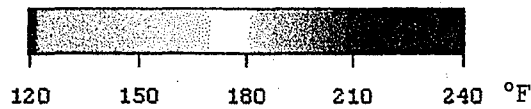
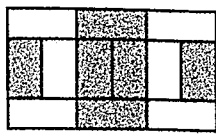
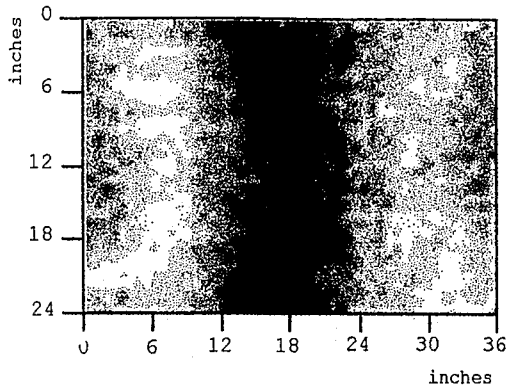


Figure 5. 6: Comparison of Theoretical and Experimental Temperature Distribution Corresponding to Heater Pattern 2 at Z = 12 inches: (a) Experimental IR Image at t=60s ; (b) Numerical Image at t=60s ; (c) Experimental IR Image at t=120s ; (d) Numerical Image at t=120s.



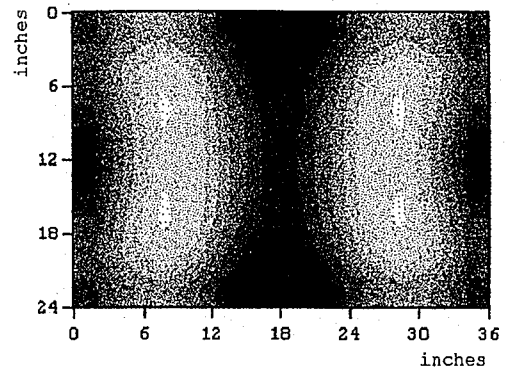
Pattern 2

Z = 8 inches

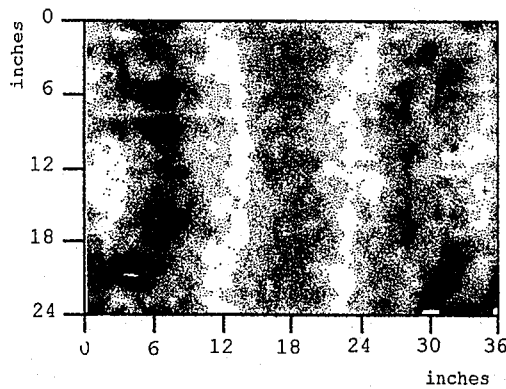


(a)

t = 60s

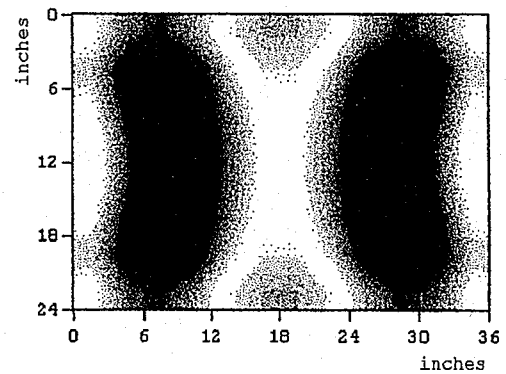


(b)



(c)

t = 120s



(d)

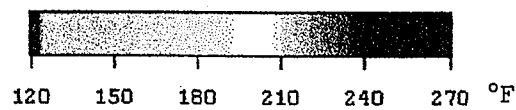
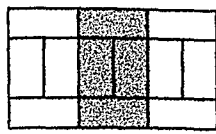


Figure 5. 7: Comparison of Theoretical and Experimental Temperature Distribution Corresponding to Heater Pattern 2 at Z = 8 inches: (a) Experimental IR Image at t=60s ; (b) Numerical Image at t=60s ; (c) Experimental IR Image at t=120s ; (d) Numerical Image at t=120s.

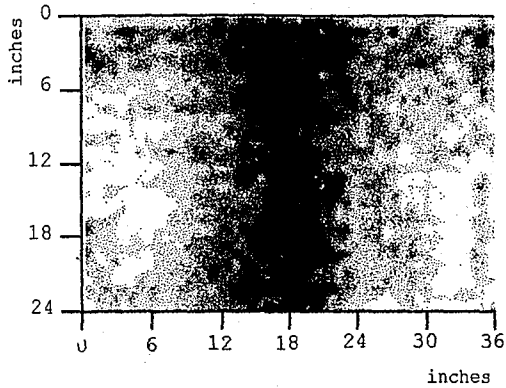
Pattern 3 consisted of a cool heater region in the middle that was sandwiched by two hot sections. Figures 5.8 (a) and (b) have comparable warm areas at around 190 °F that are centered at positions (6,12) and (30,12). On the other hand, Figures 5.8 (c) and (d) were beginning to exhibit higher temperatures in the middle section at $x=18$ inches, in addition to their hottest regions being centered around the same positions as the images obtained at $t=60$ seconds. At $t=120$ seconds, the sheet region below the cool heaters, between $x=12$ and 24 inches, were warming up to over 180 °F. This was a result of the view factor from the hot heater regions.

At $Z=8$ inches, the temperature patterns on the sheets bear a closer resemblance to Heat Pattern 3. At $t=60$ seconds, the numerical and experimental results began to exhibit warm areas at around 225 °F, as shown in Figures 5.9 (a) and (b). At $t=120$ seconds these warm areas became hotter and more well defined with hot regions over 210 °F almost strictly isolated to areas immediately under the hot heaters. Figure 5.9 (c) bears a rather remarkable similarity to Heat Pattern 3 especially since its middle section between $x=12$ and 24 inches remained mostly at around 180 °F. The numerical simulation of Figure 5.9 (d) possessed similar qualities except for a more diffusive region around the boundary separating the hot and cool heaters at $x=12$ inches.



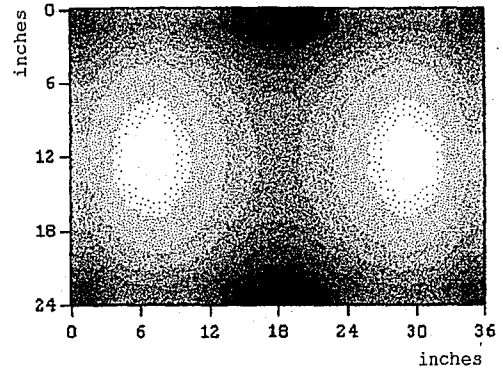
Pattern 3

Z = 12 inches

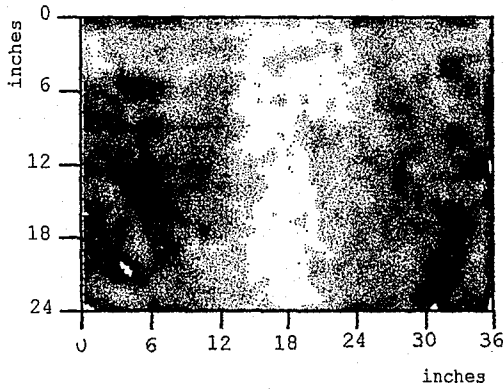


(a)

t = 60s

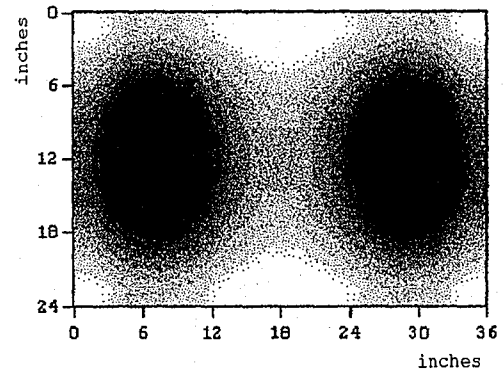


(b)



(c)

t = 120s



(d)

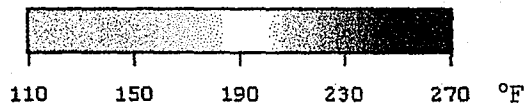
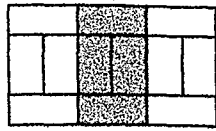
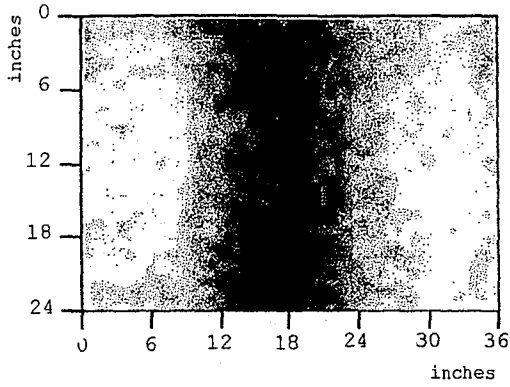


Figure 5. 8: Comparison of Theoretical and Experimental Temperature Distribution Corresponding to Heater Pattern 3 at Z = 12 inches: (a) Experimental IR Image at t=60s ; (b) Numerical Image at t=60s ; (c) Experimental IR Image at t=120s ; (d) Numerical Image at t=120s.



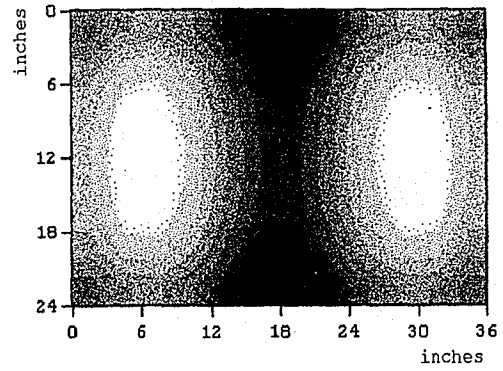
Pattern 3

Z = 8 inches

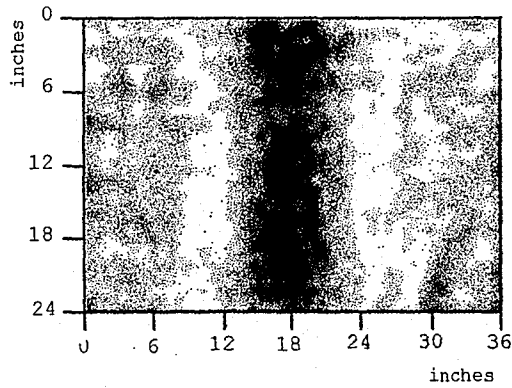


(a)

t = 60s

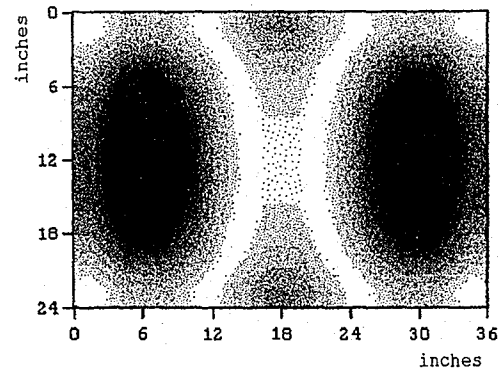


(b)



(c)

t = 120s



(d)

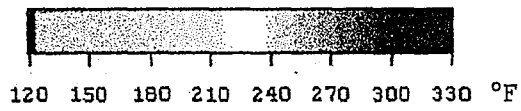
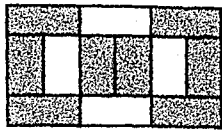


Figure 5. 9: Comparison of Theoretical and Experimental Temperature Distribution Corresponding to Heater Pattern 3 at Z = 8 inches: (a) Experimental IR Image at t=60s ; (b) Numerical Image at t=60s ; (c) Experimental IR Image at t=120s ; (d) Numerical Image at t=120s.

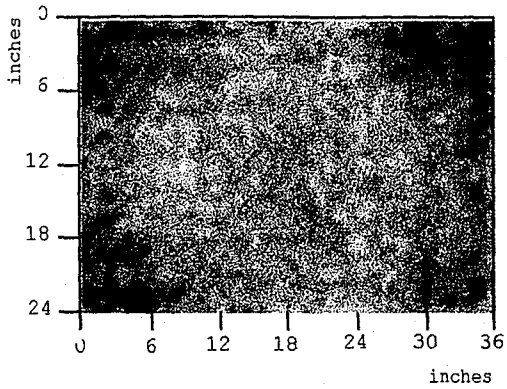
Pattern 4 involved only four hot heaters, the fewest number of 600 °F heaters in this study. Figure 5.10 (a) did not present much useful data as the sheet temperature appeared diffused. Figure 6.10 (b) displayed a faint circular region of temperatures below 150 °F. At $t=120$ seconds, the sheet temperature appeared to be higher in the middle with a maximum of 210 °F. The IR image of Figure 5.10 (c) gave a hint of a cooler spot in the middle of sheet surrounded by a diffused ring of warmer regions. On the other hand, Figure 5.10 (d) did not exhibit any detailed temperature pattern in relation to Heat Pattern 4.

At $Z=8$ inches, shown in Figure 5.11, the temperature pattern induced in the polymer sheet is apparent at both time instances. In Figure 5.11 (a) and (b), 60 seconds of heating time saw the onset of a warmer ring around 185 °F that encompassed a cooler middle region. The numerical image of Figure 5.11 (b) did not display much temperature gradient in the middle region between $x=12$ and 24 inches, whereas the experimental image of Figure 5.11 (a) exhibited a 150 to 175 °F change in the same region. The thermal maps of Figures 5.11 (c) and (d) were qualitatively comparable as the hot rings and cooler middle sections appeared distinctive. The temperature gradient between $x=12$ and 18 inches was 50 °F for the experimental image in Figure 5.11 (c), and approximately 35 °F for the numerical results in Figure 5.11 (d).



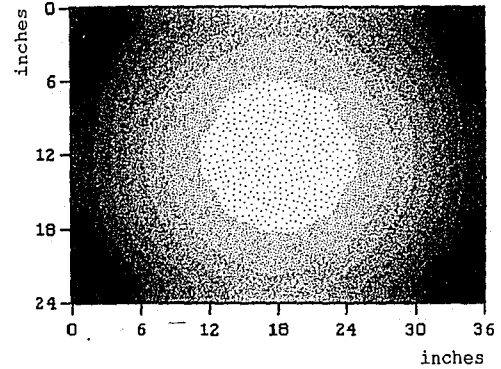
Pattern 4

Z=12 inches

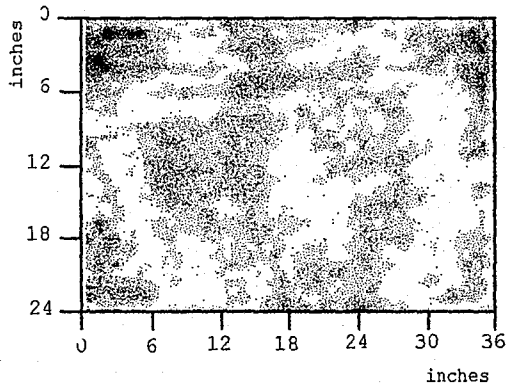


(a)

t = 60s

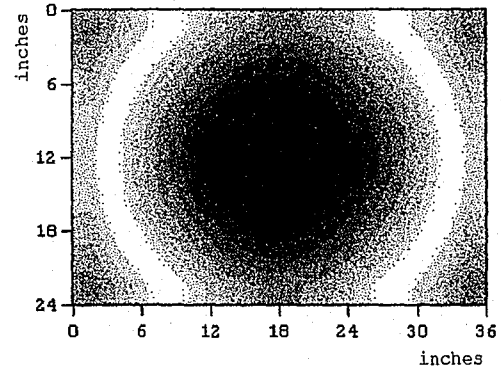


(b)



(c)

t = 120s



(d)

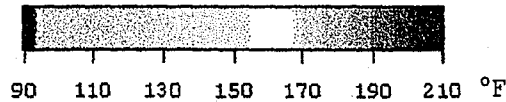
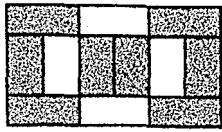
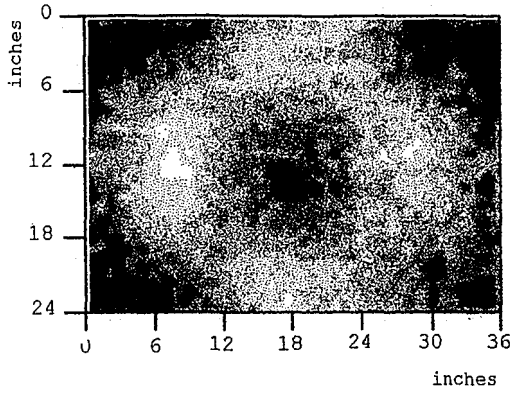


Figure 5. 10: Comparison of Theoretical and Experimental Temperature Distribution Corresponding to Heater Pattern 4 at Z = 12 inches: (a) Experimental IR Image at t=60s ; (b) Numerical Image at t=60s ; (c) Experimental IR Image at t=120s ; (d) Numerical Image at t=120s.

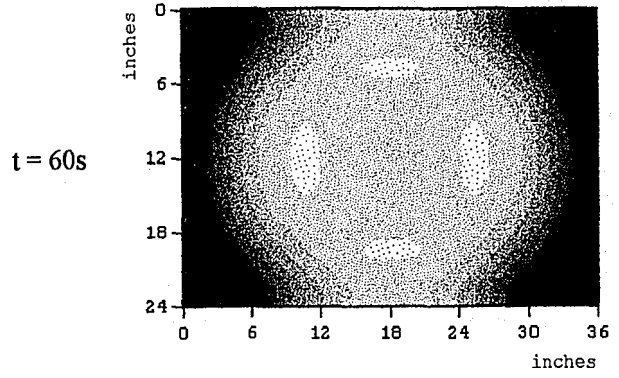


Pattern 4

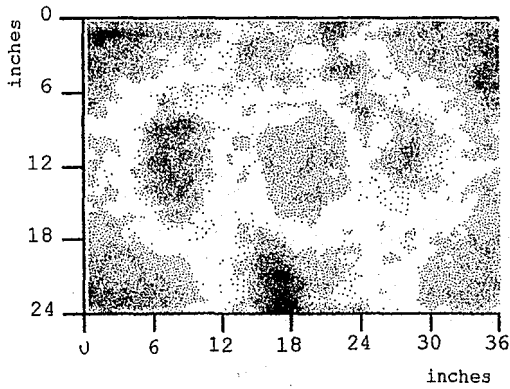
Z = 8 inches



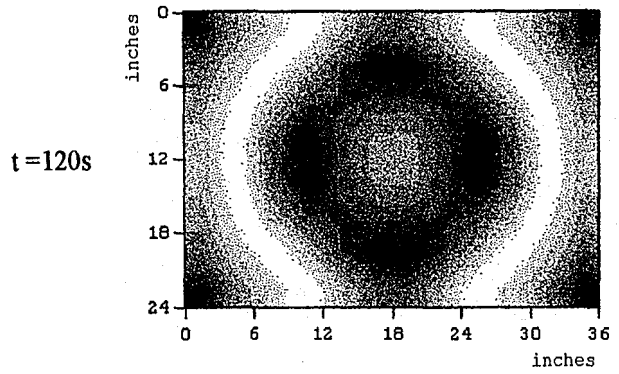
(a)



(b)



(c)



(d)

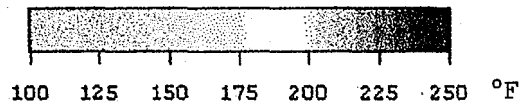
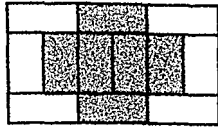


Figure 5. 11: Comparison of Theoretical and Experimental Temperature Distribution Corresponding to Heater Pattern 4 at Z = 8 inches: (a) Experimental IR Image at t=60s ; (b) Numerical Image at t=60s ; (c) Experimental IR Image at t=120s ; (d) Numerical Image at t=120s.

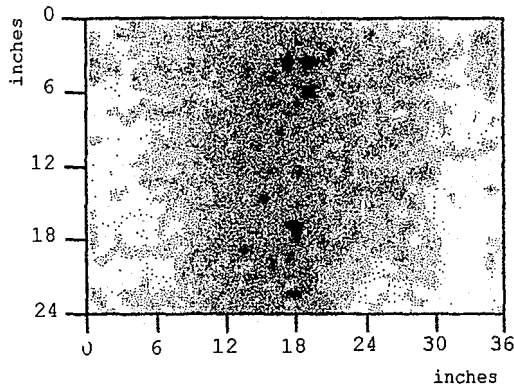
Pattern 5 was composed of three hot heaters on both sides, with six cool heaters in the middle, forming a cross. The results for $Z=12$ inches appeared more diffused. After $t=60$ seconds, the thermal maps of Figures 5.12 (a) and (b) illustrated an increase from laboratory room temperature at $80\text{ }^{\circ}\text{F}$ to around $155\text{ }^{\circ}\text{F}$ in the side regions to the left of $x=6$ inches and to the right of $x=30$ inches. At $t=120$ seconds, as seen in Figures 5.12 (c) and (d), hot regions above $170\text{ }^{\circ}\text{F}$ have dominated the polymer sheet. In Figure 5.12, the areas of highest temperature for the numerical results are located around $x=5$ inches and $x=31$ inches. For the experimental images, the occurrence of hot areas at $x=0$ inches and $x=36$ inches came from the heated metal clamps.

The results for Heat Pattern 8 at $Z=8$ inches, in Figure 5.13, showed the increased definition of temperature patterns with the decrease in sheet to heater distances or Z . Figures 5.13 (a) and (b) did not compare as well as these seen in the previous analyses. The experimental image of Figure 5.13 (a) appeared hotter at the sides with temperatures around $210\text{ }^{\circ}\text{F}$ as opposed to its cooler counterpart, in Figure 5.13 (b), that possessed high temperatures around $190\text{ }^{\circ}\text{F}$. However, after $t=120\text{s}$ the experimental and numerical results became very similar, in terms of temperature range and pattern. The hot areas between 210 and $270\text{ }^{\circ}\text{F}$ were emulating the shape of the hot heaters except the regions around $(6,12)$ and $(30,12)$ directly below two cool heaters.



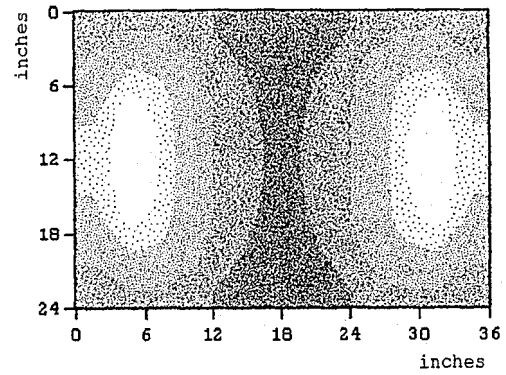
Pattern 5

Z = 12, inches

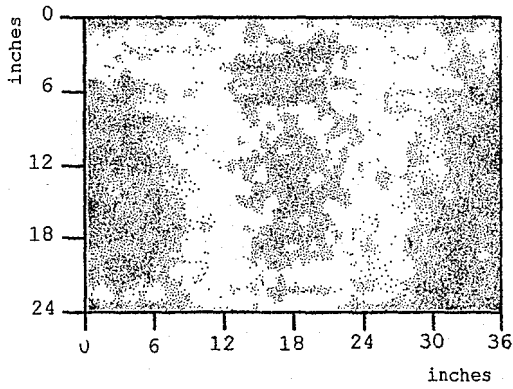


(a)

t = 60s

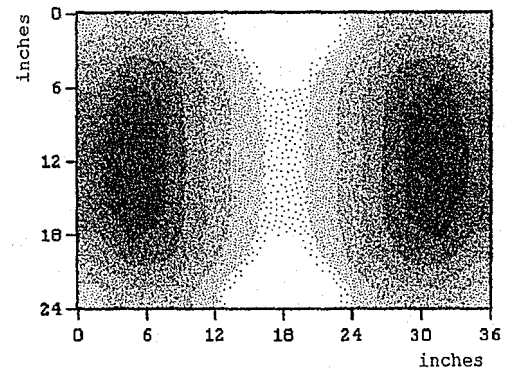


(b)



(c)

t = 120s



(d)

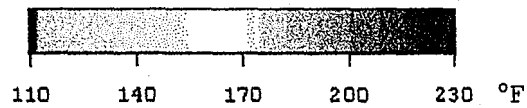
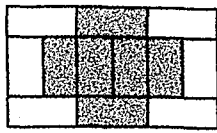
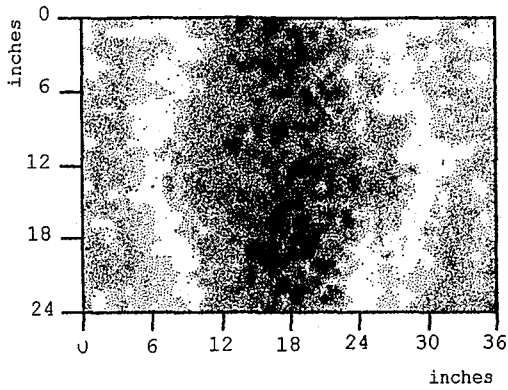


Figure 5. 12: Comparison of Theoretical and Experimental Temperature Distribution Corresponding to Heater Pattern 5 at Z = 12 inches: (a) Experimental IR Image at t=60s ; (b) Numerical Image at t=60s ; (c) Experimental IR Image at t=120s ; (d) Numerical Image at t=120s.



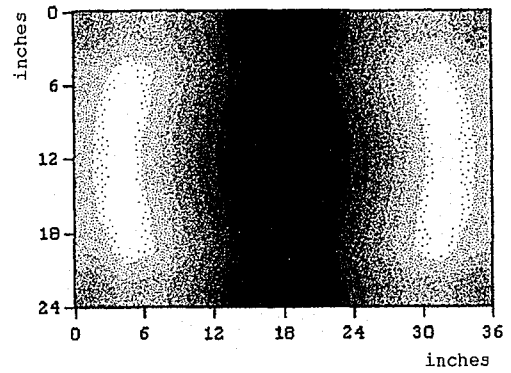
Pattern 5

Z = 8 inches

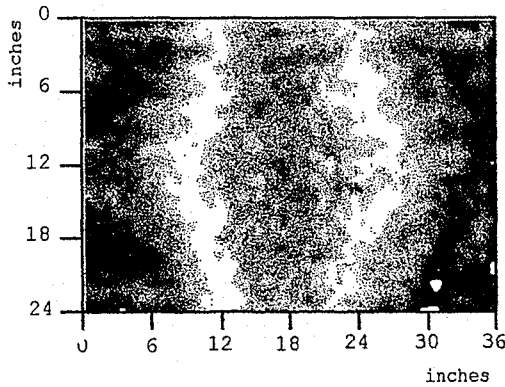


(a)

t = 60s

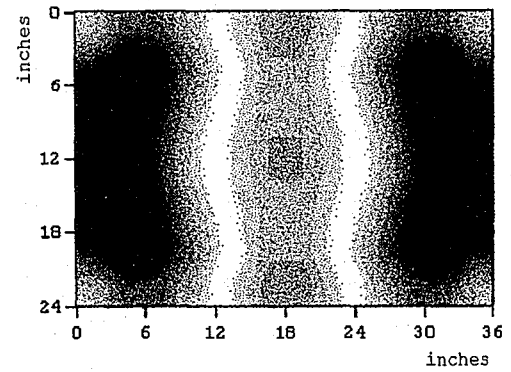


(b)



(c)

t = 120s



(d)

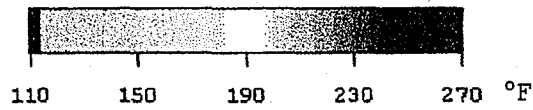
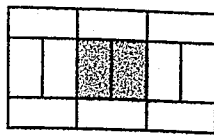


Figure 5. 13: Comparison of Theoretical and Experimental Temperature Distribution Corresponding to Heater Pattern 5 at Z = 8 inches: (a) Experimental IR Image at t=60s ; (b) Numerical Image at t=60s ; (c) Experimental IR Image at t=120s ; (d) Numerical Image at t=120s.

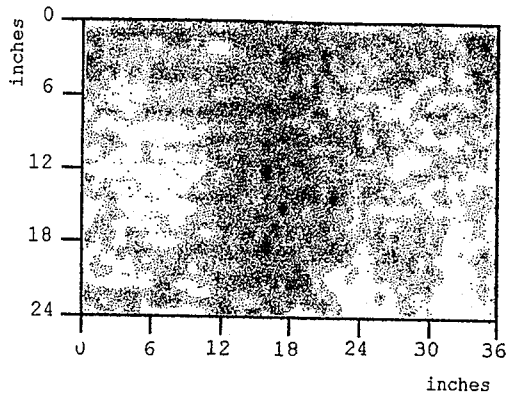
Hot elements surrounding two cool heaters in the middle formed Heat Pattern 6. Not unlike the results from Pattern 5, the thermal maps at $t=60$ seconds, as seen in Figures 5.14 (a) and (b), the middle portion of the sheet remained at a lower temperature, below $200\text{ }^{\circ}\text{F}$ compared to its surroundings. The temperature distributions in Figures 5.14 (c) and (d) are becoming more uniform compared to the previous analyses. The former possessed hot regions between 240 and $280\text{ }^{\circ}\text{F}$ in the majority of the sheet except the middle portion that contained cooler spots around $220\text{ }^{\circ}\text{F}$. The latter, however, exhibited hot temperatures close to $300\text{ }^{\circ}\text{F}$ distributed quite evenly from $x=3$ to $x=33$ inches.

The images in Figure 5.15 were qualitatively analogous. Figures 5.15 (a) and (b) displayed thermal maps with heated areas, around $250\text{ }^{\circ}\text{F}$, centered at $(6,12)$ and $(30,12)$. At $t=120$ seconds, these hot areas have reached temperatures close to $350\text{ }^{\circ}\text{F}$ and the distorted thermal signatures around $(6,12)$ and $(30,12)$ was contributed by excessive sag. The cooler middle portions of Figures 5.15 (c) and (d) have respective minimums around $220\text{ }^{\circ}\text{F}$ and $270\text{ }^{\circ}\text{F}$, exhibiting a $50\text{ }^{\circ}\text{F}$ difference between experimental and numerical results. This higher temperature prediction may come from the unity assumption of the view factor in the "TF505" software that simulated a higher heat transfer rate.



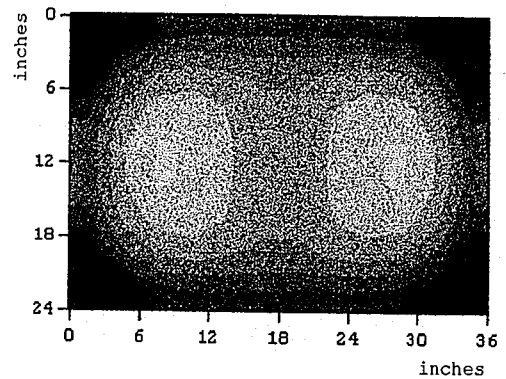
Pattern 6

Z = 12 inches

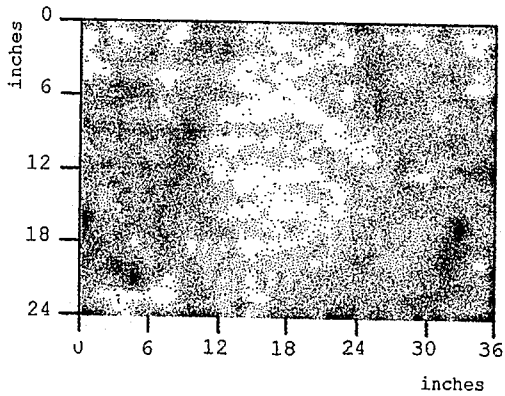


(a)

t = 60s

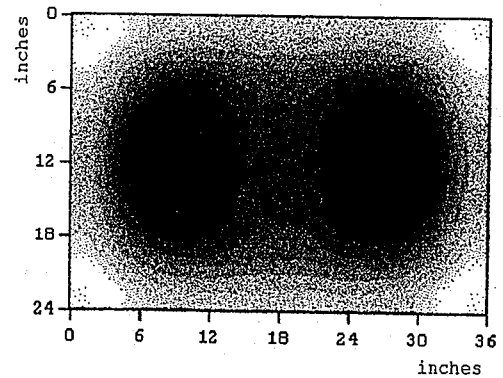


(b)



(c)

t = 120s



(d)

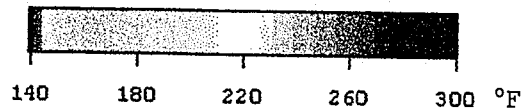
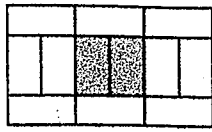
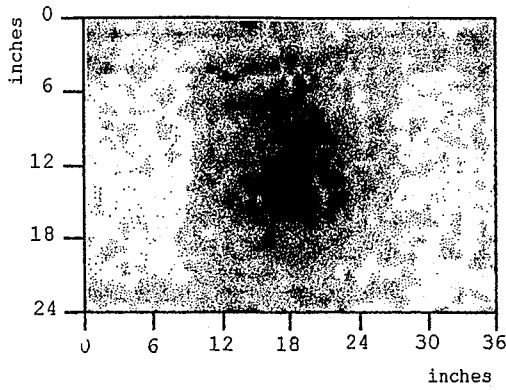


Figure 5. 14: Comparison of Theoretical and Experimental Temperature Distribution Corresponding to Heater Pattern 6 at Z = 12 inches: (a) Experimental IR Image at t=60s ; (b) Numerical Image at t=60s ; (c) Experimental IR Image at t=120s ; (d) Numerical Image at t=120s.

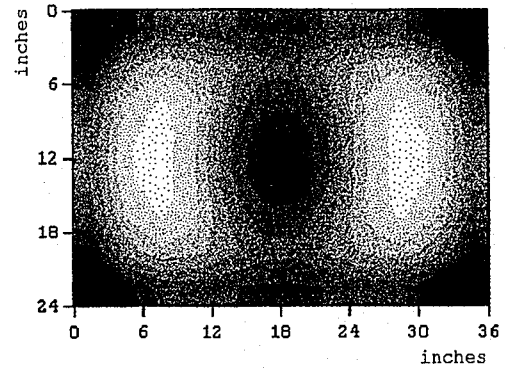


Pattern 6

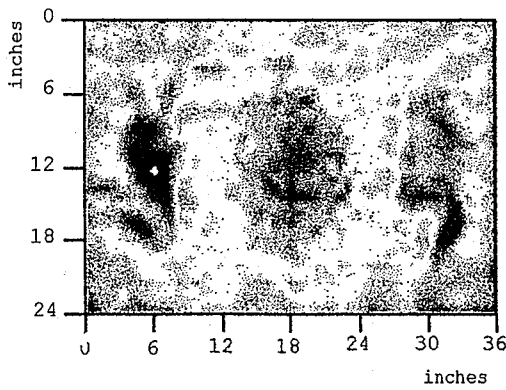
Z = 8 inches



(a)

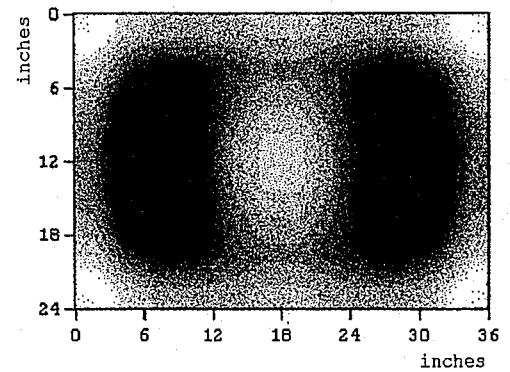


(b)



(c)

t = 120s



(d)

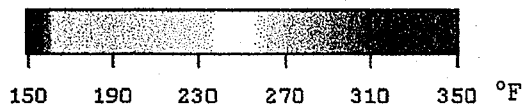
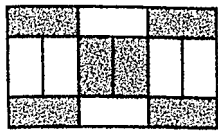


Figure 5. 15: Comparison of Theoretical and Experimental Temperature Distribution Corresponding to Heater Pattern 6 at Z = 8 inches: (a) Experimental IR Image at t=60s ; (b) Numerical Image at t=60s ; (c) Experimental IR Image at t=120s ; (d) Numerical Image at t=120s.

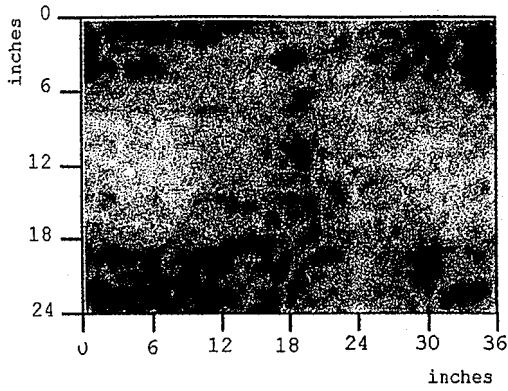
Pattern 7 was a slight deviation from Pattern 4 by the inclusion of two hot heaters on the left and right sides. After only $t=60$ seconds, not much could be concluded from the results, as shown in Figures 5.16 (a) and (b). However, within the next minute, two hot areas that centered at (5,12) and (31,12) ranging from 200 to 220 °F became apparent. Figure 5.16 (c) also suggested that the two hot heaters at $y=3$ and 21 inches have begun to influence the area of the sheet below them. In Figure 5.16 (d) the induced temperature pattern correlated well with Heat Pattern 7 except the hot middle portion. Perhaps the Z distance was large enough for the view factor of the hot heaters to influence a larger area below them.

The plots in Figure 5.17 presented good comparisons between experiment and simulation. At 60 seconds of heating time, the experimental image of Figure 5.17 (a) exhibited two hot spots that centered around (5,12) and (31,12) at temperatures between 210 and 220 °F. Moreover, the numerical result of Figure 5.17 (b) displayed similar if not cooler occurrences that centered around (7,12) and (29,12). The thermal map in Figure 5.17 (c) has a curious similarity to Heat Pattern 7. At $t=120$ seconds and a smaller separation of $Z=8$ inches, the experimental image has isolated hot regions around 270 °F almost directly underneath the hot heaters. A similar phenomenon was predicted by the numerical simulation as seen in Figure 5.17.



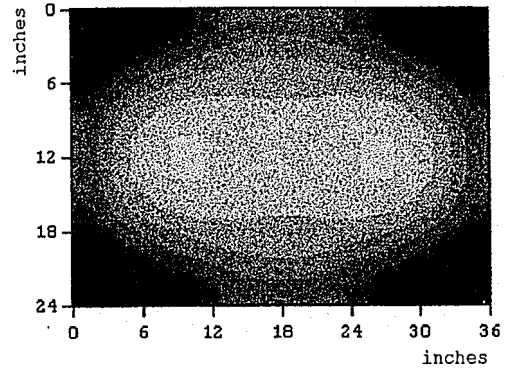
Pattern 7

Z = 12 inches

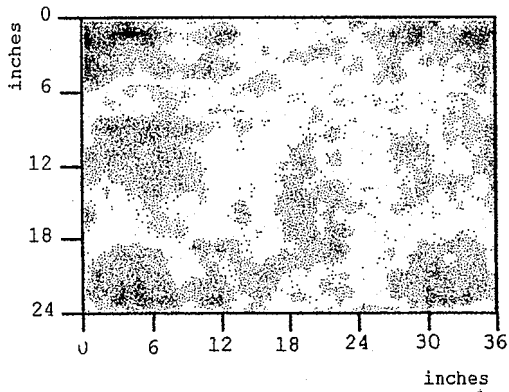


(a)

t = 60s

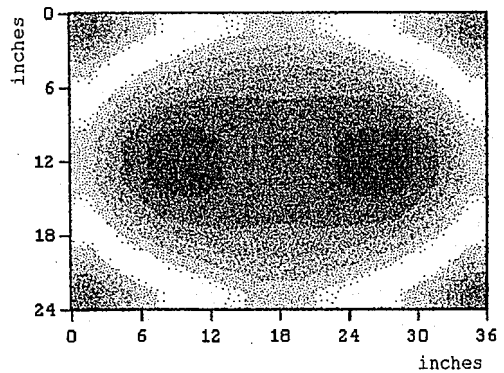


(b)



(c)

t = 120s



(d)

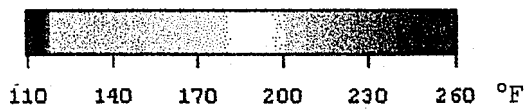
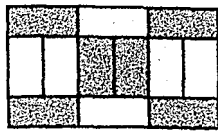
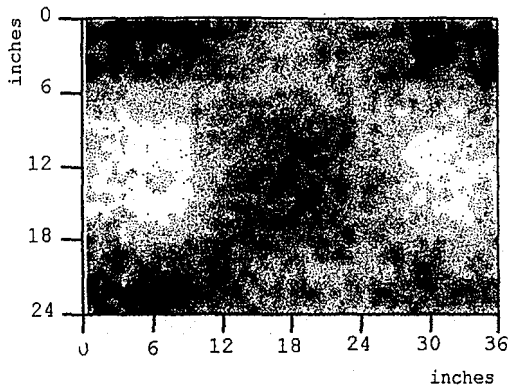


Figure 5. 16: Comparison of Theoretical and Experimental Temperature Distribution Corresponding to Heater Pattern 7 at Z = 12 inches: (a) Experimental IR Image at t=60s ; (b) Numerical Image at t=60s ; (c) Experimental IR Image at t=120s ; (d) Numerical Image at t=120s.



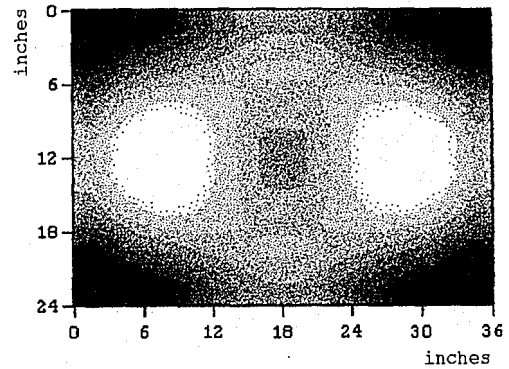
Pattern 7

Z = 8 inches

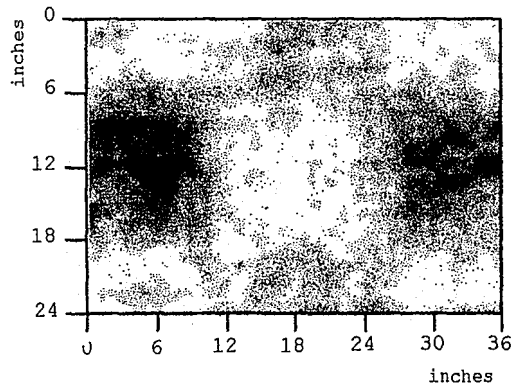


(a)

t = 60s

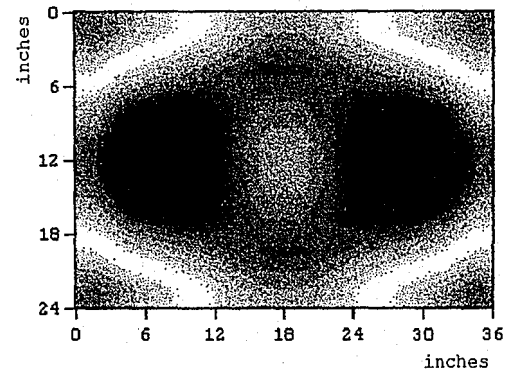


(b)



(c)

t = 120s



(d)

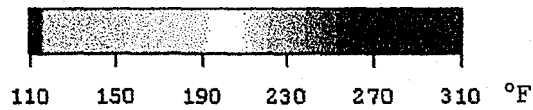
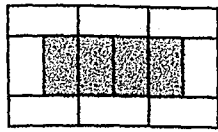


Figure 5. 17: Comparison of Theoretical and Experimental Temperature Distribution Corresponding to Heater Pattern 7 at Z = 8 inches: (a) Experimental IR Image at t=60s ; (b) Numerical Image at t=60s ; (c) Experimental IR Image at t=120s ; (d) Numerical Image at t=120s.

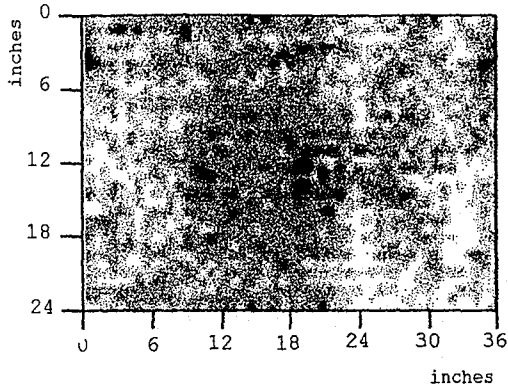
The heater arrangement of Pattern 8 with the hot heaters completely surrounding the cool elements was made to produce a more uniform sheet temperature distribution. At $t=60$ s, the experimental image, as illustrated in Figure 5.18 (a), appeared diffusive with temperatures ranging from 160 to 190 °F. The numerical result in Figure 5.18 (b) faintly exhibited a warm ring around a cool middle which may be otherwise interpreted as zero temperature gradient in this analysis. On the other hand, after $t=120$ s, the sheet temperature distribution became quite uniform as shown in Figures 5.18 (c) and (d). The former image contained tiny spots between $x=12$ and 24 inches at temperatures around 190 °F in a sheet dominated by temperatures between 210 and 230 °F. The latter plot displayed a mostly uniform temperature distribution between 220 to 240 °F with discernible edge losses near the four corners.

At a separation of $Z=8$ inches the induced temperature patterns, again, possessed well-defined patterns. Compared to Figure 5.18, the temperature uniformity was gone. The thermal maps in Figures 6.19 (c) and (d) appeared to be hotter versions of their (a) and (b) counterparts. The numerical and experimental results for both heating times exhibited good comparisons although the warmer ring in Figure 5.19 (b) is hardly apparent. The images of Figures 5.19 (c) and (d) qualitatively emulated Heat Pattern 8. The middle portion of the former plot is about 25 °F cooler compared to the latter.



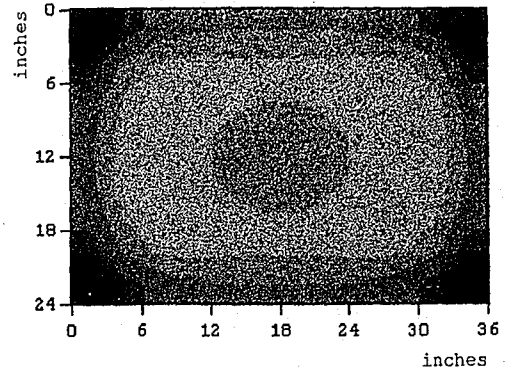
Pattern 8

Z = 12 inches

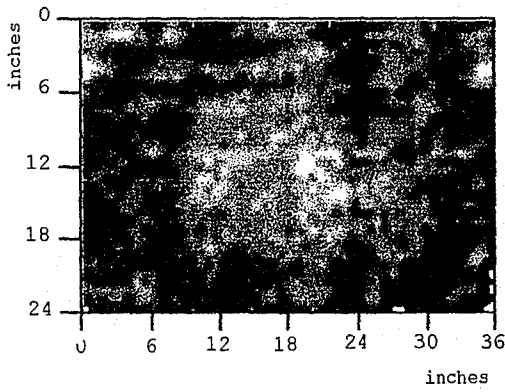


(a)

t = 60s

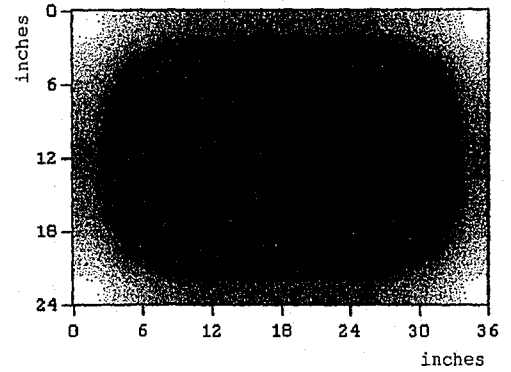


(b)



(c)

t = 120s



(d)

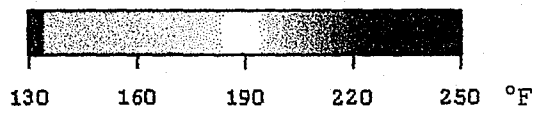
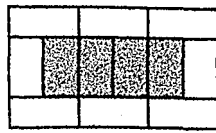
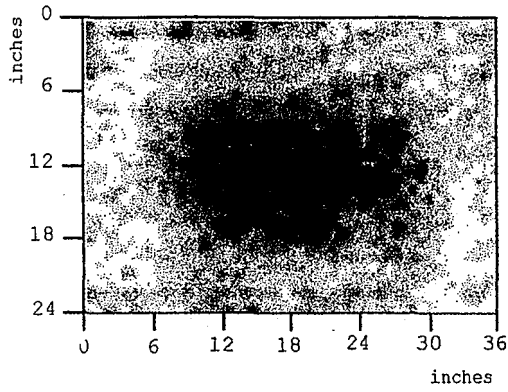


Figure 5. 18: Comparison of Theoretical and Experimental Temperature Distribution Corresponding to Heater Pattern 8 at Z = 12 inches: (a) Experimental IR Image at t=60s ; (b) Numerical Image at t=60s ; (c) Experimental IR Image at t=120s ; (d) Numerical Image at t=120s.



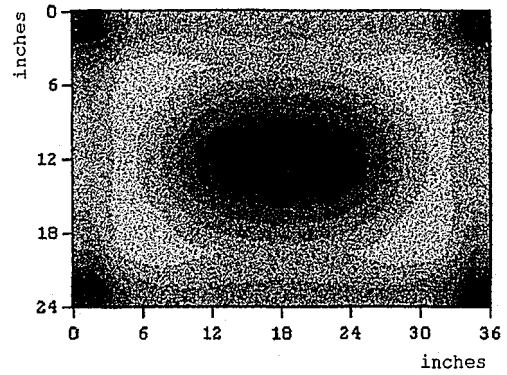
Pattern 8

Z = 8 inches

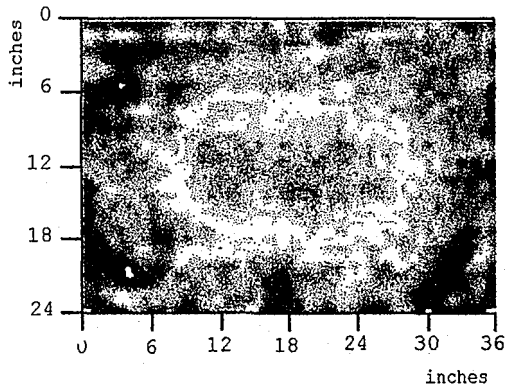


(a)

t = 60s

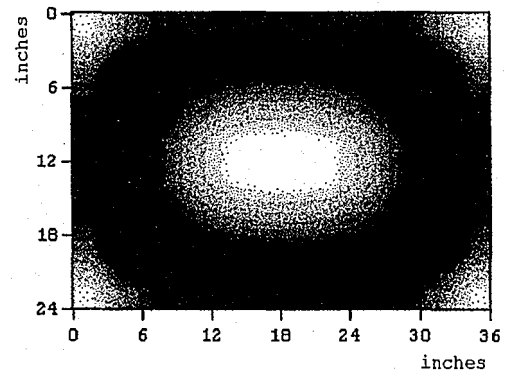


(b)



(c)

t = 120s



(d)

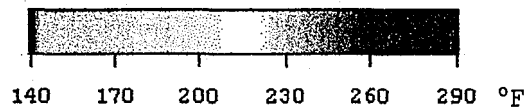


Figure 5. 19: Comparison of Theoretical and Experimental Temperature Distribution Corresponding to Heater Pattern 8 at Z = 8 inches: (a) Experimental IR Image at t=60s ; (b) Numerical Image at t=60s ; (c) Experimental IR Image at t=120s ; (d) Numerical Image at t=120s.

Upon completing these comparisons, conclusions could be drawn regarding the physical confines of zone-heating capability. Moreover, recommendations could be made for the ongoing task of refining the IR temperature sensing subsystem. These discussions, which represent a starting point towards intelligent thermoforming, can be found in the chapter that follows.

CHAPTER 6

DISCUSSION, CONCLUSIONS AND RECOMMENDATIONS

As a result of the combined thermoforming literature research, numerical calculations, and infrared imaging experiments performed during the present investigation, a number of observations and conclusions could be made. Overall, it was concluded that both the numerical modeling and experimental temperature sensing efforts were successful, and that a reasonable degree of correlation between theory and practice resulted. It was also concluded, however, that certain future improvements could lead to significant further related advancements. For example, it was found that the IR imaging comes with some shortcomings, such as a lack of polymer surface properties, which are crucial for accurate IR temperature measurement. Moreover, while the "TF505" zone-heating software package from Sherwood Technologies, Inc. was found to be quite useful for solving one-dimensional heat transfer problems with radiative and convective boundary conditions, a more comprehensive code would have been preferred. Furthermore, the utilization of radiant zone-heaters for eventual real-time control was concluded to require some additional developments. Such heaters continue to emit high levels of radiant heat minutes after being turned off and thus in an un-shielded fashion could not be used for real-time control. These findings require proper

explanation and documentation as this first phase of a larger, multi-investigator interdisciplinary thermoforming research program comes to a close.

6.1 Feasibility of Sensor-Controller Scheme

The Palm IR 250 imaging system is a remarkable device for the display of high resolution, 320 X 240 pixel, qualitative thermal images. With the PCX framegrabber and a typical laboratory PC, video footage at 14 frames per second (maximum) was displayed on the computer monitor. However, the quantitative analysis through the packaged calibration software needed much refinement, especially for the viewing of target objects at an angle. Furthermore, the temperature-dependent optical properties of the polymer target surfaces, which are very significant variables for quantitative sheet temperature calibration remains somewhat unknown.

During the present study, the IR imaging sensor was positioned above the forming area which necessitated the removal of the sheet clamping frame prior to an image capture. The present version of the "Autocapture" software was written to digitize the thermal image obtained from a lens positioned with a view angle perpendicular to the target sheet. Initially, a proposal was made to position the IR camera at a different angle in order to view the sheet in the heating area, as illustrated in Figure 6.1. Due to the continual refining state of the IR

software, this angle compensation capability, accurate to no less than a 30° angle to the sheet, was left as a subject for future research. In the experiment the IR camera, with a 25mm lens pointing vertically downward, captured images of the heated polymer sheets after a 3 second delay time once the target object slid from the heating to the forming area. Therefore, the sensor-controller scheme would have to account for a 6 second free-convection cooling time during the image capture if the sheet needed any further heating. Nevertheless, the employed measurement scheme was free from any constraints to mechanical changes in the heating domain of the thermoformer.

On the other hand, the proposal for a real-time IR sensing system would require not only the repositioning of the IR camera, but impose constraints to the distance between heater and sheet (Z distance). If Z is too small, the IR camera cannot obtain a proper field-of-view (FOV) of the target sheet. Additionally, the occurrence of sag will further undermine the situation as some areas of the sheet may become hidden from the camera's FOV. When these hurdles are crossed, a more elegant temperature sensing system will be available for incorporation into a real-time heater control scheme. Alternatively, the IR imager could remain in the forming area and be utilized as part of a stepwise iterative heating process.

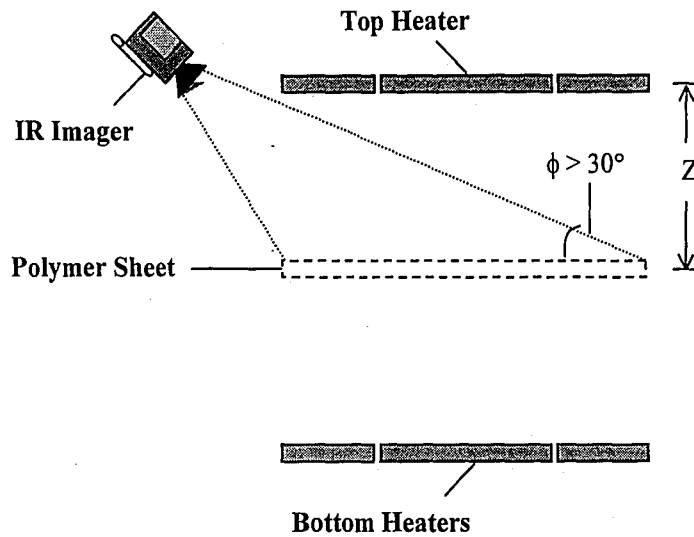


Figure 6. 1: A Proposed Thermal Imaging Procedure for Real-time IR Detection in the Heating Stage.

6.2 Numerical Program Usage

The transient heat transfer computer program from Sherwood Technologies, "TF505", was a worthwhile investment for an initial study of the thermoforming heating stage. However, for expediency in computation, simplifications were made to the view factor, F_{hs} , in "TF505" by assuming unity. In reality, the view factor is less than one ($F_{hs} < 1$) and becomes smaller as the Z distance increases. The view factor equation for two parallel rectangles, as shown in equation 6.1, yielded the following values of F_{hs} for $Z=12$ inches and $Z=8$ inches:

$F_{hs} = 0.528$ for a 12 inch heater-to-sheet distance, and

$F_{hs} = 0.621$ for an 8 inch heater-to-sheet distance.

The figures above were calculated using a 24 X 36 inch geometry.

$$F_{hs} = \frac{2}{\pi \cdot \bar{X} \cdot \bar{Y}} \left\{ \begin{aligned} & \ln \left[\frac{(1 + \bar{X}^2)(1 + \bar{Y}^2)}{1 + \bar{X}^2 + \bar{Y}^2} \right]^{1/2} + \bar{X} \cdot (1 + \bar{Y}^2)^{1/2} \cdot \tan^{-1} \frac{\bar{X}}{(1 + \bar{Y}^2)^{1/2}} \\ & + \bar{Y} \cdot (1 + \bar{X}^2)^{1/2} \cdot \tan^{-1} \frac{\bar{Y}}{(1 + \bar{X}^2)^{1/2}} - \bar{X} \cdot \tan^{-1} \bar{X} - \bar{Y} \cdot \tan^{-1} \bar{Y} \end{aligned} \right\} \quad (6.1)$$

$$\text{where } \bar{X} = \frac{\text{length}}{Z} = \frac{36}{Z} \quad \text{and} \quad \bar{Y} = \frac{\text{width}}{Z} = \frac{24}{Z}$$

Sheet sag also contributed to the change in view factor during heating. Therefore, a computational code would be even more useful if it included a capability to determine view factors for geometries other than two parallel flat plates. For example, an improved code would compute an array of F_{hs} values for every differential sheet element. When the view factor values are corrected, the radiant energy exchange calculations will increase in accuracy, instead of overestimating.

Another minor modification to the program could be made to expand the numerical analysis over the entire area of the sheet by autonomously setting the temperatures of the 24 heaters. "TF505" only allowed the analysis of a sheet quadrant by permitting the input of the heater temperatures in that particular quadrant. Therefore, the numerical results displayed in Chapter 5 were in all cases vertically and horizontally symmetrical. Obviously, this limitation could be altered by expanding the program to provide a complete heat transfer analysis from heater to sheet.

As a final note in this section, the sheet emissivity setting in "TF505" may require some future adjustment. The software's emissivity setting, which only recognized constants (with a 0.9 default value), could perhaps be substituted with an equation once the temperature-dependent data for the optical properties of polymers were obtained.

6.3 Possibilities for Temperature Patterns

In this study, the temperature patterns produced in the sheet were consistent with the individual zone-heater patterns. The comparisons in Chapter 5 demonstrated a change from more diffusive to well-defined temperature patterns as the Z distance decreased from 12 to 8 inches. At the edges of the sheet, the induced temperature appeared more diffused due to edge losses. Still, for the case of 2 minute heating time at Z=12 inches the numerical and experimental results, particularly the latter, closely matched their corresponding Heat Patterns. For the case where the hot heaters surrounded two cool heaters, as seen in Heat Patterns 6 and 7, the sheet temperature below the cool heaters was generally higher, around 190 °F, due to overlapping radiant exchange from the neighboring hot elements.

In the endeavor towards a future coupled sensing and control scheme, the zone-heaters will be individually computer-controlled in order to create the desired sheet temperature distribution. This would require fast control over each heater setting, be it a

considerable increment in power or total shut off. As radiant heaters continue to emit energy after shut down, due to the exponential decay of temperature, zone-heating alone could not induce distinctive temperature patterns for more complex, asymmetrical geometries. A credible solution to this predicament would be the use of mechanically adjustable screening shields that could either "shadow" or "burn" the polymer sheet. Not unlike the technique employed in darkrooms for the enlargement and development of photo prints, the radiant energy would be prevented from reaching the sheet and vice versa. This new method, modeled in Figure 6.2, of insulating shields used jointly with zone-heating would produce a more effective heating controls system.

6.4 Recommendations for Future Investigations

While the present study was somewhat successful, much room remains for the continued expansion of the subject matter. As a first investigative effort into an intended multi-year thermoforming program, this research study involved a significant amount of preliminary background investigation as well as the undertaking of unprecedented experimentation. This thesis focused on selecting the most relevant research direction with respect to the current manufacturing industry, and the procurement of new equipment with consideration given to the larger project theme of developing intelligent thermoforming in the future.

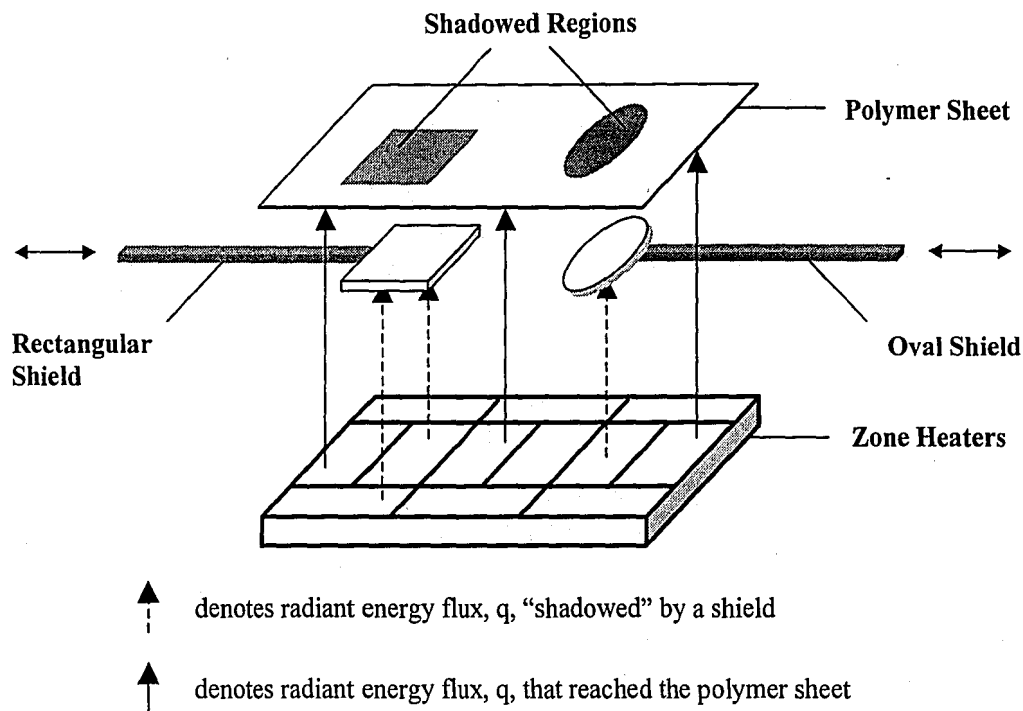


Figure 6. 2: A Model System for Improved Sheet Temperature Control by Combining Zone-heating with Moveable Heat Shields.

As a result of what was learned, a number of improvements for prospective future studies into this engineering topic can be suggested.

6.4.1 Further Improvements in IR Thermal Imaging System

First, the IR imaging system can be greatly enhanced by obtaining the optical properties of the target polymers of interest. It was found, late in the thesis work, that due to the semi-transparent nature of most polymer sheets, the values of their emissivity, transmissivity, and reflectivity were critical for accurate quantitative temperature measurements with the IR

imaging system. Moreover, there is evidence from a handful of journal papers that these optical properties of polymers vary with temperature. As was said before, polypropylene is semi-crystalline and turns transparent around its softening temperature. A common type of emissiometer or a spectrophotometer of the appropriate spectral intensity range, found in optics laboratories, could be used to characterize these material properties[40]. Furthermore, a comprehensive search should be conducted in the future to uncover whether or not such optical information, for the polymer thickness of interest, exists in the form of a database perhaps developed for the nuclear medicine and energy measurement industry.

The "Autocapture" software needs further tinkering as well. In its current state, this temperature calibration program will run for the purpose of capturing single or consecutive IR images. The calibration worksheet is a separate function found within the program window. For the purpose of real-time temperature sensing, the following capabilities would be required of the software:

1. Capturing and displaying a real-time temperature map that includes a color bar.
2. An incorporated calibration worksheet that needs only a single target data entry prior to the IR image display.

These seemingly straight forward revisions would have to be progressively communicated to the IR software vendor as they have

expressed their inexperience with such requests, especially in detecting semi-transparent material.

6.4.2 Revision of Radiant Heat Transfer Exchange Simulation

When the IR imaging system succeeds in accurate sheet temperature measurements, with respect to thermocouple readings, the thermoforming software will be provided with improved experimental comparisons. However, the finite difference sheet heating program requires improvements as well. A robust computer program would include a view factor calculation subroutine. Eventually, this computational software package would account for changes in the Z distances as the sheet sags towards the bottom heater. In addition, the sheet and heater could be divided into a number of differential elements for the individual view factor calculations prior to computing the radiant energy exchange.

6.4.3 Proposals for More Effective Zone-heating Thermoforming

The usage of other polymers that do not exhibit excessive sagging at softening temperatures would improve the heating and IR imaging aspects of this project. Polypropylene Homopolymer, though imbued with high melt strength, sags and wrinkles considerably at temperature above 250 °F. At its softening temperature of 300 °F, which is also the normal forming

temperature of PP Homopolymer, the sheet sag prevents a Z distance below 8 inches at the risk of burning the plastic at close proximity to or by contact with the bottom heaters. Moreover, excessive wrinkling at such temperatures in the sheet region around the clamp creates an uneven surface that distorts the emitted energy detection. PP and other thermoformable polymer sheets come in different grades and blends that are extruded for the purpose of vacuum-forming. The use of these alternatives is suggested. Finally, the development of controllable reflective shields combined with the zone-heating capability should be pursued as a subsequent phase of the overall research program.

In conclusion, the present research effort served as an initial endeavor into the area of intelligent thermoforming incorporating product quality monitoring and real-time process control. Developments were realized which significantly contributed to both the prediction of realizable polymer sheet temperature patterns, and the establishment of such patterns using IR thermal imaging and zone-heating control. The continued advancement of the research area, such as was suggested through the final chapter would lead to the eventual development of a fully intelligent thermoforming capability. This in turn would enable the utilization of cost-effective thermoforming processes for the manufacture of an expanded range of products, and thus benefit society as a whole.

REFERENCES

1. Blanco, A., *29th Annual SPE Automotive Awards*, in *Plastics Engineering*. 1999. p. 26-28.
2. Brophy, R., *Plastics will do nicely*, in *Automotive Engineer (London)*. 1999. p. 90-92.
3. Gabriele, M.C., *Large part thermoforming fills expanded application roles*, in *Modern Plastics*. 1999 JUN. p. 52-55.
4. Song, Y.H., Zhang, K F , et. al., *Study on the Warpage of Plastics Vacuum-Forming Process*. *Journal of Reinforced Plastics & Composites*, 1999. **18**(10): p. 931-941.
5. Leaversuch, R.D., *Solid PS enjoys resurgence in thermoformed food packaging*, in *Modern Plastics*. 1999. p. 64-67.
6. Wigotsky, V., *Thermoforming*, in *Plastics Engineering*. 1999. p. 24-29.
7. Bordonaro, C.M.V., T L. Galante, P A. Pineo, B. Scott, C E. *Optimization of processing conditions in thermoforming*. in *ANTEC*. 1998. Soc Plast Eng, Brookfield, CT, USA. p. 696-700.
8. Taylor, C.A.D., H G. Kazmer, D O., *Experimental and numerical investigations of the vacuum-forming process*. *Polymer Engineering & Science*, 1992. **32**(16): p. 1163-1173.
9. Michaeli, W., et. al. *Automation of the thermoforming process by a wall thickness closed-loop control*. in *ANTEC '96*. 1996. Indianapolis, IN. p. 863-868.
10. Knights, M., *Virtual Thermoforming: Ready for prime time?*, in *Plastics Technology*. 1999. p. 44-49.
11. Stephenson, M.J., Ryan, M E. *A Study of the Sagging of Styrenic Sheets Associated with the Thermoforming Process*. in *ANTEC '95*. 1995. p. 794-799.
12. Myers, J., *Closed-loop temperature scanners increase quality*, in *Modern Plastics International*. 1993. p. 20-22.
13. deLorenzi, H.G., Nied, H F , Taylor, C A, A *Numerical/Experimental Approach to Software Development for Thermoforming SIMulations*. *Journal of Pressure Vessel*

- Technology -Transactions of the ASME, 1991. **113**(1): p. 102-114.
14. Novotny, P., et. al. *Optimization of thermoforming*. in ANTEC '99. 1999. NYC, NY.
 15. Lappin, J.F., et. al. *Finite Element Modeling of the plug-assisted thermofoming process*. in ANTEC '99. 1999. NYC, NY.
 16. Aroujalian, A.N., Michael O. Emond, Jean-Pierre., *Effect of processing parameters on compression resistance of a plug-assist vacuum thermoformed container*. Advances in Polymer Technology, 1997 Summer. **16**(2): p. 129-134.
 17. Hamada, H., et. al. *Optimum Analysis Method For Thermoforming Process by Numerical Approach*. in ANTEC '95. 1995: Kyoto Inst of Tech & Mie Univ. p. 800-804.
 18. Parisi, M.J.R., M E. Charrier, J-M., *Experimental study on the dynamics of thermoforming of polystyrene*. Polymer Engineering & Science, 1994 JAN. **34**(2): p. 102-108.
 19. Laroche, D., Erchiqui, F. *Experimental and Theoretical Study of the Thermoformability of Industrial Polymers*. in ANTEC '98. 1998.
 20. Nam, G.J.R., H W. Lee, J W. *Finite element analysis of the effect of processing conditions on thermoforming*. in ANTEC. 1998. Atlanta, GA, USA. p. 690-694.
 21. Taylor, C.A. *Finite Element Simulation of Thermoforming-Experiments and Analyses*. in ANTEC '89. 1989. New York, NY. p. 435-437.
 22. deLorenzi, H.G., Hied, H F, *Blow Molding and Thermoforming of Plastics: Finite Element Modeling*. Computers & Structures, 1987. **26**(1-2): p. 197-206.
 23. Kouba, K., et. al. *Some new results in modeling of thermoforming*. in ANTEC '94. 1994. San Francisco, California: Society of Plastic Engineers. p. 850-853.
 24. Marchal, T.M.C., Nicolas P. Agarwal, Amit K. *Optimization of the thermoforming process: A few industrial examples*. in ANTEC. 1998. Soc Plast Eng, Brookfield, CT, USA. p. 701-705.
 25. DiRaddo, R.e.a. *Optimization of thermoforming with process modeling*. in ANTEC '99. 1999. NYC, NY.

26. Duarte, F.M.C., J A., *Heating thermoplastic sheets for thermoforming solution to direct and inverse problems*. *Plastics Rubber & Composites Processing & Applications*, 1997. 26(5): p. 213-221.
27. Throne, J.L. *Radiant Heat Transfer in Thermoforming*. in *ANTEC '95*. 1995. p. 810-821.
28. Throne, J.L., *Pattern Heating Polymer Sheet For Thermoforming (TF 501 & TF 505)*, 1996, Sherwood Technologies, Inc.: Hinckley, OH.
29. Throne, J.L., *Technology of Thermoforming*. 1996.
30. Wilson, J. *Thermal analysis of the bottle forming process*. in *Thermosense XIII*. 1991. Orlando, FL: The International Society for Optical Engineering, Bellingham, WA. p. 219-228.
31. Welch, T., *Scanning IR Sensors In Plastics Thermoforming*, in *Sensors*. 1993. p. 28-31.
32. Rietveld, J.X. *Inverse Method For Obtaining the Temperature Profile within a Mold Cavity via IR Pyrometry*. in *ANTEC '94*. 1994. p. 836-839.
33. Lappin, J.F., Martin, P J. *Sheet Temperature Measurement in Thermoforming*. in *ANTEC '96*. 1996. p. 878-882.
34. Raytheon, *Raytheon Commercial Infrared Products, 2000*, Corporate Communications, Raytheon Company: webmaster@raytheon.com.
35. Incropera, F., DeWitt, David, *Fundamentals of Heat and Mass Transfer*. 1996, New York: John Wiley & Sons.
36. Welty, J.R., *Engineering Heat Transfer*. 1974, New York: John Wiley & Sons.
37. Hottel, H., Sarofim, Adel, *Radiative Transfer*. 1967, New York: McGraw-Hill Book Company.
38. Kreith, F., *Principles of Heat Transfer*. 3rd ed. The Intext Series in Mechanical Engineering. 1973, New York, NY: Dun-Donnelley Publisher.
39. Cao, B., Sweeney, P. , Campbell, G. A. *Infrared Characteristics of Thin Polymer Film : Temperature Measurement of Polyethylene*. in *ANTEC '89*. 1989. New York, NY: Society of Plastics Engineers. p. 172-174.

40. Zhang, Y.P., et. al., *Method for Measuring Thermal Radiation Properties of Semi-Transparent Materials*. *Measurement Science & Technology*, 1994. 5(9): p. 1061-1064.
41. Cohen, Y.P.O., *ZMD International V-200 Series Vacuum Forming Machine*, 1999, ZMD INC., 600 West 15th Street · Long Beach, CA 90813, USA.

VITA

Khoo Guan Soon was born on the dawn of December 8th, 1975 in Penang Island, Malaysia. He attended Francis Light Primary School and, later, Penang Free School during his formative years. He obtained his Bachelor of Science degree with university and departmental honors in Physics and Mathematics from Susquehanna University, Pennsylvania in May 1998. Furthermore, he graduated with a Film minor and as valedictorian of the Class of 1998. Then, a graduate assistantship brought him to Lehigh University, Pennsylvania to pursue a degree in Mechanical Engineering. His graduate research in intelligent thermoforming under the direction of Dr. John P. Coulter was completed in June 2000 when he received his Master of Science degree in Mechanical Engineering from Lehigh University.

**END OF
TITLE**